Title
Mach Probes, Plasma Flows, and Heavy Impurity Transport in CSDX

Author
Gosselin, Jordan James

Publication Date
2016

UNIVERSITY OF CALIFORNIA, SAN DIEGO

Mach Probes, Plasma Flows, and Impurity Transport in CSDX

A dissertation submitted in partial satisfaction of the requirements for the degree
Doctor of Philosophy

in

Physics

by

Jordan James Gosselin

Committee in charge:

Professor George R. Tynan, Chair
Professor Cliff M. Surko, Co-Chair
Professor Dan H.E. Dubin
Professor Sergei I. Krasheninnikov
Professor Tom W. Murphy

2016

The Dissertation of Jordan James Gosselin is approved, and it is acceptable in quality and form for publication on microfilm and electronically:

Co-Chair

Chair

University of California, San Diego

2016

DEDICATION

This dissertation is dedicated to my parents for raising me with a strong interest in the natural world and because, as we learned from Marty McFly, without them I would never have existed.

Also, it is dedicated in part to Doc Brown for inventing Mr. Fusion. Did you happen to leave the plans for that lying around, Doc?

EPIGRAPH

To explain all nature is too difficult a task for any one man or even for any one age. Tis much better to do a little with certainty & leave the rest for others that come after, than to explain all things by conjecture without making sure of any thing.

-Sir Isaac Newton

TABLE OF CONTENTS

SIGNATURE PAGE iii

DEDICATION iv

EPIGRAPH v

TABLE OF CONTENTS vi

LIST OF FIGURES viii

LIST OF TABLES xiii

ACKNOWLEDGEMENTS xiv

VITA xviii

ABSTRACT OF THE DISERTATION xx

Chapter 1: Fusion: Power source of the future 1

- 1.1 The Tokamak 2

Chapter 2: Previous Work 8

- 2.1 Material Erosion: 8
- 2.2 Plasma Transport of Impurities: 11

Chapter 3: Experimental Methods 36

- 3.1 CSDX 36
- 3.2 Mach probe, plasma velocity measurements, and impurity entrainment times 38
- 3.3 LBO and Impurity Injection 40

Chapter 4: Initial comparison between Mach probe and Laser-impurity blow-off results 50

- 4.1 Model and Apparatus: 50
- 4.2 Results and discussion: 54
- 4.3 Conclusions: 57

Chapter 5: Overestimation of Mach Number due to Probe Shadow 62

- 5.1 Experimental Apparatus: 62
- 5.2 Results: 69
- 5.3 Discussion: 69
  - 5.3.1 Presheath Edge Density Correction 71

5.4 Summary and Conclusions: 77
Chapter 6: Multi-Species Ambipolar Diffusion Along a Magnetic Field 94
6.1 Introduction:.. 94
6.2 Experimental Methods:... 95
6.3 Results:... 101
6.4 Discussion:.. 102
6.5 Conclusion: 105
Chapter 7: Future Work 113
Appendix: 121
References: 124

LIST OF FIGURES

Figure 1 Diagram of the plan for the ITER tokamak, which at the time of publication of this thesis, is anticipated to be built in France.. 5

Figure 2 Schematic showing basic toroidal geometry of a tokamak. The major radius is given by R; the minor radius is given as ρ. Poloidal magnetic field is represented by Bθ; toroidal magnetic field is represented by Bϕ.This image is sourced from Argomedo's 2013 paper. 6

Figure 3 Image sourced from Pitcher's 1999 paper. This is a typical cross section of a tokamak (ASDEX Upgrade in this case) showing both the chamber and field geometry. 7

Figure 4 Schematic showing breakdown of the basic processes affecting the lifetime of plasma facing components. Taken from Phillips' 2006 paper[4]. 25

Figure 5 Diagram showing sputtering of a wall atom (green) by a plasma ion (brown). The plasma ion enters with an energy E_0 exchanging a portion of its energy (γE) with each collision, which gives a maximum imparted energy of (1-γ) γE_0 to the surface atom. 26

Figure 6 Figure borrowed from Phillips' 2006 paper[4] showing simulation results of enhanced sputtering of tungsten due to a small amount of carbon impurity being introduced into a deuterium plasma. The open circles represent experimental data for sputtering of tungsten and graphite with a pure deuterium plasma for comparison. ... 27

Figure 7 Figure showing simulation of tungsten impurity density in the SOL near the separatrix, adapted from reference 14. 28

Figure 8 Since the ion-ion collision frequency is inversely proportional to the temperature the ions are gently pushed up along the temperature gradient as they experience more momentum exchange from the colder ions on the bottom, cool side, and less momentum exchange with the warm ions on the top.. 29

Figure 9 Results from TEXTOR methane injection showing the ratio of carbon-13 to carbon-12 in the deposited carbon layers.. 30

Figure 10 Figure showing net deposition of carbon in the inner divertor region of the MkII-GB divertor in JET, adapted from Matthews 2005 paper[11]. Grey bars indicate compression of the deposits after multiple measurements with calipers. The asymmetry in divertor deposition is assumed to be due to flows in the SOL. 31

Figure 11 Contours of the emission from C-II emission in Alcator C-MOD. Figure adapted from LaBombard's 2004 paper[29] 32

Figure 12 Raw data from filterscopes in blue, and fit from equation 8 in red. Figure taken from Hollmann's 2011 paper[30]. 33

Figure 13 Results from Hollmann's 2011 paper[30] showing the transport parameters determined from the fitted model. 34

Figure 14 Measurements of the Mach number adapted from from LaBombard's 2004 paper[29]. It can be seen from the plots that the flows in the inner SOL approach Mach 1 in both upper and lower null configurations regardless of the line averaged plasma density.. 35

Figure 15 Diagram of CSDX showing the vacuum chamber, surrounded by the 28 magnetic coils. 43

Figure 16 Figure adapted from Thakur's 2014 paper. As can be seen in (a) most of the plasma column is within a five centimeter radius (r = 5).. 44

Figure 17 Schematic showing side and end views of the Mach probe. The tungsten electrodes are shown in red 45

Figure 18 Plasma velocity as determined from Mach probe data interpreted using equation 10. Figure is adapted from reference. These results indicate a plasma velocity that is increasing about an order of magnitude on axis from a Mach number of 0.1 to 0.9. 46

Figure 19 Plot of ratio of ion saturation currents for tips separated 180 degrees (shown in black). Fit from equation 10 (shown in red) is determined by adjusting $M_{\parallel}$ and $M\perp$ until best fit is achieved. It can be seen that the fitting function fits well at both low and high fields even though the derived Mach number is incorrect. 47

Figure 20 Calculation of the momentum exchange time for different background plasma flow velocities[21]....................48

Figure 21 Diagram showing the cross section of the laser blow off apparatus. A coated microscope slide is placed on a linear positioner. The linear positioner can be fully retracted into an interlock portion of the vacuum chamber to enable a quick change of the slide....................49

Figure 22 Image taken with high speed camera showing cross section of plasma. Camera is focused at the axial position of the injection port with 520 nm bandpass filter in front of lens.. 59

Figure 23 Data from the LBO experiments collected from the PMTs. Data is an average of about 60 individual shots; all signals are renormalized to a max height 1. A 1-D advection diffusion model is used to fit to the light emission from the impurities, which is shown here as the dotted lines overlayed on the data. 60

Figure 24 Top plot is Mach probe data at r = 0. Showing monotonic increase in interpreted parallel velocity across range of magnetic fields from 400 to 1600 gauss. Primary uncertainty in interpreted velocity of background plasma comes from uncertainty in the acceptance area of the probe....................61

Figure 25 Diagram showing the three-level scheme for LIF. Red laser light excites the metastable transition at approximately 668.61 nm, and the ion re-emits at 442.72 nm. 83

Figure 26 Schematic of LIF setup. Shown in red is the laser beam path; The laser travels through a window at the end of the plasma device and along the axis of the machine. Shown in the dotted line is the iodine cell enclosure. 84

Figure 27 Diagram showing the emission spectrum used by the three level LIF scheme. Zeeman splitting is illustrated for the 1 kGauss case. Line widths are arbitrary. The sigma transition branch used for the LIF measurements is shown in blue....................85

Figure 28 Diagram of CSDX showing the LIF laser beam (red online) and the PMT viewing area (green online). The overlap of the beam and PMT view gives the effective collection volume, which determines the spatial resolution of the experiment. 86

Figure 29 Histogram of the signal to noise ratio for the LIF data shown in this paper. As can be seen, most of the data points have a signal to noise ratio between 3.5 and 25. 87

Figure 30 Plot showing the LIF raw data with the fit used to extract the velocity. Temperature is determined from the width, and the mean velocity is determined by the shift of the function relative to the expected Zeeman shift. 88

Figure 31 Plot showing the plasma ion velocity as determined by the Mach probe (top) on the plasma axis (r=0) for comparison with the velocity on axis determined by LIF (bottom) on the plasma axis. 89

Figure 32 Schematic of the probe shadow and the boundary conditions for the presheath model.. 90

Figure 33 Low density wake calculated from simplified model at 400 and 1600 gauss magnetic fields. Contours represent $ny, znup$. Wake elongation due to decreased perpendicular transport can be seen clearly by comparing the two plots. 91

Figure 34 Background plasma density due to the geometric shadowing with different magnetic fields. The edge of the plot (at 23 cm) represents the presheath edge. The density at distances less than 23 cm from the probe tip is determined by the presheath physics. 92

Figure 35 Plot showing the application of the collisional presheath correction for 0-D model. 93

Figure 36 Parallel velocity measured by a Mach probe for the 400 gauss magnetic field. For calculations of the effect of shear the velocity profile is approximated as a quadratic, $V = V_0 (1 - (r/a)^2)$, where $V_0 = 3.6x10^4$ cm/s and a = 7 cm. 108

Figure 37 Plot of the ion saturation current in arbitrary units with a Gaussian fit to the profile visible in red. The best fit gives σ = 3 cm. 109

Figure 38 Simulated PMT signal illustrating effect of shear. Diffusion is neglected in the simulation. 110

Figure 39 Plot of the LIF signals at 400 and 1000 gauss showing the increasing width of the ion IVDF with increasing temperature. 111

Figure 40 Plot showing the diffusion coefficient as determined by the 1-D advection diffusion modeling 112

Figure 41 A schematic of a conceptual Mach probe side and end view. The progressively smaller radii should allow for simultaneous measurements of the Mach number with different correction factors 118

Figure 42 Head on image of the Mach probe fully inserted into the plasma column. Downstream of the probe a region of low light intensity can be seen. This is presumably due to a low density wake from the probe blocking the flowing plasma. Brightness and contrast on the image have been adjusted to emphasize the wake. 119

Figure 43 Velocity of the impurity cloud measured as a function of the RF power of the plasma source at 400 gauss. The impurity cloud velocity appears to be linearly proportional to the RF source power over the range of powers used. 120

Figure 44 Averaged iodine cell spectrum. Light intensity data is binned and averaged over ~350 individual LIF measurements.. 123

LIST OF TABLES

Table 1 In the left column are line shifts due to Zeeman splitting of the sigma, m = 1 transition from the central line location. Right column contains the relative amplitude of the line components. Total amplitude is normalized to 1. 80

Table 2 Values of the various collision frequencies used to calculate the perpendicular diffusion coefficient. 81

Table 3 Scaling parameters of the probe shadow. Parallel and perpendicular diffusion coefficients calculate from classical considerations as discussed in the text. 82

Table 4 Ion temperatures measured with laser induced fluorescence (LIF). Approximately a 50% increase in temperature is observed over the range of magnetic fields used in these measurements. 107

ACKNOWLEDGEMENTS

I would like to acknowledge the Department of Energy for funding both me and the science produced through the development of this dissertation. Without funding there is no scientist and without the scientist there is no science.

I would also like to acknowledge Professor George Tynan for acting as my advisor and the co-chair of my committee. His hand has been the one that has guided me through multiple projects and pushed me to produce the work contained in this dissertation. Through his support I will have either authored or co-authored a total of six articles pertaining to impurity transport and helicon produced plasmas, and I have been given great opportunities for exposure to the greater plasma physics community through a total of six conference presentations. I am undoubtedly a better and more productive scientist after having the opportunity to work in his group.

I would also like to acknowledge Professor Clifford Surko. In addition to being the co-chair of my committee, Cliff provided me with some very valuable laboratory experience for the first few years of my graduate school. Working in his group I co-authored three articles with Dr. James Danielson (who was also a valuable mentor) and learned invaluable laboratory and research skills.

Additionally, I would like to acknowledge the whole of the PISCES group, especially Dr. Russ Doerner, Dr. Saikat Chakraborty Thakur, Dr. Eric Hollmann, Dr. Daisuke Nishijima, Dr. Jonathan Yu, Ray Seraydarian, Leo Chousal, Rollie Hernandez, and Tyler Lynch. The advice and support of this excellent group of scientists and engineers has been immeasurably beneficial in the production of the work presented in

this dissertation and much of the scientific content is the result of long winded discussion and debate with Saikat.

There is a long list of people who have contributed to my interest in science and who have supported me in one way or another in the long journey to get this degree. I will do my best to thank them all, but I will undoubtedly have neglected to mention many.

First, I thank my mother, who taught me to read at a young age, which has given me an invaluable advantage that I have been able to leverage for a high level of success throughout my academic career. I also thank my father who has also cultivated my interest in the natural world through watching the birthing of fowls and dissecting rattlesnakes, among other things. Both of my parents labored to instill in me a strong work ethic, which has helped me push through many of the more difficult portions of my academic career.

My sister, Chenelle, has often provided me with her own point of view and advice on matters both personal and professional, and I will always appreciate her input and support. We don't always agree; when we don't agree it is invariably because she is wrong. She has taught me patience by continuously picking fights with me when we were children, and, for the record, she fights dirty; I have the scars to prove it.

My older brother and sister, Sean and Becca respectively, have always been people I look up to. Their unavoidable status of being nearly a decade older than me provides me with an intimate look into what the future could hold. Both are fantastic artists and have, by example, inspired me to continue to develop the creative side of myself.

My lifelong friend and doppelgänger, Paul McMillan, as well as his mother and father, Janet McMillan and Charles McMillan have also been instrumental in keeping me curious about the world. Paul and I dissected thousands of owl pellets as children, as well as household electronics and appliances (with or without permission). Our endless schemes of mischief and world domination helped me practice creative thinking and problem solving skills from a young age. Also, I have no doubt that Charles' career as a physicist influenced my decision to pursue a career in the same field.

My officemate and friend, Joseph Barton, has been a welcome distraction and valuable for both discussions of plasma physics and commiserating about the difficulties of research. He is a talented research who will do well wherever he decides to go. Also, he mentioned me in his acknowledgements and it would be quite rude of me to neglect to mention him.

I must thank my Norweigan grandmother Vergie Zuppan who has always been a supportive and stereotypical grandmother. Her strong Viking blood flows in my veins and provides me with determination. Also, her cookies are delicious. I must thank my gypsy grandfather Al Zuppan, who let me explore nature at his ranch and endowed me with a sense of humor that carries me through my day to day life. Also, I thank my proud Irish grandmother Lorre Rollins, who always has a story to tell and has always been supportive of my career as a physicist; although she has to be constantly reminded that I am not a nuclear physicist and I am not making atom bombs. Finally, I must thank my Grandfather Fred Rollins, who taught me how to cast a fishing rod and tie flies.

Finally, many of my friends have served as ample and welcome distractions from the continual academic grind. I treasure them all even if some of them have to be reminded that having a PhD does not make me that kind of doctor.

Portions of Chapter 5 have been submitted for publication of the material as it may appear in Physics of Plasmas, 2016, J. J. Gosselin, S. C. Thakur, S. H. Sears, J. S. McKee, E. E. Scime, and G. R. Tynan, American Institute of Physics, 2016. The dissertation author was the primary investigator and author of this paper.

Chapter 6, in full, is currently being prepared for submission for publication of the material. J. J. Gosselin, S. C. Thakur, and G. R. Tynan. The dissertation author was the primary investigator and author of this material.

Portions of the appendix have been submitted for publication of the material as it may appear in Physics of Plasmas, 2016, J. J. Gosselin, S. C. Thakur, S. H. Sears, J. S. McKee, E. E. Scime, and G. R. Tynan, American Institute of Physics, 2016. The dissertation author was the primary investigator and author of this paper.

VITA

2008	Bachelor of Science, University of California, San Diego
2010	Master of Science, University of California, San Diego
2016	Doctor of Philosophy, University of California, San Diego

PUBLICATIONS

“Heavy Impurity Transport Studies in a Weakly Collisional Plasma” J. J. Gosselin, S. C. Thakur, and G. R. Tynan. Manuscript in preparation

“Overestimation of Mach Number due to Probe Shadow” J. J. Gosselin, S. C. Thakur, S. H. Sears, J. S. McKee, E. E. Scime, and G. R. Tynan. Submitted to Physics of Plasmas, February 2016

“Formation of the ‘Blue Core’ in Argon Helicon Plasma” S. C. Thakur, C. Brandt, L. Cui, J. J. Gosselin, and G. R. Tynan. IEEE Trans. Plasma Sci 43, 2754—2759 (2015)

“Multi-Instability Plasma Dynamics During the Route to Fully Developed Turbulence in a Helicon Plasma” S. C. Thakur, C. Brandt, L. Cui, J. J. Gosselin, A. D. Light, and G. R. Tynan. Plasma Sources Sci. Technol. 23 044006 (2014)

“Simultaneous use of camera and probe diagnostics to unambiguously identify and study the dynamics of multiple underlying instabilities during the route to plasma turbulence” S. C. Thakur, C. Brandt, A. Light, L. Cui, J. J. Gosselin, and G. R. Tynan. Rev. Sci. Instrum. 85, 11E813 (2014)

“Positron Binding to Alcohol Molecules” A. C. L. Jones, J. R. Danielson, J. J. Gosselin, M. R. Natisin, and C. M. Surko. New J. Phys. 14 015006 (2012)

“Interplay Between Permanent Dipole Moments and Polarizability in Positron-Molecule Binding” J. R. Danielson, C. L. Jones, J. J. Gosselin, M. R. Natisin, and C. M. Surko. Phys. Rev. A 85, 022709 (2012)

“Dipole Enhancement of Positron Binding to Molecules” J. R. Danielson, J. J. Gosselin, and C. M. Surko. Phys. Rev. Lett., 104, 233201 (2010)

FIELDS OF STUDY

Major Field: Physics (Plasma Physics)

Studies in Matter-Antimatter Interaction
Professor Cliff M. Surko

Studies in Impurity Transport and Plasma Physics
Professor George R. Tynan

ABSTRACT OF THE DISERTATION

Mach Probes, Plasma Flows, and Impurity Transport in CSDX

by

Jordan James Gosselin

Doctor of Philosophy in Physics

University of California, San Diego, 2016

Professor George R. Tynan, Chair
Professor Cliff M. Surko, Co-Chair

Understanding wall material migration in tokamaks is fundamental to understanding the problem of the lifetime of the plasma-facing components in the tokamak. However, diagnostic access and plasma parameter control in tokamaks is difficult. In order to address the migration of wall material in the scrape-off layer of tokamaks, parallel transport of heavy impurities in a lighter flowing plasma is studied in an Argon plasma. The device used is CSDX, a 3m long, 20 cm diameter helicon plasma device at UC San Diego. Bismuth is injected using a technique called laser blow off (LBO). The resulting impurity transport is found to follow the expectations of classical collisional theory. A careful study of the plasma flows with multiple diagnostics, Laser Induced Fluorescence (LIF) and Mach probes, reveals a systematic error in the interpretation of Mach probe data. It is shown that the probe creates a low density wake on the downstream side. When the ion-neutral mean free path is comparable to the length of the shadow downstream of the probe, the Mach probe reports an artificially high Mach number when the shadow is not taken into account. A theory describing the low density wake is presented, which results in successful correction of the Mach probe results. It is demonstrated that ion-neutral collision effects can be important and should be taken into account when constructing Mach probes for velocity measurement in plasma devices.

Chapter 1: Fusion: Power source of the future

Fusion is the process of combining lighter elements into heavier elements. It is what powers the starts in the sky, including our sun, and fusion power is what provides the light and energy that gives life to this dusty rock that we call home. The basic principle relies on Einstein's most famous relation for matter at rest, $E = mc^2$. When the nuclei of the constituent atoms fuse the resulting particles are lighter than their constituents alone. The difference in mass between the constituent nuclei and the resulting particles is released as free energy.

The idea behind a fusion reactor is to harness the free energy provided by the fusion reaction and use it to run a turbine and generate electricity. The benefits to a fusion energy plant would be vast; fusion has many advantages when compared to current methods of energy production. The fuel source is huge and available globally. No greenhouse gasses are produced by the process. Also, unlike its sister nuclear energy process, fission, the radioactive products have relatively short half-lives and there is no risk of meltdown.

The fuel source being considered for future reactors is a deuterium-tritium fusion scheme. Both deuterium and tritium are heavy isotopes of hydrogen; deuterium has two nucleons (one proton and one neutron) while tritium has three nucleons (one proton and two neutrons). The deuterium and tritium react to produce a ^{4}He nucleus and one neutron. This reaction produces about 17.6 MeV of energy with 14.1 MeV being transferred to the neutron and 3.5 MeV being transferred to the ^{4}He nucleus (also called an alpha particle). Again, the principle behind a fusion reactor would be to harness the 17 MeV of free energy produced by this reaction and use it to spin a turbine and produce electrical power.

Deuterium can be harvested from sea water and is naturally available at levels of 0.015% of Hydrogen atoms[1]. Even at this very low level the amount of free energy available in a bucket of sea water is about 300 times the amount of energy available in a bucket of gasoline. Since seventy percent of the earth's surface is covered in oceans, this represents a remarkably abundant fuel source for fusion reactors.

In order for the fusion reaction to begin, the plasmas inside the reactors have to be heated to around 100 million Kelvin. This is ten times hotter than the core of the sun. At these temperatures the electrons have long since left the nuclei and the deuterium-tritium mix exists in a state called plasma. Plasma is defined as a collection of charged particles that exhibits collective effects.

No materials on earth that can withstand temperatures of 100 million Kelvin, and, therefore, the plasma is contained in a magnetic bottle. There are a few different schemes for magnetic confinement. Currently the most popular scheme is the Tokamak.

1.1 The Tokamak

The Tokamak is the most developed reactor concept. It is essentially a stainless steel, donut-shaped vacuum vessel with magnetic field coils that generate a toroidal field. A diagram of the vacuum chamber and the surrounding components is given in Figure 1.

There are a few important conventions in tokamaks that are important to understand for the sake of this thesis. First, we should address the basic coordinate system used to describe the Tokamak geometry, which is shown in Figure 2. As shown in the figure, if you were to stand inside the vacuum vessel and walk along the interior of the tokamak in the toroidal direction you would travel along the path S (in the direction ϕ) around the tokamak; this is the long circumference of the toroid. If you were to then traverse in the poloidal direction, θ, you would navigate around the smaller circumference. The major radius is defined as the radius of the toroid center as measured from the center of the toroid (the hole), given as R_0 in Figure 2. The minor radius, ρ, is defined as the radius from the center of the plasma to the last closed flux surface.

The vessel and magnetic geometry is shown in Figure 3. The combination of toroidal and poloidal fields gives flux surfaces that are shown as the dotted lines in the figure. A flux surface is defined as a region where the magnetic field lines never cross the surface. There are two distinct regions of flux surfaces. The first is the closed flux surface region; this region is also referred to as the core. This region is where the heat and particles are confined during an experimental run. Outside of the last closed flux surface (LCFS), also called the separatrix, is where the plasma is no longer contained; this region is called the scrape off layer (SOL). These flux surfaces are open and terminate in a region called the divertor. The separatrix has one special point, which is called the x-point or the null. This is where the magnetic field is zero and is located near the divertor.

Transport along the magnetic field lines is referred to as parallel transport, while transport across the magnetic field lines is referred to as perpendicular transport. Perpendicular transport is responsible for carrying particles across the separatrix into and out of the core.

As plasma is transported across the separatrix it escapes confinement and may encounter the walls of the device. The plasma will impact the plasma-facing components and cause erosion and degradation of the walls of the fusion device. This thesis work has been devoted to understanding some of the basic physics that governs wall erosion, specifically the transport of impurities in the plasma.

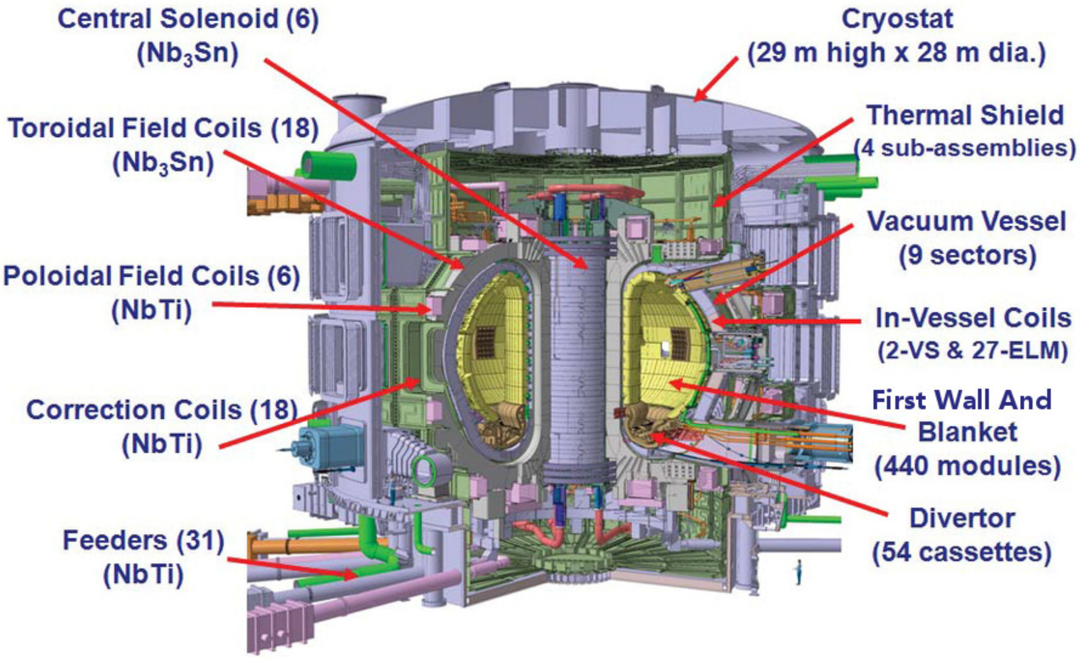

Figure 1 Diagram of the plan for the ITER tokamak, which at the time of publication of this thesis, is anticipated to be built in France. Shown in yellow is the blanket, which is referred to in the text as the "chamber wall". In brown is the divertor, and the diagram also shows the locations of the field coils that provide containment for the plasma. For scale, an averaged size human is shown in the bottom right of the figure. Image sourced from http://www.french-nuclear-safety.fr/ on 02/16/2016.

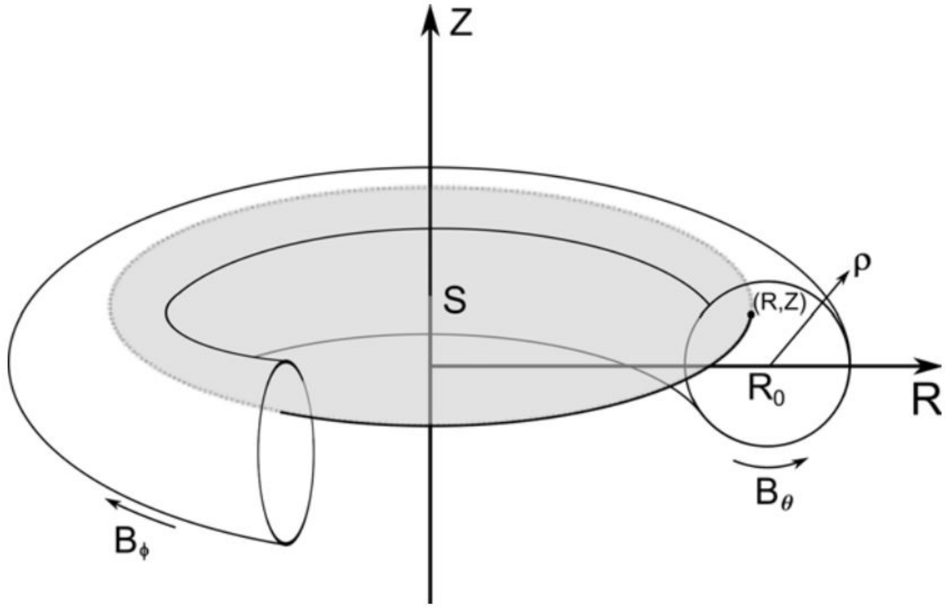

Figure 2 Schematic showing basic toroidal geometry of a tokamak. The major radius is given by R; the minor radius is given as ρ. Poloidal magnetic field is represented by B_θ; toroidal magnetic field is represented by B_ϕ.This image is sourced from Argomedo's 2013 paper[3].

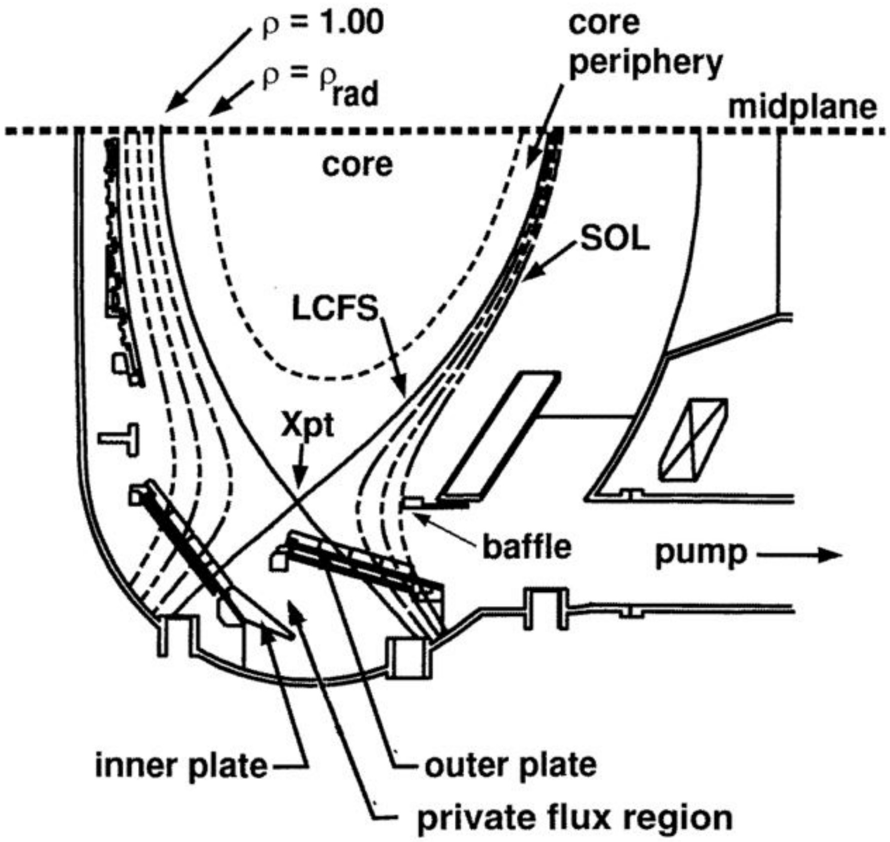

Figure 3 Image sourced from Pitcher's 1999 paper[2]. This is a typical cross section of a tokamak (ASDEX Upgrade in this case) showing both the chamber and field geometry. The dotted lines are flux surfaces. The solid line is the last closed flux surface (LCFS), which is also called the separatrix. Inside the separatrix is the core plasma, defined by its location in the closed flux surface region. Outside of the separatrix is the scrape off layer (SOL). In this region the plasma flows along the field lines to the divertor plates. The divertor plates are designed to take the large heat and particle flux from the plasma. The plasma recombines here and neutral gas can be pumped away through the baffle.

Chapter 2: Previous Work

The processes governing the erosion of plasma-facing components (PFCs) in ITER is still a major open topic of research within fusion science[4]. Before ITER, the erosion of the PFCs was not a major concern because the erosion processes were too slow to cause any practical damage. In a JET campaign from 1999-2001 the outer divertor plate was eroded by only tens of microns[5]. However, current tokamaks run on extraordinarily small duty cycles (10^{-2}) while ITER is planned to run with an order of magnitude higher duty cycle (0.1)[6], and future devices will run on even higher duty cycles eventually approaching steady state for an operational power plant. Longer net operating times will result in increased erosion of the components.

The processes governing the lifetime of the PFCs break down into (Figure 4): erosion from plasma impact, plasma transport of sputtered material, and impact of sputtered material into the surface[4]. The original intent of this thesis was to address the latter two processes listed above: plasma transport of sputtered material (referred to in this document as material migration) and the impact of the sputtered material back on the surface. To introduce the topic to the reader we will briefly address each of the components governing PFC erosion and lifetime.

2.1 Material Erosion:

The main sources of material erosion are physical and chemical sputtering. Physical sputtering involves the physical removal of a wall atom by exchange of energy with a plasma particle via a series of collisions in the surface region[4,6]. The momentum exchange is most simply modeled as a binary collision between the plasma particle and the wall particle. In this case the transfer of energy between an incoming particle with energy E_0, $M_1$and a wall particle with mass M_2 at rest is given as[4]:

$$T_m = 4\frac{M_1M_2}{(M_1+M_2)^2}E_0 = \gamma E_0 \qquad 1$$

If the trajectory of the incoming particle is assumed to be approximately normal to the wall, the incoming plasma particle must collide and ricochet off of at least one wall atom before transferring energy to a surface atom as illustrated in Figure 5. This results in a maximum energy of $E_{max} = \gamma(1- \gamma)E_0$ being transferred to the surface atom, and a threshold energy for physical sputtering of E_{th}[7]:

$$E_{th} = \frac{E_B}{\gamma(1-\gamma)} \qquad 2$$

Here E_B is the binding energy of the wall atom to the wall surface, γ is the fraction of energy carried over from the impacting particle after each collision as given by equation 1, and E_{th} is the minimum energy necessary for an incoming particle to eject a particle of wall material.

In addition to a threshold energy required for sputtering, the other notable result from equation 1 is that there is a peak in the energy transferred when $M_1 = M_2$. This means that sputtering by impurities from the plasma and self-sputtering from eroded wall material is going to be significantly more efficient at eroding the PFCs than sputtering by plasma ions. This effect can be seen clearly by the simulations shown in Figure 6, which has been borrowed from Phillips' 2006 paper[4].

Another pathway for removal of wall material is chemical sputtering, which is particularly effective for carbon materials especially at low plasma temperatures[8]. Chemical sputtering is essentially a process in which hydrogen from the plasma undergoes a chemical reaction with the wall material and removes carbon in volatile molecules[9].

In JET, emission from the C^{2+} impurities in the divertor and SOL was seen to drop when the device was run with a pure He plasma, which is consistent with a picture of chemical sputtering being responsible for a large portion of the carbon erosion[10]. Chemical sputtering is important for current devices; however, high neutron damage to carbon components is anticipated in a fully functioning fusion reactor, which rules out carbon components for power plants[11].

A detailed exposition on chemical sputtering is beyond the scope of this thesis. For our purposes, it can be viewed as the plasma-enhanced removal of weakly bound or volatile molecules found at the surface by chemical reactions between incoming plasma ions and atoms or compounds at the surface. The interested reader is encouraged to reference a survey of chemical erosion on carbon by Roth [12], the review of erosion by Federici[13], and the references therein.

Sputtering of material is a necessary but not sufficient condition for the erosion of PFCs. The erosion process also includes migration of the PFC materials. Once the material is sputtered from the wall it is transported through the plasma by friction and ion/electron temperature gradient forces. If the transport is short range, the net erosion is reduced because eroded material is replaced by incoming sputtered material from nearby. It is the long-range transport that is responsible for the net erosion of the PFCs[4,6].

2.2 Plasma Transport of Impurities:

In addition to affecting the rate of erosion of the plasma-facing components, the transport of impurities from the wall and target plates of the fusion device will affect the plasma performance[2]. The PFC erosion and material transport mechanisms are themselves linked to the plasma performance through plasma temperature, density, and flow velocity[14,15]. Thus, the plasma material interactions can be complicated and careful studies are important.

Impurity atoms that are sputtered from the surface can be transported perpendicularly into the core plasma. This is undesirable for two principle reasons. First, impurities dilute the fuel and reduce fusion power[16,17]. Second, the materials used for the wall and target plates (especially tungsten) may not be fully ionized in the core of the plasma and degrade the energy confinement time through enhanced bremsstrahlung radiation as well as line radiation from partially ionized impurities[16,17].

Parallel transport of the impurities along the field within the SOL is intricately related to both the lifetime of the PFCs and the perpendicular transport of impurities in the core. Simulations have shown that ion temperature gradient forces can pull sputtered impurities out of the divertor region where they travel to the top (crown) of the plasma device and are transported into the core of the plasma as shown in Figure 7[14]. This is important because impurities are not only sputtered off of the target plates but are also often injected in the divertor region in order to radiatively cool the plasma near the target[17].

In addition to moving impurities from the divertor region to areas where the impurities are more easily transported into the core, tritium inventory control will be an issue for future fusion-relevant devices such as ITER. Tritium can be co-deposited with eroded wall materials (especially with carbon) in regions shielded from the plasma where subsequent recovery of the tritium may be difficult. This inherently links the problems of parallel transport and tritium retention, and a better understanding of parallel transport can help elucidate the problem of tritium retention in ITER[18].

Parallel impurity transport in the SOL and divertor is inherently coupled to the lifetime of the PFCs, the long term migration of material, the tritium inventory in the device, and even the contamination of the core plasma. The parallel transport is determined by the friction force, electric fields, and ion/electron thermal gradients in the plasma[17,19]. Thermal gradient forces along the magnetic field lines are typically found near the divertor region of a tokamak because the plasma is recombining and cooling through both radiation and collisions with neutral particles[11,14,18].

The fundamental source of the thermal force is the inverse dependence of the collision frequency of ion-ion collisions on the temperature $\nu_{ii} = 4\pi e^4 \lambda_{ii} n_i m_i^{-\frac{1}{2}} T_i^{-\frac{3}{2}}$. Each collision imparts random momentum to the particle. The temperature dependence is inversely proportional to the temperature, $\nu_{ii} \propto T_i^{-\frac{3}{2}}$, and the momentum exchanged in each collision is on average proportional to the thermal velocity, $p_{ii} \propto T_i^{\frac{1}{2}}$. This means that on average the magnitude of the force exerted on a test particle in each collision is proportional to the inverse of the temperature[20], $F_{ii} \sim p_{ii} v_{ii} \propto T_i^{-1}$. Therefore, hotter background particles transfer less momentum to any given test particle, and that particle will move in the direction of the temperature gradient. This effect is starkly different from the thermal force in a neutral gas, which pushes particles preferentially against the gradient from the hot to cold regions.

The dependence of the thermal gradient force on the temperature gradient can be easily understood qualitatively as follows. Suppose a test particle in a system with a layer of hot plasma above a layer of cold plasma as shown in Figure 8. A test particle located between the two layers will experience an average force downwards from collisions with the hot particles inversely proportional to the temperature, $F_{hot} \propto \frac{1}{T_{hot}}(-\hat{z})$. Likewise, the test particle will experience an average upward force from the cold particles, $F_{cold} \propto \frac{1}{T_{cold}}\,\hat{z}$. The net force will be the sum of the two:

$$\begin{aligned}\boldsymbol{F_{net}} = \boldsymbol{F_{hot}} + \boldsymbol{F_{cold}} &\propto \frac{1}{T_{hot}}(-\hat{z}) + \frac{1}{T_{cold}}\,\hat{z} \\ &= \frac{(T_{hot} - T_{cold})\hat{z}}{(T_{hot}\,T_{cold})} = \frac{\Delta T\,\hat{z}}{T^2 - \left(\frac{\Delta T}{2}\right)^2} \approx \frac{\Delta T}{T^2}\,\hat{z}\end{aligned} \tag{3}$$

The gradient can be estimated as $\nabla T \approx \frac{\Delta T}{\Delta L}$, where $\Delta L \sim \lambda_{mfp} = \frac{v_{th}}{\nu_{ii}} \propto T^2$. Therefore, the thermal gradient force will be proportional to the temperature gradient.

$$\boldsymbol{F_{net}} = \boldsymbol{F_{hot}} + \boldsymbol{F_{cold}} \propto \frac{\Delta T}{T^2}\hat{z} \sim \nabla T \frac{\Delta L}{T^2}\hat{z} \propto \nabla T\,\hat{z} \qquad 4$$

The thermal gradient force can, of course, be calculated exactly assuming a Maxwellian distribution of the background ions, yielding[20]:

$$\boldsymbol{F_{\nabla T}} = \frac{15\sqrt{2}}{8}\left(1 + \frac{m_\beta}{m_\alpha}\right)\left(\frac{q_\alpha}{q_\beta}\right)^2 \exp\left(-\widetilde{v_\alpha^2}\right)\left[\boldsymbol{\nabla}T_\beta - 2(\boldsymbol{\nabla}T_\beta \cdot \widetilde{\boldsymbol{v_\alpha}})\,\widetilde{\boldsymbol{v_\alpha}}\right] \qquad 5$$

Here, the index β represents the background particles and the index α represents the test particle. The velocity, $\widetilde{v_\alpha}$ is normalized by the thermal velocity, $\widetilde{\boldsymbol{v_\alpha}} = \sqrt{\frac{m_\beta}{2T_\beta}}\left(\boldsymbol{v_\alpha} - \boldsymbol{v_\beta}\right)$. As mentioned above, the thermal force is especially important when considering transport of the impurities out of the divertor region of tokamaks[11,14,18].

Even more fundamental than the thermal gradient force is the friction force, which arises from Coulomb collisions transferring momentum to a test particle from the background plasma. This force can be calculated using [20,21]:

$$\boldsymbol{F_0} = -4\frac{\pi\lambda_{\alpha\beta}\left(q_\alpha q_\beta\right)^2\left(1 + \frac{m_\beta}{m_\alpha}\right)n_\beta}{2\,k\,T_b}\,\frac{\left(\Phi(\widetilde{v_\alpha}) - \widetilde{v_\alpha}\Phi'(\widetilde{v_\alpha})\right)}{\widetilde{v_\alpha}^3}\,\widetilde{\boldsymbol{v_\alpha}} \qquad 6$$

Here $\Phi(v) = \frac{2}{\sqrt{\pi}}\int_0^v \exp(-t^2)\,dt$ and $\Phi'(v) = \frac{d\Phi}{dv}$. This form assumes a Maxwellian distribution of the background particles, and the Φ and Φ' terms represent the integrated contribution of collisions with the background distribution. The friction force is important in all regions of the tokamak where the transport length scales involved are longer than the plasma-background ion mean free path.

A common technique for investigating the transport of impurities in the scrape off layer (SOL) of tokamaks is to inject hydrocarbons with heavy carbon, ^{13}C, which is found in natural abundances of only 1.1%[18]. This technique was originally pioneered at TEXTOR[22], where calibrated pulses of methane, $^{13}CH_4$, were injected through a hole in an aluminum target plate. The primary result from this study was that the carbon films in TEXTOR were rapidly eroded and redeposited in the machine. This was confirmed by the ratio of ^{13}C to ^{12}C on another aluminum target plate shadowed from the injected methane. The isotope ratio here was constant across the radius of the SOL as shown in Figure 9.

JET operated with the MkII-GB divertor for a period of three years from 1998-2001 in order to mimic the conditions in the ITER divertor. The pattern of deposition on the tiles in the divertor over these years was indicative of heavy net deposition on the divertor tiles in the inner divertor region and erosion of the tiles in the outer divertor region[23]. Results from these experiments are shown in Figure 10. These results are similar to results from ASDEX-U[24].

In addition to the net erosion measurements taken over years of operation, gas puffing experiments were performed with $^{13}CH_4$ puffed from the top of the vessel[23]. These results also showed a preferential deposition of ^{13}C in the inner divertor and no deposition outboard of the methane injection site. It has been hypothesized that the asymmetry in the divertor deposition is due to the entrainment of impurities in flows in the scrape off layer[11]. This hypothesis is consistent with measurements of the scrape off layer flow that have been measured in JET as well as other tokamaks[19].

A similar puffing experiment was performed in the ASDEX-U. In this experiment the methane plume was puffed in from the outer midplane, even further away from the inner divertor along the field lines. In this case, the deposition of ^{13}C was found to be very highly correlated with the long term deposition of carbon in the divertor[25]. This was surprising because the long term deposition profile had been assumed to be due to the distribution of strike points during the campaign. Since the two profiles were so similar, the conclusion was that short range erosion and redepostion is responsible for the profile of carbon deposition within each divertor leg. As with the JET studies, the ASDEX-U studies reported net deposition of ^{13}C in the inner divertor, consistent with impurities being entrained in the SOL flow.

Experiments with ^{13}C tagged methane were also carried out in DIII-D in both low density, L-mode plasmas and high density, H-mode plasmas[18]. These experiments were set apart from the above mentioned experiments in two ways. The first was that the injection of methane was done in a toroidally symmetric fashion. The second was that the CII and CIII light emission was monitored by cameras viewing the plasma. This allowed for an estimate of the velocity of the carbon ions based on the plume shape. These experiments also showed an accumulation of the carbon impurities on the inboard (high field side) divertor.

From the imaging diagnostic data, it seemed that the impurities were fully entrained in the SOL flow in the low density, L-mode case. The measurements in the high density H-mode plasma were inconclusive due to the rapid ionization to high ionization states in the denser H-mode plasma. However, later attempts to the experiment failed to simultaneously reproduce the carbon and the deuteron flows[26,27]. So, it was not possible to confirm what processes were controlling the impurity flows from the experimental data.

Deuterated ethylene gas was injected at different depths in the SOL of Alcator C-MOD[28] near the outer divertor with the goal of more carefully examining the structure of the plum entrained in the SOL flows. The C-II and C-III emission was imaged through a fiber bundle in order to examine the two dimensional structure of the plume. The plume structure was, of course, found to depend on the plasma parameters in the SOL. However, the plume structure was also found to depend on interactions between the reciprocating gas injecting probe and the background plasma, which made interpretation of the results complicated, and not necessarily indicative of the transport in an unperturbed plasma.

Additional plume injection experiments were carried out on the high field (inner) midplane of Alcator C-MOD[29]. In these experiments the plume was seen to be consistently elongated in the direction of the inner divertor as shown in Figure 11. Unfortunately, these plumes were perturbative to the plasma, but there was a clear trend of indicating impurity flow towards the inner divertor regardless of the position of the null point, which is consistent with all the other SOL impurity experiments.

This is a significant amount of evidence for the entrainment of the carbon impurities in the SOL flows [18,19,23,25]. However, the flows in the SOL are complicated[29], and diagnostic access in tokamaks is often limited. This in turn often makes understanding the complete physical picture of entrainment in the SOL difficult[26–28]. In order to better understand the basic mechanisms behind impurity transport in a flowing plasma experiments were performed in the linear divertor simulator, PISCES-A[30].

For these experiments, impurities were injected into PISCES-A using a technique called laser blow off (LBO). Laser blow off uses a laser pulse to ablate impurities from a thin film that has been deposited onto a glass slide. LBO has been used previously in tokamaks to study perpendicular transport of impurities[16,31–34]. To the authors knowledge LBO has only been used to study parallel transport in the experiments done in the TJ-II stellarator[34], the experiments in PISCES-A[30], and the experiments described in this thesis.

One great advantage of the LBO system over the gas puffing system is the well-defined nature of the source term. With the gas puffing technique the molecules of gas must become disassociated, and then the individual atoms become ionized leading to some uncertainty and spreading of the location of the source term[18]. Additionally, the gas puffing technique releases a plume of gas, which may have a duration on the order of milliseconds[35], whereas LBO can provide impurity deposition times on the order of tens of microseconds[30,34]. So, the modeling of the impurity transport is greatly simplified because the LBO source term is significantly shorter in injection duration and spatial extent compared to gas puffing.

The second advantage to LBO is that the choice of impurity is only limited by what can be coated onto a slide. Laser blow off experiments have been performed with lithium[36,37], carbon[34,36], nickel[16,36], silicon[36], calcium[31], boron[30,34], aluminum[30], iron[31], tungsten[31], and bismuth (work in this thesis). The LBO technique allows access to a wider variety of impurity to background ion mass ratios and a wider variety of charge states than are available from just gas puffing.

For the impurity entrainment experiments in PISCES-A[30] aluminum (27 amu) and boron (11 amu) were used as the injected impurities. The background was a helium plasma (4 amu) with a typical density of $5\text{x}10^{12}$ cm^{-3} and electron temperature, T_e, of 5 eV. The light emission from the impurities was monitored using a "filterscope" consisting of a photomultiplier tube (PMT) and optical bandpass filter located at a window at the injection site as well as windows 25 cm upstream and 22 cm downstream of the injection site.

Impurities were modeled using an advection-diffusion equation with source and sink terms. The perpendicular diffusion was modeled as a decay term.

$$\frac{\partial n_j}{\partial t} = D_{||,j}\frac{\partial^2 n_j}{\partial z^2} + V_{||,j}\frac{\partial n_j}{\partial z} + \left(\frac{\partial n_j}{\partial t}\right)_{source} - \left(\frac{\partial n_j}{\partial t}\right)_{sink} - \frac{n_j D_{\perp,j}}{\left(\frac{R_p}{j_{0,1}}\right)^2} \qquad 7$$

Here, R_p represents the radius of the plasma and $j_{0,1}$ is the first zero of the J_0 Bessel function. The impurity source comes from the injection, and the sink comes from losses to higher ionization states, which was estimated from the n_e and T_e profiles. The fit to the experimental data was determined by allowing $D_{||,j}, V_{||,j}$, and $D_{\perp,j}$ to vary as free parameters. Examples of the raw data and fits from the modeling are shown in Figure 12.

The results from the boron and aluminum experiments are shown in Figure 13. It can be seen that while the boron ions are fully entrained in the background helium plasma, the aluminum ions are only at about 50% of the velocity of the He^+ ions as measured by spectroscopy. This is a surprising result because the calculated ion-ion collision time is an order of magnitude shorter than the experimental time scale. It was speculated in the paper by Hollmann[30] that the low measured impurity velocity could be a result of the entrainment time being longer than time calculated by a classical binary collision model. If the momentum exchange time is long compared to the transit time between the injection site and the downstream port this would explain the discrepancy between the measured velocity of the impurities and the plasma velocity.

Understanding the entrainment of heavy impurities in a background flowing SOL plasma is important for the erosion of the PFCs. Heavy impurities traveling at the same speed as the background plasma will collide with the PFCs at a higher energy (due to their heavier mass). The increase in energy is due to the difference between the kinetic energy of the entrained particles (moving at the same velocity as the background plasma) and the energy due to the presheath drop (impurities have the same kinetic energy as the background plasma. This increase is given by $\Delta E = \left(\frac{M_{imp}}{M_D} - 1\right)\left(\frac{e(T_e+T_i)}{2}\right)$, and for SOL ion and electron temperatures of 20 and 10 eV[38] would give a significant energy increase of up to 1.4 keV for tungsten and 700 eV for molybdenum. Also, if the impurity is the same element as the wall material itself the energy transfer between the incoming impurity and the wall elements will be maximized. Both of these effects can lead to greatly enhanced sputtering and erosion of the PFCs.

Experiments have been done to measure the parallel flows in the SOL of plasmas with Mach probes, which consistently show flow speeds approaching the sound speed in the SOL[19]. A relatively thorough study was done in the SOL of Alcator C-MOD with Mach probe measurements at multiple locations around the SOL[29]. These measurements were carried out at different densities and under both upper and lower null geometries. The results from the Mach probe measurements are shown in Figure 14. It can be seen clearly in the figure that the parallel Mach number in the SOL approaches 1 at the inner SOL regardless of the null configuration or line averaged plasma density.

An impurity ion that is accelerated up to Mach 1 will definitely impact the PFCs with a higher energy than if it was just accelerated by the presheath potential as defined below. This clearly should be accounted for when estimating erosion rates of the inner wall of the tokamak based on the flow measurements in the SOL. However, even without these high flows it may be possible for the impurity ions to become frictionally coupled to the background plasma in the presheath, and the impurities will then impact the wall at the sound speed of the background ions.

The incoming energy of the plasma ion causing the sputtering is a result of the plasma parameters, specifically the ion temperature (T_i) and the electron temperature (T_e). Because of their smaller mass (and typically higher temperature), the electrons in the plasma are more mobile and reach the wall first. Since the bulk plasma remains quasineutral, this drops the potential of the wall relative to the plasma until the flux of electrons leaving the plasma is the same as the flux of ions leaving the plasma (no net current, j = 0). This low potential boundary results in a small scale, non-neutral, positive potential region near the boundary called the sheath. In order to break the quasineutral condition, the plasma ions must be accelerated up to the plasma sound speed, $c_s = \sqrt{\left(\frac{T_e + T_i}{M_i}\right)}$, at the sheath/plasma boundary[39]. This condition on the ion velocity is called the Bohm criterion. The Bohm criterion results in an electric field that extends into the plasma some length, L_{ps}, commonly referred to as the "presheath".

However, in the boundary of fusion devices the plasma contains both the fusion fuel (D^+ and T^+) and impurity ions. The main source of impurities is sputtering from the wall[40], but light impurities are sometimes injected into the divertor region of tokamaks in order to radiate away the thermal energy of the plasma before it strikes the divertor plates[17]. So, a typical fusion plasma will have multiple ion species.

In a multispecies plasma the Bohm criterion is no longer unique[41–43] and is given as:

$$\sum_j \frac{n_{j0}}{m_j V_{j0}^2} \leq \frac{n_{e0}}{Te} \qquad 8$$

Here, n_{j0}, m_{j0}, and V_{j0} represent the density, mass, and velocity of the jth ion species. If the concentration of the impurities is low equation 8 reduces to the single species Bohm criterion, $V_{i0} \geq c_s$, where V_{i0} represents the bulk velocity of the main plasma ions.

If the momentum exchange time between the impurity ions and the background plasma is shorter than the transit time of the impurities through the SOL plasma and presheath, then the impurities will impact the PFCs at the sound speed of the background plasma regardless of the plasma flow speed in the SOL. This will result in the impurities impacting the PFCs at a much higher energy than the background ions. As mentioned above, this increase could be up to 1.4 keV for ITER. However, if the momentum exchange time is significantly longer than the transit time of the impurities through the presheath, then the impurities will strike the wall at the same energy as the background plasma ions because their energy gain is due to the presheath potential drop only. So, the entrainment time is limited to the impact energy of impurities with the PFCs.

Clearly, understanding the basic physics of impurity entrainment is important for understanding and predicting the lifetime of the PFCs. Due to the complexity of the flows in the SOL it is difficult to do detailed studies in tokamaks. In linear devices, there is some evidence that heavy impurities may not be entrained in plasmas as quickly as predicted by the classical theories[30].

These considerations then motivated the original goal of this thesis project-to measure the entrainment time between heavy impurities and the lighter background ions in the CSDX plasma. A rigorous test of the basic binary frictional coupling theory in a laboratory plasma has not been performed. Initial results implied that the plasma velocity could be manipulated in CSDX, which would allow for a systematic adjustment of the entrainment time. However, this turned out to be a systematic error in the Mach probe interpretation. The discrepancy between the Mach probe and the actual velocity and a theory describing the source of the discrepancy is described in the next two chapters.

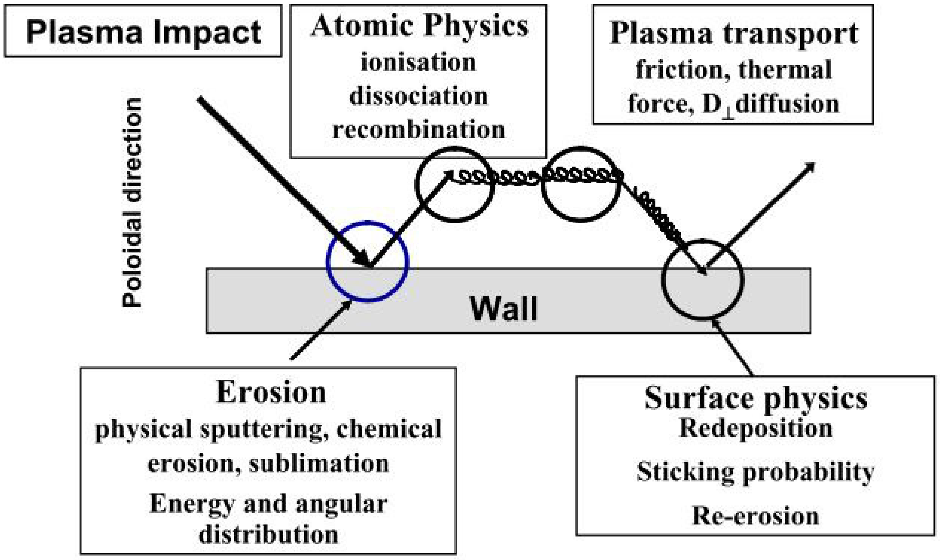

Figure 4 Schematic showing breakdown of the basic processes affecting the lifetime of plasma-facing components. Taken from Phillips' 2006 paper[4].

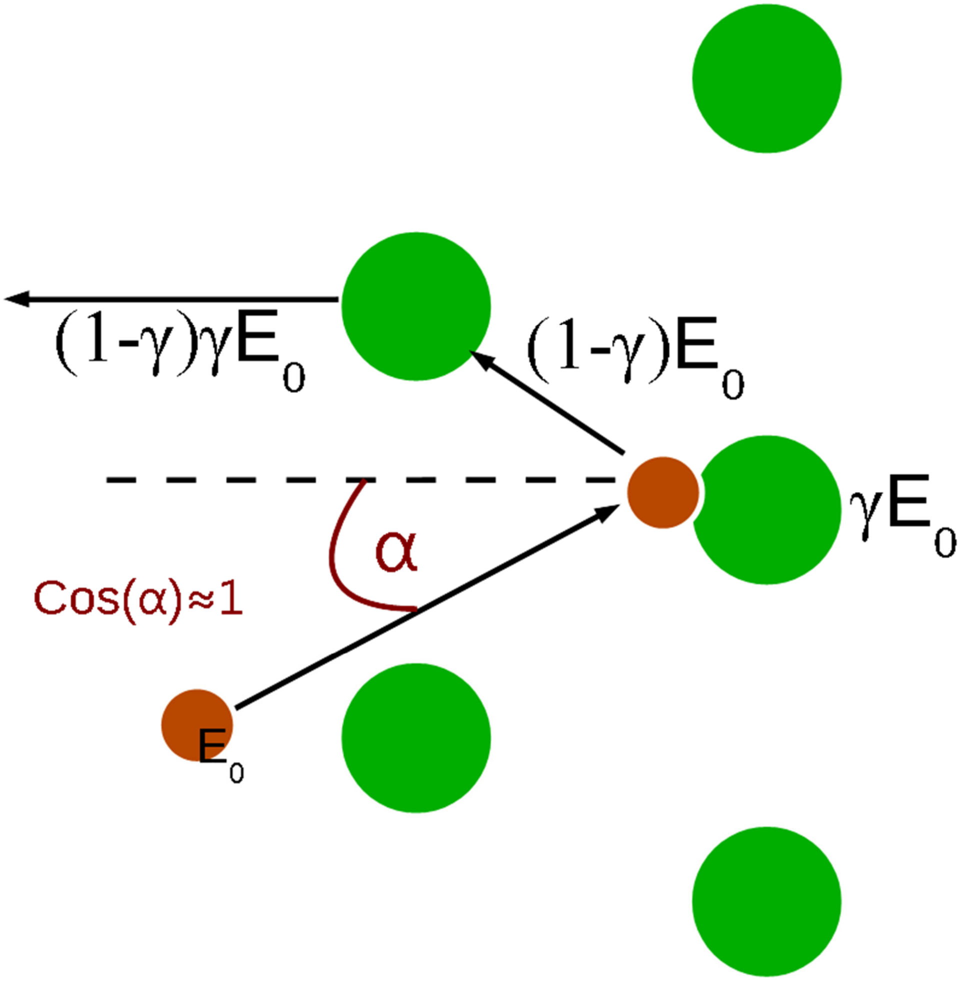

Figure 5 Diagram showing sputtering of a wall atom (green) by a plasma ion (brown). The plasma ion enters with an energy E_0 exchanging a portion of its energy (γE) with each collision, which gives a maximum imparted energy of (1-γ) γE_0 to the surface atom. The final energy, (1-γ) γE_0 must exceed the binding energy of the atom to the surface.

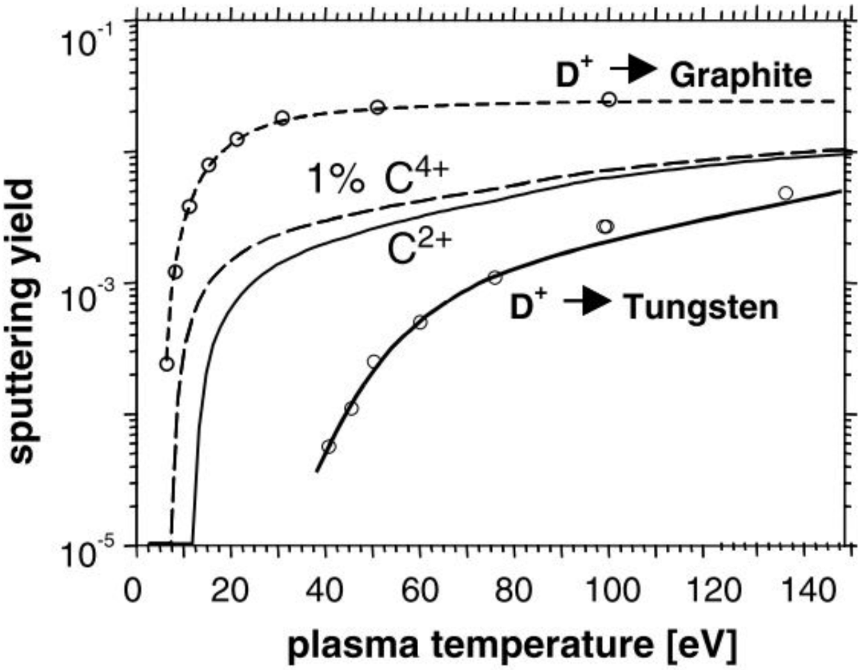

Figure 6 Figure borrowed from Phillips' 2006 paper[4] showing simulation results of enhanced sputtering of tungsten due to a small amount of carbon impurity being introduced into a deuterium plasma. The open circles represent experimental data for sputtering of tungsten and graphite with a pure deuterium plasma for comparison.

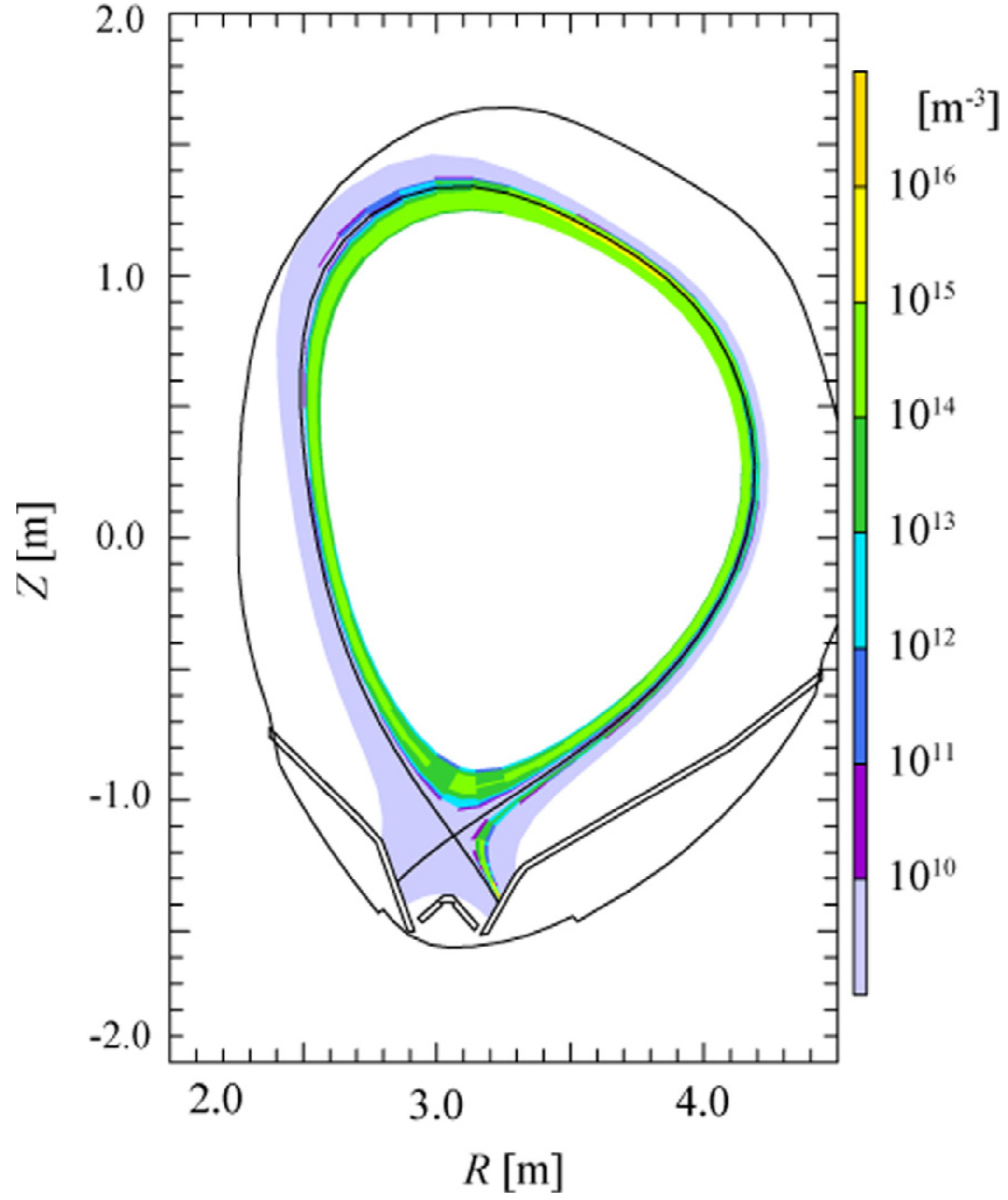

Figure 7 Figure showing simulation of tungsten impurity density in the SOL near the separatrix, adapted from reference 14.

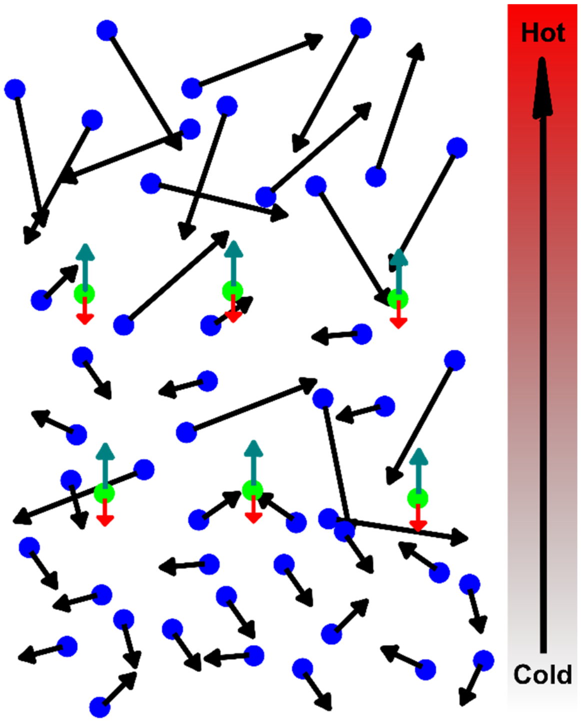

Figure 8 Since the ion-ion collision frequency is inversely proportional to the temperature the ions are gently pushed up along the temperature gradient as they experience more momentum exchange from the colder ions on the bottom, cool side, and less momentum exchange with the warm ions on the top. This is shown schematically with the green "test particles" in the figure. The red arrows represent the smaller force due to the hot ions, and the green arrows represent the larger force due to the cold ions. The result is a net force upwards towards the hotter plasma.

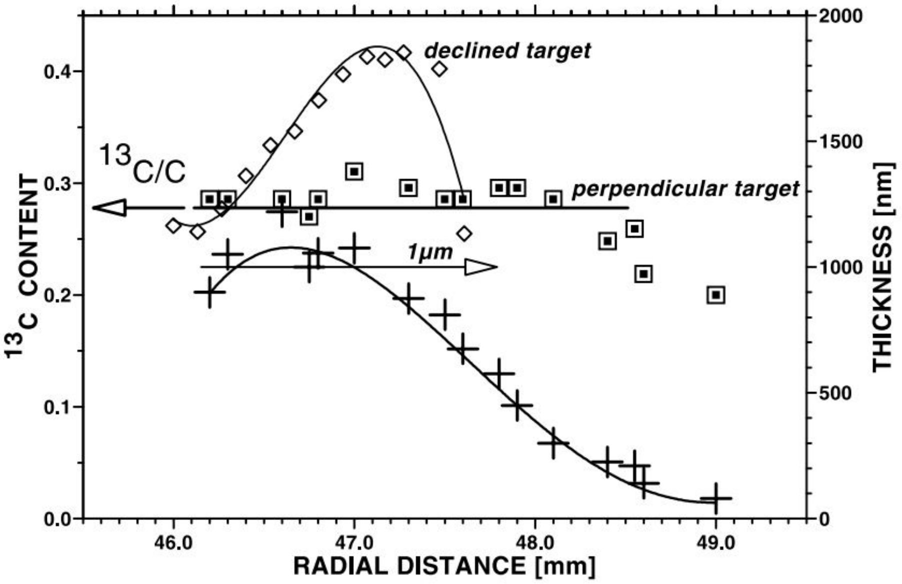

Figure 9 Results from TEXTOR methane injection showing the ratio of carbon-13 to carbon-12 in the deposited carbon layers. Square and diamond signals represent the carbon isotope ratio. The perpendicular target is shadowed from the methane injection by the declined target. The flat profile on the perpendicular target was taken to indicate that the carbon-13 is being deposited and reeroded from locations all over the interior of TEXTOR and redeposited onto the perpendicular target. The high carbon-13 ratio at 47.3 mm is due to the proximity to the methane injection hole. Figure originally appeared in Wienhold's 2001 paper[44].

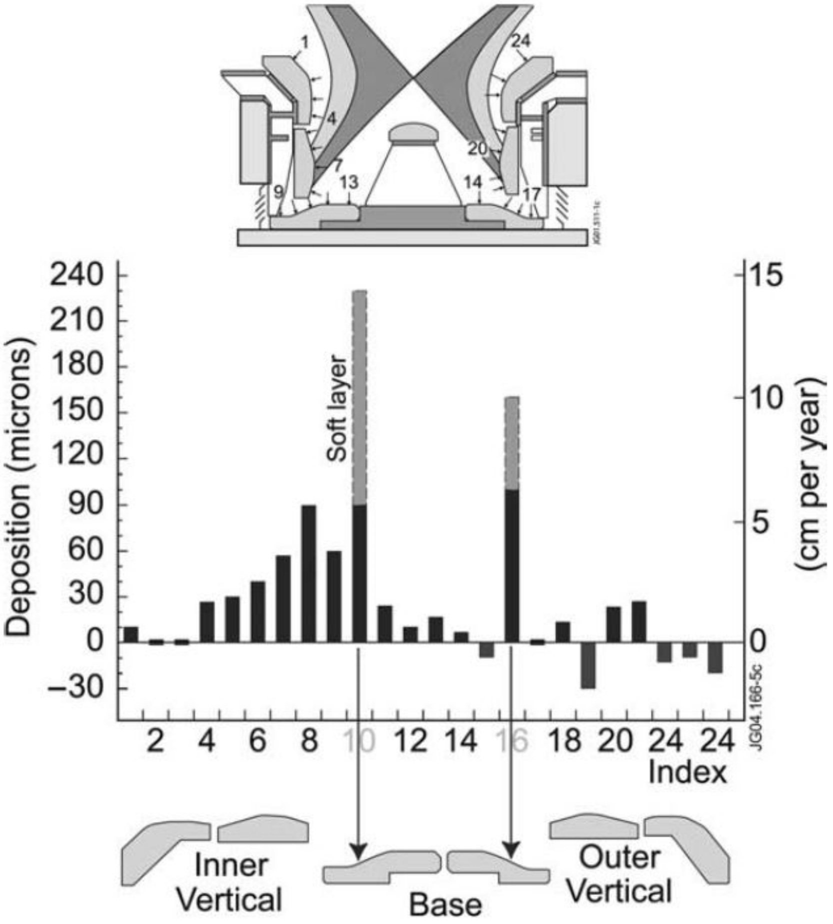

Figure 10 Figure showing net deposition of carbon in the inner divertor region of the MkII-GB divertor in JET, adapted from Matthews 2005 paper[11]. Grey bars indicate compression of the deposits after multiple measurements with calipers. The asymmetry in divertor deposition is assumed to be due to flows in the SOL.

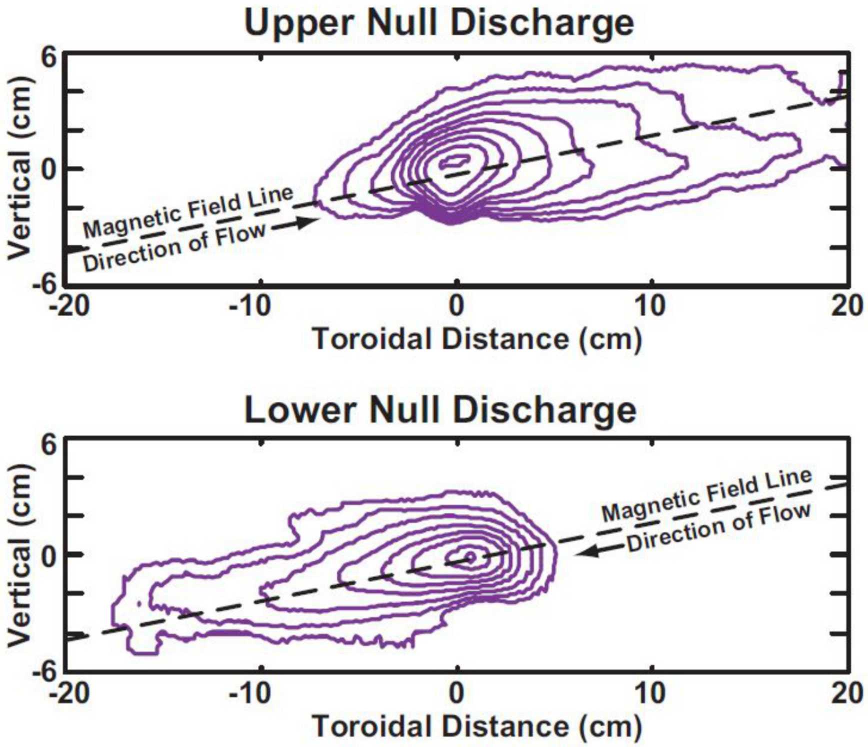

Figure 11 Contours of the emission from C-II in Alcator C-MOD during plume injection. Figure adapted from LaBombard's 2004 paper[29]. The injection location is at the origin, and the plume emission can clearly be seen to be elongated in the direction of the flow. In both the upper and lower null discharges the plume is elongated in the direction leading to the inner divertor.

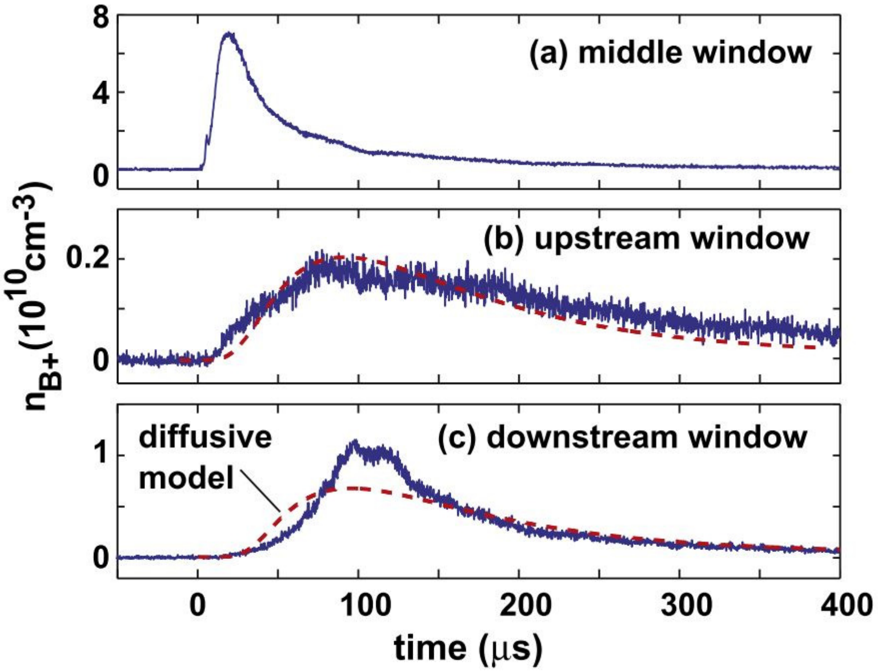

Figure 12 Raw data from filterscopes in blue, and fit from equation 8 in red. Figure taken from Hollmann's 2011 paper[30].

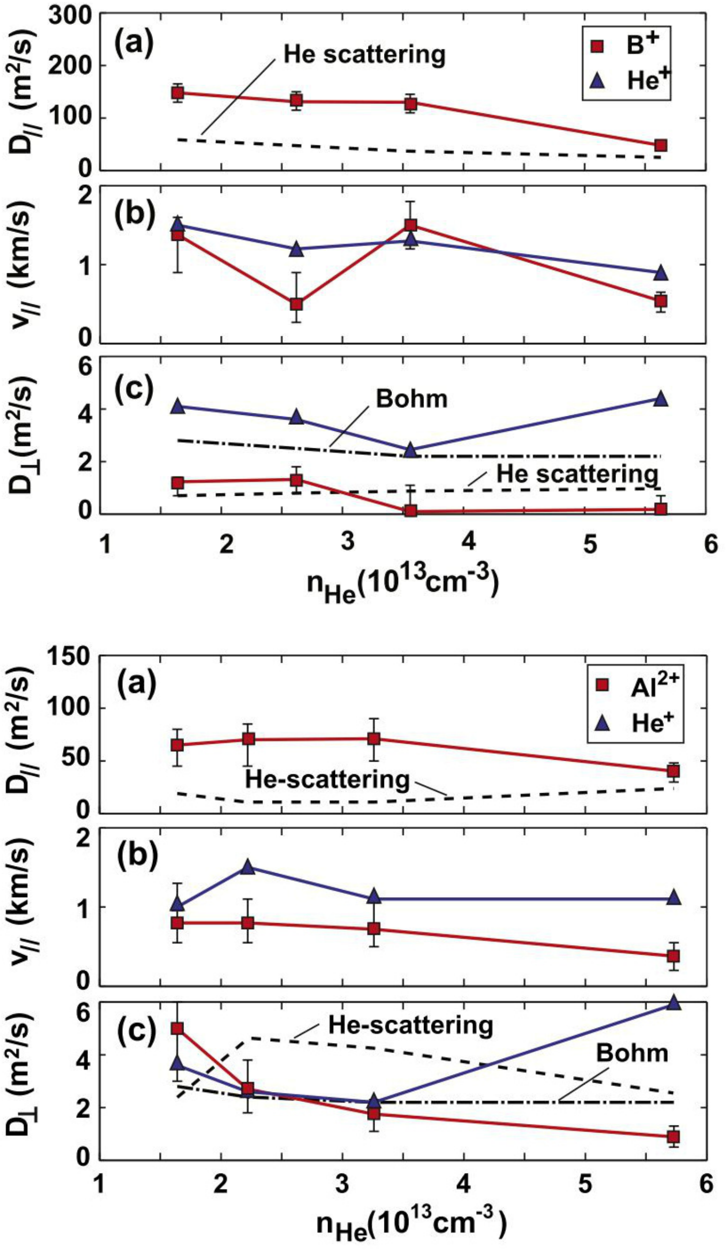

Figure 13 Results from Hollmann's 2011 paper[30] showing the transport parameters determined from the fitted model. It can be seen that the boron velocity is the same as the helium velocity, indicating that the boron is fully entrained in the helium flow. However, the velocity of the aluminum ions appears to only be approximately 50% of the background helium velocity implying the heavier aluminum ions are not fully entrained.

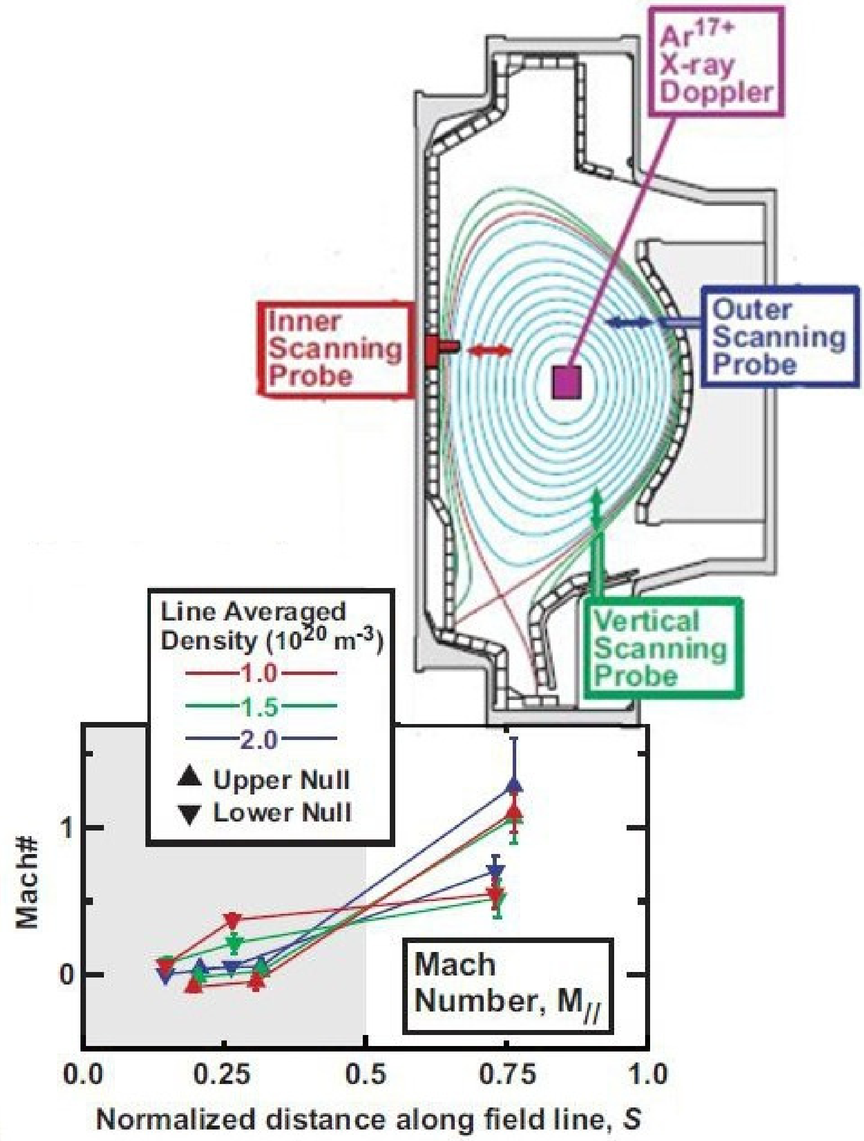

Figure 14 Measurements of the Mach number adapted from from LaBombard's 2004 paper[29]. It can be seen from the plots that the flows in the inner SOL approach Mach 1 in both upper and lower null configurations regardless of the line averaged plasma density.

Chapter 3: Experimental Methods

As noted in the last chapter, understanding the transport of impurities in the SOL of the tokamak is essential for understanding the lifetime of the PFCs and perpendicular transport of impurities into the core plasma. However, there is some evidence from the PISCES linear device[30] that the entrainment of the heavy impurities in the parallel flow could be much longer than classically calculated. The goal of this thesis was to test the frictional coupling of heavy impurities to a lighter flowing background plasma. The results would be directly applicable to the parallel transport of impurities in the SOL of tokamaks and therefore relevant to fusion devices.

The essential plan for the project was to develop a scheme to control the parallel plasma velocity, which would be an experimental knob to adjust the momentum exchange (or entrainment) time for the impurities. It was expected that the plasma velocity could be well characterized through Mach and Langmuir probe measurements. Impurities would be injected through the laser blow off technique, and their position would be tracked by isolating the electronic transitions in the ions. A comparison of the measured velocity from a transport model could then be compared to the background plasma velocity in order to constrain the entrainment time. In this chapter we will describe the experimental hardware chosen to complete the project.

3.1 CSDX

The Controlled Shear De-Correlation eXperiment (CSDX) is a linear plasma device that utilizes an m = 1 helical RF antenna to create a plasma. A schematic of the device and the associated hardware is given in Figure 15. CSDX consists of a 2.8 m long, 0.2 m diameter vacuum chamber surrounded by a series of 28 water cooled, copper coils that produce a solenoidal magnetic field.

The 28 coils are separated into 7 groups, each powered by its own constant-current power supply. This allows for tailoring of the magnetic field geometry. However, for these experiments all coils were operated at the same amperage. The current in each coil can be brought up to 800 Amps providing a range of magnetic fields from 0-2400 gauss.

Base pressures in the device are typically about one microTorr or less. Argon is used as the working gas and is injected at a constant rate of 25 sccm through a port located next to the helical antenna. Neutral gas fill pressures are typically 4.2 mTorr at the source end and 3.1 mTorr at the pump end when the helicon antenna is off. Steady state pressure is accomplished by pumping the argon gas back out of the chamber through a 1000 l/sec turbopump. The vacuum conductance to the pump is adjusted through the use of a butterfly valve located directly above the pump port.

The plasma is produced through an m = 1, helical RF antenna that is mounted over a Bell jar at the end of the vacuum chamber. The antenna is typically powered at 1.8 kWatts. When the antenna is on and operating the measured neutral pressure in the chamber typically drops to around 1.2 mTorr. Presumably this is due to electrons in the plasma ionizing the neutrals and acting as a sink for the neutral gas.

One of the goals of these experiments was to systematically vary the momentum exchange time by adjusting the plasma velocity. For this purpose, it is important to have the other plasma parameters remain relatively constant. In CSDX, typical plasma densities and electron temperature are 10^{13} cm^{-3} and 4 eV, respectively, across the range of magnetic fields available as shown in Thakur's 2014 paper[45]. Both the electron temperature and density remain relatively constant (within 20%) on axis as the magnetic field is changed.

3.2 Mach probe, plasma velocity measurements, and impurity entrainment times

In order to measure the plasma velocity a Mach probe was initially used. A Mach probe is an ion current collecting probe. It is designed with multiple tips that are shielded from the plasma on one side. The design of our probe is shown in Figure 17. It is a 14-tip probe made of 14 tungsten electrodes embedded in an insulating alumina shaft with a diameter of approximately 1 cm. Having 14 tips on the Mach probe allows for redundant measurements of the Mach number. This helps shorten the experimental time and also allows for backup measurements if any of the electrodes should fail. The electrodes are biased negatively with respect to the plasma potential in order to collect only ion current.

For operation the Mach probe is rotated through 2π radians with each tip giving an independent measure of the ion Mach number. The Mach number is determined from the ratio of the ion current densities up and down stream, denoted as $j_{\theta+\pi}$ and j_{θ}, by using the analysis technique from Shikama[46].

$$\frac{j_{\theta+\pi}}{j_\theta} = \exp\left(\mathrm{k}\frac{\sin\alpha}{\alpha}(M_{||}\cos\theta + M_{\perp}\sin\theta)\right) \qquad 9$$

Here, α is the acceptance angle of the probe electrode as described in Figure 17, θ is the angle of the tip normal with respect to the magnetic field, k is a calibration constant, and $M_{||,\perp}$ represents the parallel and perpendicular Mach number.

The swept Langmuir probe measurements of electron temperature, which are given in Thakur's 2014 paper[45], were used to convert the Mach number to the velocity, $v_{||} = M_{||} C_s$, where C_s is the speed of sound. The speed of sound in a plasma is given by $C_s = \sqrt{\frac{T_e}{M}}$, where M is the mass of the ions in the plasma.

In preparation for this work measurements of the plasma velocity were made, which were published with the electron density and temperature measurements[45]. These results are shown in Figure 18. These results indicate an ion flow speed that increases monotonically on axis as the magnetic field increases. The combination of approximately constant electron temperature and density with the steadily increasing plasma velocity appears to be an ideal platform for testing the frictional coupling of impurities to the background plasma.

CSDX has ports available 70 cm and 140 cm downstream of the impurity injection port. These ports will be referred to as port 2 and 3 to indicate the location of PMT 2 and 3 as shown in Figure 15. According to the Mach probe measurements of the velocity, the transit time to ports 2 and 3 will be 2.3 msec and 4.7 msec at 400 gauss

(300 m/s). As the magnetic field is increased the plasma velocity increases monotonically yielding a transit time of approximately 230 microsec to port 2 and 470 microsec to port 3 at the highest magnetic fields (3000 m/s). Over this range of velocities, the entrainment time scales from vanishingly small (2 microsec at a plasma flow speed of 300 m/s) to approximately 6% of the transit time (14 microseconds at a plasma flow speed of 3000 m/s).

The experimental transport timescale for the entrainment experiments done by Hollmann[30] show impurities arriving downstream approximately 100 microseconds after injection. However, the classically calculated entrainment times for these experiments give a timescale on the order of 1 microsecond. Therefore, the momentum exchange time would be two orders of magnitude longer than what is calculated from a binary collision model. Our experimental apparatus should certainly be able to measure a discrepancy of that magnitude. A two order of magnitude discrepancy in this experiment would make the entrainment time 1.4 msec at the highest ion flow velocities, which would be significantly longer than the transit time of the background plasma.

3.3 LBO and Impurity Injection

Based on these results and calculations of the entrainment time we prepared for impurity injection in CSDX. In order to introduce impurities into the plasma the laser blow off (LBO) technique was used. A schematic of the laser blow off apparatus is shown in Figure 21. To perform LBO a glass microscope slide is coated with a thin layer of the desired impurity. A laser pulse travels through the microscope slide and strikes the underside of the coating, ablating the material as a mix of ions, neutrals, and dust particles. The neutral atoms travel into the plasma column where they are ionized by the electrons in the plasma, confined radially by the magnetic fields, and transported along the length of the plasma device.

The microscope slide is housed in a cross-shaped addition to the main vacuum chamber. The slide is mounted on a linear positioner, which allows it to be withdrawn from the cross into an interlock chamber for easy replacement of the slide. For laser ablation of the coating the slide is moved to the center of the cross. Directly beneath the slide is a specially coated window for transmission of laser light.

A Continuum Surelite-I laser with a 10 nsec pulse width was used to ablate the impurities. The laser pulse energy is variable up to ~500 mJoules. For these experiments low pulse powers, of about 20-40 mJoules, was all that was necessary to ablate the coating. The laser pulse was focused onto the coating through a convex-planar lens onto a spot approximately 1 mm in diameter. Some damage to the glass slide is visible after each shot, but the glass slide remained structurally stable even after multiple shots.

The slides were coated with a thin, ~3 micron coating of bismuth with a magnetron sputter coater. The thickness of the film was determined by using a needle profilometer, which gives a high precision measure of thickness variations. By masking a portion of the glass slide before coating it is possible to measure the absolute thickness of the coating. The variation of the thickness was approximately 30% over the area of the slide.

The transport of the impurities was detected through a series of "filterscopes" similar to those used by Hollmann[30]. Each filterscope was comprised of a photomultiplier tube with a 10 nm bandpass filter centered at 520 nm in front of the detector. Initially a convex lens was placed in front of each detector to maximize the amount of light collected. However, the light emission from the impurities turned out to be significantly higher than anticipated. A neutral density filter was placed in front of the detectors as necessary to reduce the intensity of the collected light.

The 1-Dimensional advection-diffusion equation, $\frac{\partial C}{\partial t} = V_z \frac{\partial c}{\partial z} - D_{||} \frac{\partial^2 c}{\partial z^2}$, was used to model the impurity transport. Here, c refers to the concentration of impurities, V_z and $D_{||}$ and the velocity and diffusion parallel to the field lines. The modeling of the impurity transport is discussed thoroughly in the following chapter.

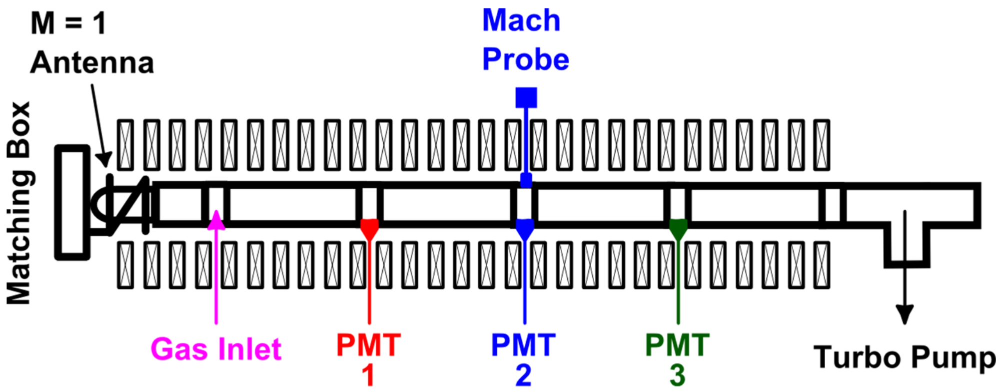

Figure 15 Diagram of CSDX showing the vacuum chamber, surrounded by the 28 magnetic coils. On the left side of the diagram is the matching box, which adjusts the impedance of the source to match the impedance of the plasma, and the m = 1 helical antenna. On the far right side of the diagram is the vacuum T, which leads to a turbo pump (not pictured) that maintains constant pressure in the device. Diagnostic access to the machine is done through a series of ports located along the length of the vacuum chamber. The working gas (in this case argon) is injected at the first port downstream of the source. The impurities were injected using laser blow off at the port in front of PMT 1 (in red) located at a window to monitor the light emission. The transport of the impurities downstream was monitored with two more PMTs, labeled PMT 2 and PMT 3, located 70 and 140 cm downstream of the injection site, respectively. Mach probe measurements were made at the same port as PMT 2.

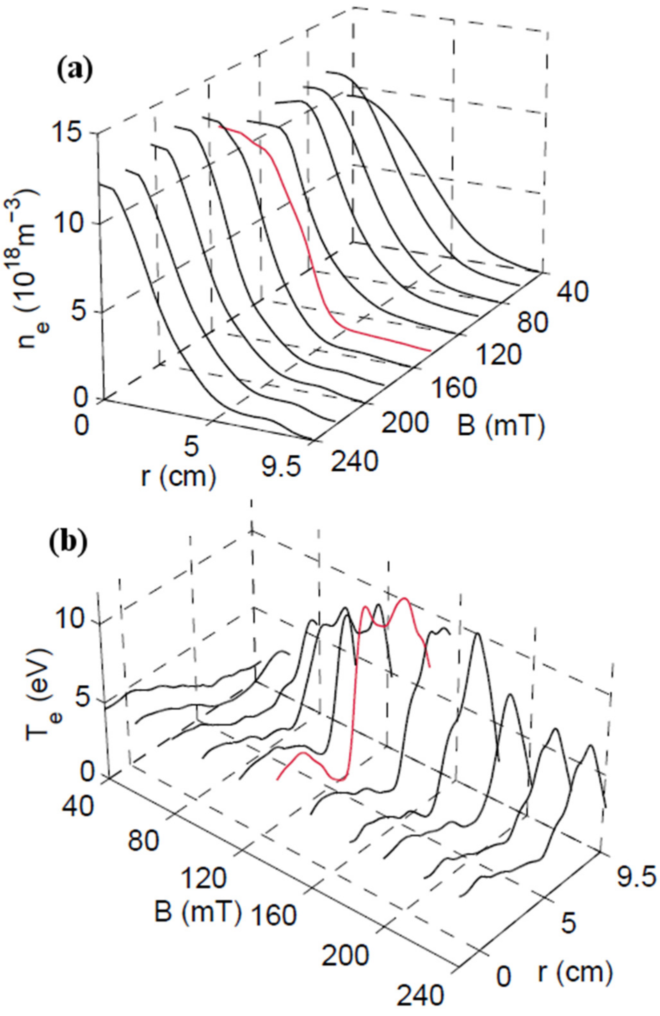

Figure 16 Figure adapted from Thakur's 2014 paper[45]. As can be seen in (a) most of the plasma column is within a five centimeter radius (r = 5). Densities on axis are typically about 10^{13} cm^{-3}. Electron temperatures are around 4 eV on axis as can be seen in (b). The Langmuir probe shows some evidence of high electron temperatures in the far edge of the plasma where the density is very low. These hot electrons are not important for the experiments in this thesis. They are discussed further in the 2014 paper by Thakur[45].

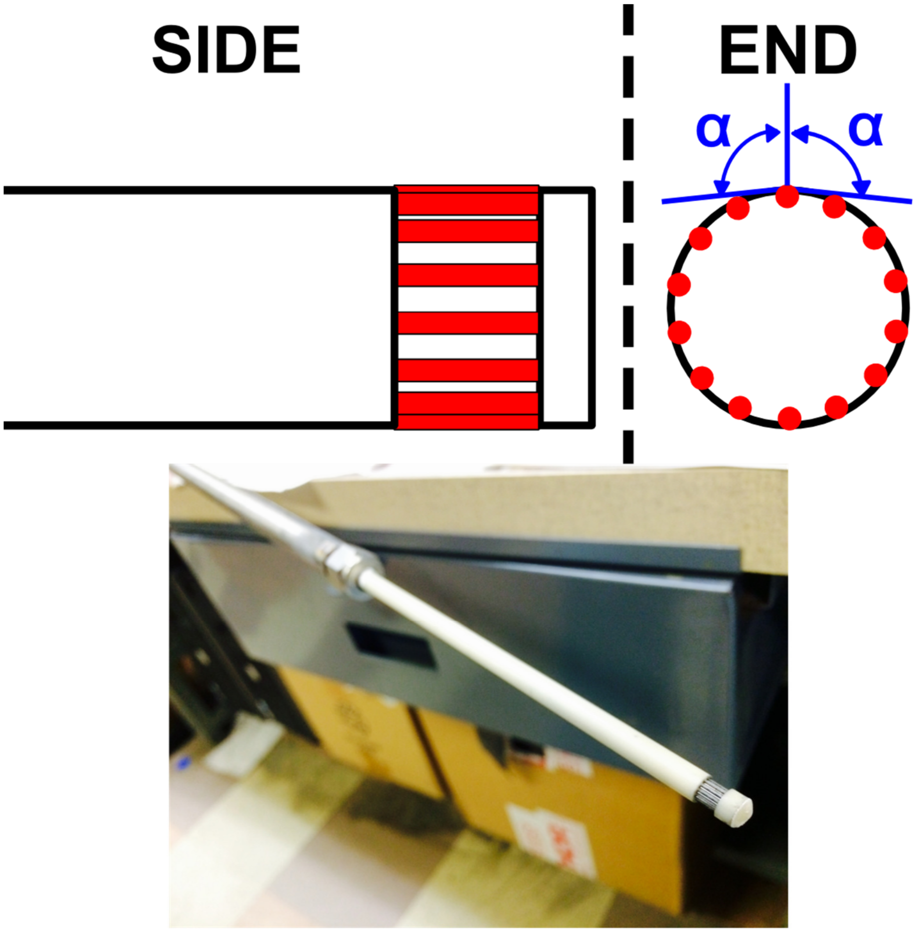

Figure 17 Schematic showing side and end views of the Mach probe. The tungsten electrodes are shown in red. This 14-tip design has 14 tungsten electrodes inserted in an insulating alumina probe shaft. A window is cut around the circumference of the probe shaft in order to expose the tips to the plasma. The electrodes collect ion current from the plasma through an acceptance angle, α, shown on the end diagram in blue. Shown below is a photograph of the probe and electrodes.

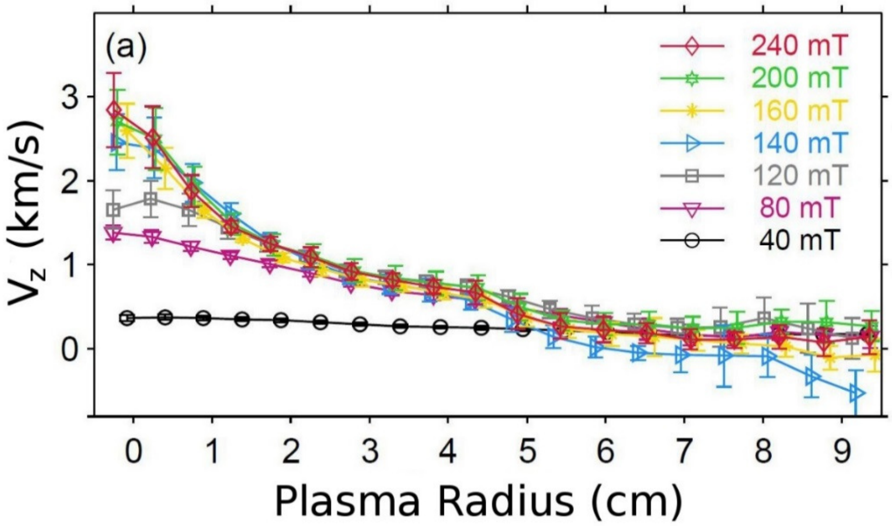

Figure 18 Plasma velocity as determined from Mach probe data interpreted using equation 10. Figure is adapted from reference [45]. These results indicate a plasma velocity that is increasing about an order of magnitude on axis from a Mach number of 0.1 to 0.9.

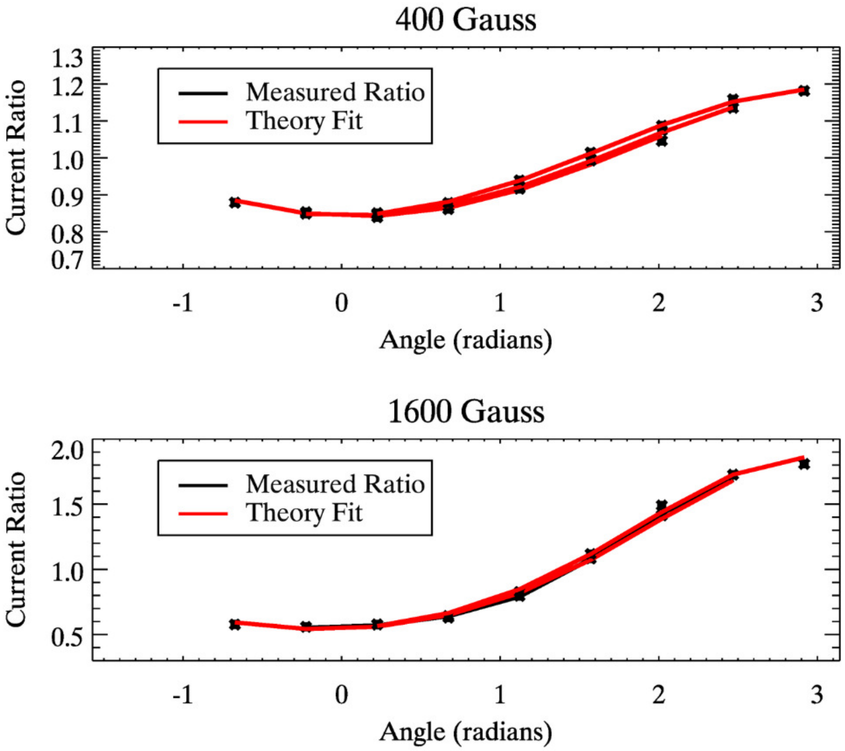

Figure 19 Plot of ratio of ion saturation currents for tips separated 180 degrees (shown in black). Fit from equation 10 (shown in red) is determined by adjusting $M_{\parallel}$ and $M_{\perp}$ until best fit is achieved. It can be seen that the fitting function fits well at both low and high fields even though the derived Mach number is incorrect.

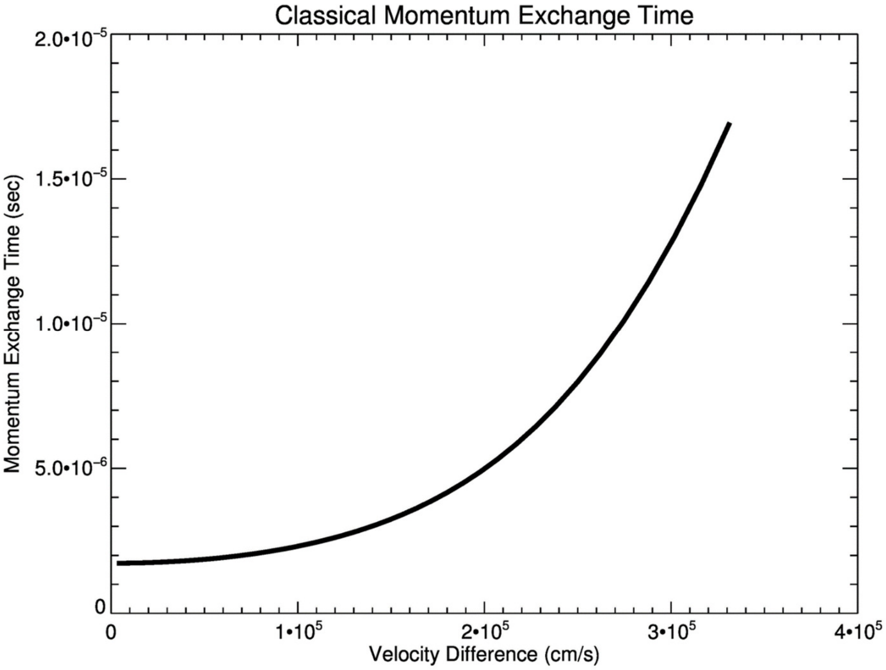

Figure 20 Calculation of the momentum exchange time for different background plasma flow velocities[21].

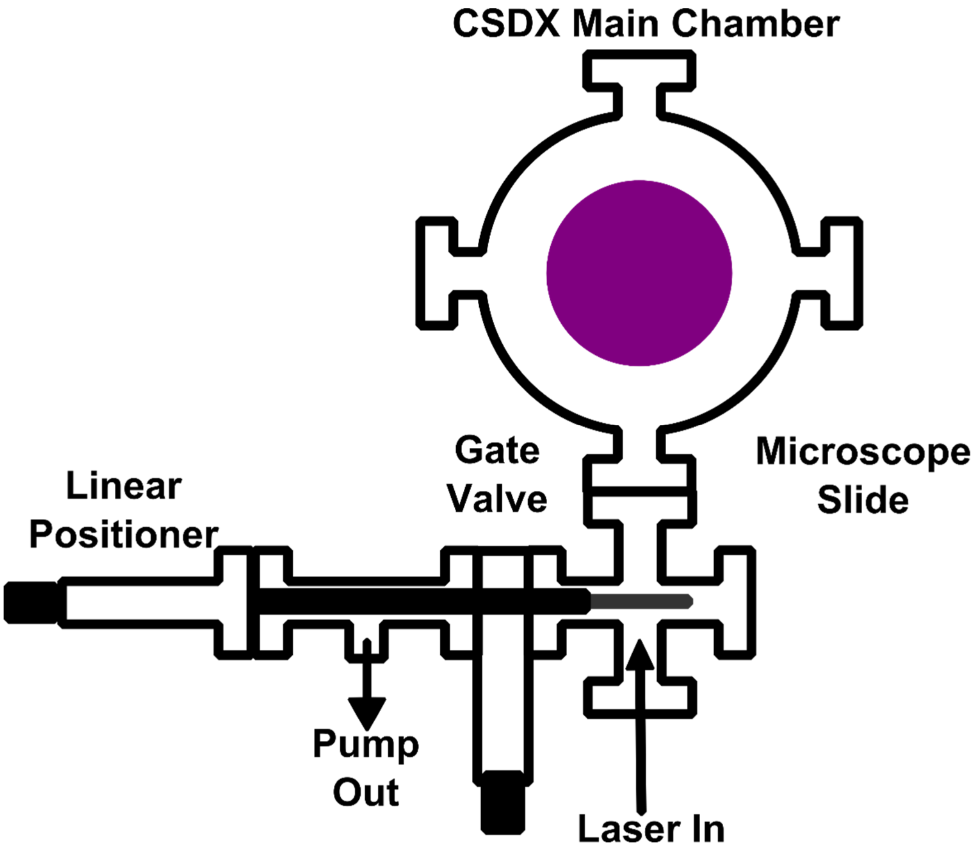

Figure 21 Diagram showing the cross section of the laser blow off apparatus. A coated microscope slide is placed on a linear positioner. The linear positioner can be fully retracted into an interlock portion of the vacuum chamber to enable a quick change of the slide. The laser beam travels along the axis of one set of ports on the vacuum cross and through the back of the microscope slide to ablate a small dot of the coating. The ablated coating travels up into the vacuum chamber as neutrals and dust particles. The neutral particles are ionized by collisions with electrons in the plasma, confined by the magnetic fields, and transported by collisions along the length of the device.

Chapter 4: Initial comparison between Mach probe and Laser-impurity blow-off results

4.1 Model and Apparatus:

In an initial set of experiments, we used the Mach probe described in Chapter 3 to infer parallel flow along the r=0 axis of CSDX for a variety of magnetic field conditions. As can be seen from Figure 18, the measurements made with the Mach probe indicate a monotonic increase in the inferred plasma flow speed as the magnetic field increases. These initial results, taken at face value, suggested that the CSDX Ar plasma flow velocity could be controlled via the strength of the axial magnetic field, while maintaining other conditions constant, making these target plasmas an excellent platform to perform experiments measuring the entrainment, or momentum exchange, time between heavy impurities and the background plasma.

In order to quickly introduce very small amount of impurities into the CSDX plasma we utilized the laser blow off (LBO) system, shown schematically in Figure 15 and Figure 21 in Chapter 3. By tracking the motion of the impurities along the length of the plasma device via an array of PMT detectors, and by comparing the actual arrival time to the calculated transit time we can determine an upper limit on the momentum exchange time. The LBO technique uses a pulsed laser to ablate material from a thin coating on a blank glass slide.

Bismuth was ideal for these experiments because it has the largest mass of any non-radioactive element, 209 amu, and provides a large impurity ion: main plasma ion mass ratio (which maximizes the entrainment time). Note that here CSDX was operated with argon as the working gas and the mass ratio of bismuth to argon is 5.2, which is close to the mass ratio of carbon to deuterium, found in many current tokamak experiments. In addition, Bismuth is non-toxic, non-flammable, and weakly reactive with atmospheric gasses. Most importantly for our experiments, bismuth has spectral lines available that are spectrally isolated from both Ar-I (neutral argon) and Ar-II (ionized argon) lines in the plasma. Additionally, bismuth has a very low vapor pressure, which is 0.1% or less of the background neutral gas pressure at temperatures of up to 680 kelvin. This ensures that the bismuth that is visible in the plasma comes from the initial LBO injection only and not from the walls outgassing impurities.

The entrainment time can be calculated as[21] $\nu^{\frac{\alpha}{\beta}}{}_{s} = \left(1 + \frac{m_\alpha}{m_\beta}\right) \psi\left(x^{\frac{\alpha}{\beta}}\right) \nu_0$. Here $\psi(x) = \frac{2}{\sqrt{\pi}} \int_0^x t^{1/2} e^{-t}\, dt$, $\nu_0 = 4 \frac{\pi e_\alpha^2 e_\beta^2 \lambda_{\alpha\beta} n_\beta}{m_\alpha^2 V_\alpha^3}$, $x^{\frac{\alpha}{\beta}} = \frac{m_\beta V_\alpha^2}{2\, k\, T_\beta}$, $\lambda_{\alpha\beta}$ is the coulomb logarithm, and α and β denote the test particle and background particles, respectively. The velocity of the particles can be multiplying the Mach number by the sounds speed, $c_s = \sqrt{\frac{T_e}{m_\beta}}$, which gives velocities on axis of about 300 m/s at 400 gauss to 2.8 km/sec at 1600 gauss. At these velocities the time scale for momentum exchange of the impurities with the background plasma, a.k.a. the entrainment time, is between 2 μSec and 17 μSec; the transit times, defined as the time for the impurity cloud to be transported from the injection location to the first port downstream, is estimated to be between 2.3 mSec and 230 μSec. Again, given the velocities interpreted from the Mach probe this looks like an excellent platform to study impurity entrainment with the ratio of entrainment time to transit time being vanishingly small at 400 gauss (entrainment to transit time ratio of 9:10,000) to nearly ten percent (ratio of 7:100). With this system we should be able to successfully measure the momentum exchange time and limit it to within an order of magnitude of the classically calculated (binary collision model) value.

After injection the impurity cloud is monitored using a series of three photomultiplier tubes (PMTs). Each PMT is equipped with a bandpass filter centered at 520 nm with a 10 nm full width half max (FWHM). One PMT is located at the injection site. Two more PMTs are placed downstream at ports 70 cm and 140 cm downstream of the injection site as shown in Figure 15. The bismuth ions emit light at ~521 nm through the 6p7p $(1/2,3/2)_2$ -> 6p7s $(1/2,1/2)_1$ transition.

The impurities are collisionally excited by electrons in the plasma, which yields a radial light emission profile that is a convolution of both the bismuth ion and the electron density. This results in the center of the plasma (r = 0) being the primary source of light emission as shown in Figure 22. As a consequence of this, even though the PMTs line integrate across the radius of the plasma, the light emission may be considered to be indicative of the location of the bismuth ions within the first centimeter of the plasma radius.

As can be seen from Figure 18, the velocity profile is relatively flat within the first centimeter of plasma radius. For this reason, we use a one dimensional advection-diffusion equation to model the impurity transport, $\frac{\partial c}{\partial t} = V_z \frac{\partial c}{\partial z} - D_{||} \frac{\partial^2 c}{\partial z^2}$. Assuming a delta function in space as the initial condition, the solution to the 1-D advection diffusion equation is well known: $C(x,t) = \frac{C_0}{\sqrt{4\,\pi D_{||} t}}\, e^{-\frac{(x-V_z t)^2}{4\, D_{||} t}}$. In both these equations c represents the density of impurity atoms, V_z is the velocity of the background plasma along the magnetic field lines, and $D_{||}$ is the diffusion parallel to the field lines.

The solution to the 1-D advection diffusion equation is linear in the initial concentration, C_0. This is convenient for our experiments because it means that no photon counting is necessary, and the PMT voltage output can be rescaled arbitrarily without affecting the physical result. The fluid transport coefficients, V_z and $D_{||}$, can be modeled by fitting the PMT output to the solution of the 1-D advection diffusion equation. The raw data and the fits are shown in Figure 23 for the 400 gauss case; the fits indicate a parallel velocity of 300 m/s ± 56 m/s and a parallel diffusion coefficient of 1.1 m^2/s ± 0.6 m^2/s. It can be seen from the figure that the fit models the data well.

Clearly we are neglecting some of the physics in order to use this simplified model. Most importantly, the initial condition is not a delta function. When attempting to get a measurement of the velocity of the impurity cloud this is not a major issue. The geometry of the laser blow off apparatus is designed so that the injection is symmetric around the axis of the injection port on the machine. Since the solution is a shifted Gaussian function, the velocity measurement is essentially a time of flight measurement and is unaffected by the initial width of the impurity cloud. Interpretation of the diffusion coefficient, on the other hand, will depend strongly on the initial condition. This will be addressed later in the chapter on parallel diffusion.

Clearly transport is always inherently three dimensional. We are neglecting azimuthal transport by assuming cylindrical symmetry, $\frac{\partial c}{\partial \theta} = 0$. This assumption is confirmed by the 2-D camera data shown in Figure 22. We are neglecting radial velocity shear, $\frac{\partial V_z}{\partial r} = 0$. The largest radial shear in the parallel velocity is between 1 and 5 centimeters where the light emission is decreasing in magnitude. If the radial shear were to be important for the data interpretation the effect would be a downshift in the velocity and an enhanced diffusive term.

Finally, we are neglecting the parallel gradient in the parallel velocity (assuming $\frac{\partial V_z}{\partial z} = 0$). The solution presented above assumes that the parallel velocity is constant along the path traveled by the impurities. The resulting velocity inferred from fitting the blow off data will be a path averaged velocity of the impurity cloud as it is transported from the initial injection site.

4.2 Results and discussion:

For comparison with the impurity transport, the relevant quantity is the velocity of the plasma on axis. This velocity, as interpreted from the Mach probe, is shown in Figure 24. Also shown in Figure 24 is the best fit for $V_{||}$ from the LBO impurity transport experiments. The velocity of the impurity cloud, inferred by fitting the solution to the 1-D advection diffusion equation above, remains nearly constant at about 300 m/s in contrast to the Mach probe data. This is a stark discrepancy; the difference in velocities is nowhere near what would be expected based on the experimental errors.

Both the Mach probe measurements and the LBO measurements are highly repeatable and present small random errors.

There are a number of possible obvious candidates to explain the discrepancy between the LBO flow speed and the inferred main ion flow speed. First, the classically calculated momentum exchange time (frictional coupling or entrainment time) could be shorter than the actual entrainment time. Second, the velocity shear could be more important than anticipated. Third, the bismuth ions could be being burned out to a higher ionization state in the center of the plasma. Finally, the Mach probe interpretation may be erroneous. We will find that the only reasonable conclusion is that there is an error in the Mach probe interpretation. However, for thoroughness, let us first examine and eliminate the first three possibilities.

The first, and simplest, potential cause to address is the frictional coupling time, $\nu^{\frac{\alpha}{\beta}}{}_{s} = \left(1+\frac{m_\alpha}{m_\beta}\right)\psi\left(x^{\frac{\alpha}{\beta}}\right)\nu_0$. Under an assumption of constant momentum exchange rate, the equation for the acceleration of the impurities, $\frac{d\overrightarrow{V_{rel}}}{dt} = -\nu_{s}^{\frac{\alpha}{\beta}}\overrightarrow{V_{rel}}$, can be easily solved (here $V_{rel} = V_\alpha - V_\beta$). Under the constant momentum exchange time approximation the velocity of the impurity cloud can be written as: $V_\alpha(t) = V_\beta(1-\exp(-\nu_s t))$.

Through a simple calculation it is easily seen that the momentum exchange time would have to be orders of magnitude larger than the classical time in order for the experimental plasma velocity and impurity transport data to be consistent. A rearrangement of the above equation yields an expression for the "measured" momentum exchange time, $\nu_{s,meas} = -\frac{V_\alpha}{L_{port}}\ln\left(1-\frac{V_\alpha}{V_\beta}\right)$, where L_{port} is the distance of the port downstream from the impurity injection location where the velocity measurement is made. At 800 gauss the momentum exchange time would have to be nearly 600 times slower than the classically calculated value, and at 1600 gauss the momentum exchange time would have to be over 1200 times greater than the classically calculated value. This is an enormous discrepancy. Additionally, this would imply that the momentum exchange time has either: a linear dependence on the magnetic field, which has no basis in theory, or the momentum exchange rate would have to be multiplied by a factor proportional to V_{rel}^{-1}, which also has no theoretical basis. Therefore, we are conclude that a long momentum exchange time is probably unphysical.

The next option is that the velocity shear is more important than anticipated. While the primary source of light emission is on the axis of the plasma column there is some small amount of emission from the impurities detectable all the way out to 5 cm as can be seen in Figure 22. As mentioned above, the effect of the velocity shear would appear as an enhanced diffusion and a downshift in the velocity. However, as can be seen in Figure 18 the velocity of the background plasma inferred from the Mach probes is greater than 300 m/s from r = 0 to 5 cm with the exception of the 400 gauss case. In fact, for all cases other than the 400 gauss case, the Mach probe reports velocities at or above 1000 m/s until a plasma radius of ~5 cm. Even if we were collecting light from the outer regions of the plasma, there would not be an appreciable effect on the observed arrival time of the Bi^+ light emission. Thus, it seems unlikely that the radial shear in the parallel velocity $\frac{\partial V_z}{\partial r}$, is responsible for the reduced parallel velocity of the impurity cloud.

Finally, we address the possible burnout of the Bi^+ ions. The measurements show that Bi^+ light emission from the impurity ions is highest in the center of the plasma. The center is also where the electron density and temperature is the highest, which may contribute to burnout of the Bi-II state. The electrons in the CSDX plasma have a typical temperature of about 4 eV. The ionization energy of neutral bismuth (Bi-I) is 7.3 eV, while the ionization energy of the first ionized state of bismuth (Bi-II) is 17 eV[Lide:2005]. By a crude estimate this means the cross section for the production of the Bi^{2+} state will be approximately 8% of that to the first ionized state. the hollowing of the Bi^+ profile needed to explain the discrepancy between Mach probe and impurity entrainment would not be subtle. Since the plasma velocity inferred from the Mach probe is at 1000 m/s or above for plasma radii less than 5 cm (again, this is excepting the 400 gauss case) the bismuth ion profile would have to be hollow all the way out to 5 cm in order to resolve the discrepancy between the two parallel flow speeds. This would be obvious from the camera data, and there is absolutely no evidence of this (see Figure 4). Therefore, we are forced to conclude that Bi^+ burnout is not the cause of the discrepancy between the inferred impurity velocity and the inferred plasma velocity from the Mach probe.

4.3 Conclusions:

It is clear that the Mach probe data and the impurity blow off data are not consistent with each other, and the other possible explanations to resolve the discrepancy do not seem plausible. Thus by a process of elimination, we arrive at the tentative conclusion that the method used for interpretation of results from the Mach probe must be flawed. Because of this discrepancy between the Mach probe data and the impurity transport measurements, we decided to also perform LIF measurements parallel to the magnetic field, and did so via a collaboration between our group and Professor Earl Scimee's group at West Virginia University. The original plan was focused on performing laser induced fluorescence (LIF) measurements of the argon ion velocity and temperature perpendicular to the magnetic field.

Motivated by the study presented in this chapter, we included some parallel flow measurements in the LIF work. The LIF experiments revealed a systematic error in the method used to interpret the Mach probe data. The next chapter of the thesis discusses these new experiments in detail, summarizes this systematic error, and introduces a physics explanation for the error. This physics insight then permits us to develop and apply a correction to the interpretation of the Mach probe data that brings the probe interpretation into agreement with the LIF measurements.

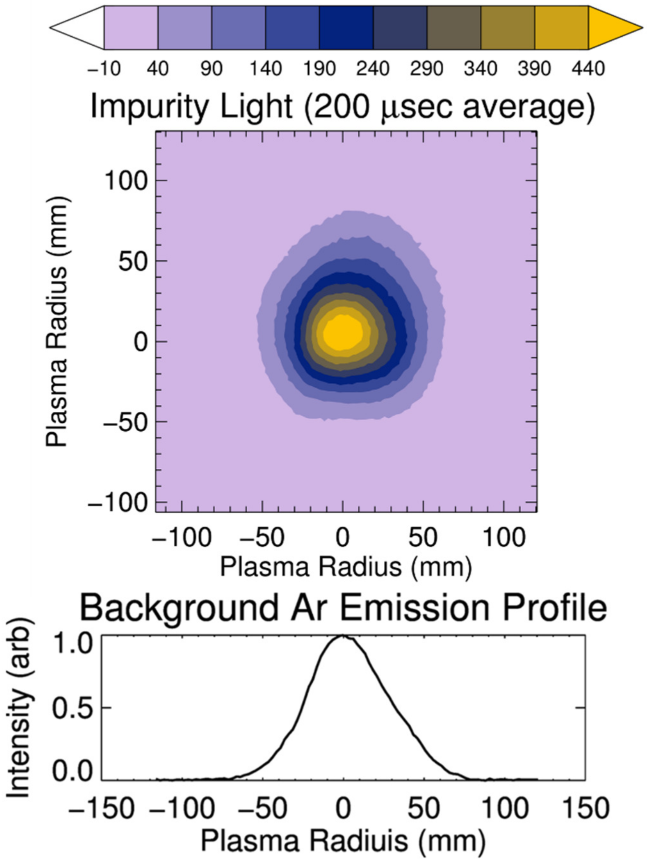

Figure 22 Image taken with high speed camera showing cross section of plasma. Camera is focused at the axial position of the injection port with 520 nm bandpass filter in front of lens. Image is an average over 200 microseconds. Small amounts of plasma light leak through the filter, and this background plasma light emission was averaged over for two seconds and then subtracted from the signal. It can clearly be seen that the dominant light emission is coming from the axis of the device (first one to two cm of plasma radius). Second plot shows radial profile of background argon emission that is visible through the bandpass filter.

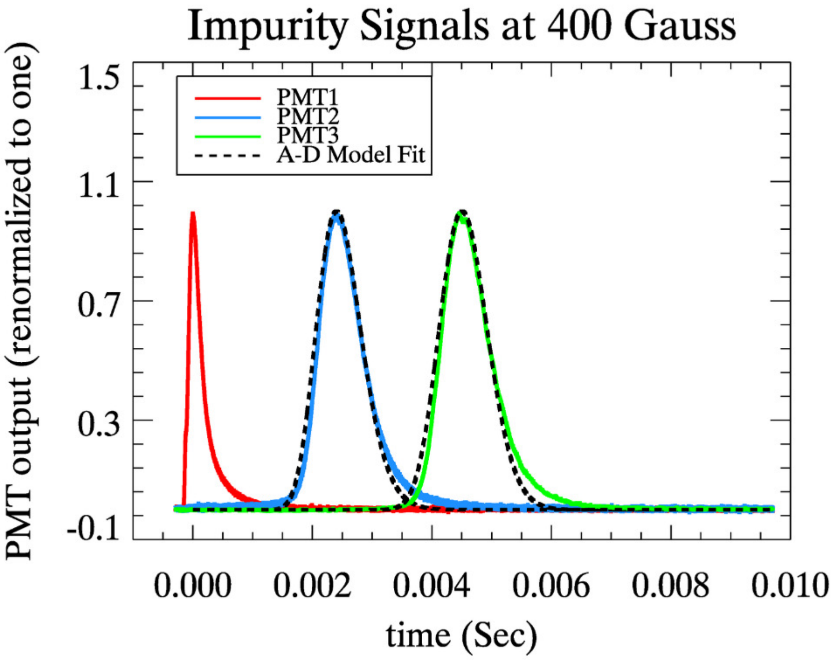

Figure 23 Data from the LBO experiments collected from the PMTs. Data is an average of about 60 individual shots; all signals are renormalized to a max height 1. A 1-D advection diffusion model is used to fit to the light emission from the impurities, which is shown here as the dotted lines overlayed on the data. Good agreement is found between the model and data downstream of the injection site. Parallel fluid transport coefficients of the impurities, V_z and $D_{\|}$, can be determined from the model fit.

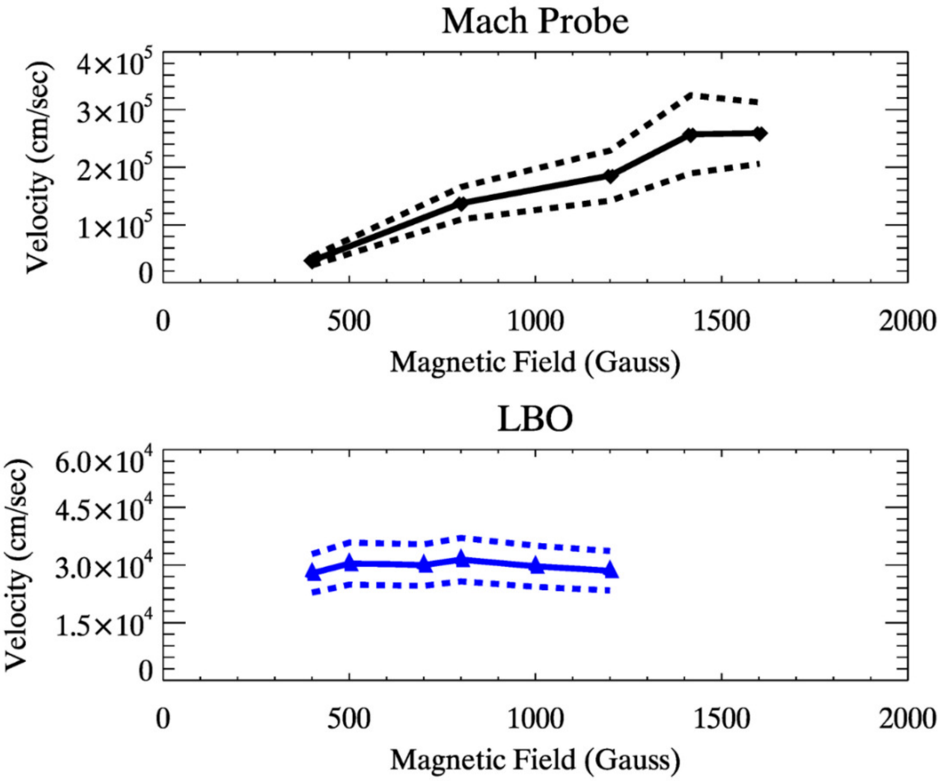

Figure 24 Top plot is Mach probe data at r = 0. Showing monotonic increase in interpreted parallel velocity across range of magnetic fields from 400 to 1600 gauss. Primary uncertainty in interpreted velocity of background plasma comes from uncertainty in the acceptance area of the probe. Bottom plot is a plot of the velocity of the impurity cloud as interpreted from the 1-D advection diffusion model. The Mach probe and impurity transport data show good agreement at 400 Gauss. However, as the magnetic field is scanned up to 1600 gauss the impurity cloud velocity remains at 300 m/s, in stark contrast with the Mach probe measurements.

Chapter 5: Overestimation of Mach Number due to Probe Shadow

In this chapter we present results for measurements of the mean fluid flow of an argon plasma performed with both Mach probes and LIF. All experiments were performed in the CSDX helicon plasma device, which is described earlier. We show results for the plasma flow measured on-axis and compare the values from each technique. The results show that the probe's own shadow perturbs the measurements when the ion-neutral mean free path (λ_{i-n}) is shorter than the characteristic length of the geometric shadow. We then discuss the differences between the two diagnostic measurements and introduce a geometric probe shadow model to account for the differences between the measurements. The model is then used to develop a correction factor which accounts for this shadowing effect and provides for accurate probe-based Mach number measurements.

5.1 Experimental Apparatus:

These experiments described in this paper were performed on the upgraded Controlled Shear Decorrelation eXperiment (CSDX)[45], a linear plasma device 2.8m long and 0.2 m in diameter. A schematic of CSDX is shown in Figure 15. Insulators are placed on both ends of the device so that the plasma flux terminates at an insulating boundary [47,48]. The plasma is produced using a 13.56 MHz, 1.8 kW, m = 1 RF antenna. The m = 1 helical antenna is placed over a 15 cm diameter bell jar that is mated to the end of the vacuum chamber. The plasma is confined radially by a series of 28 axisymmetric magnetic coils capable of creating axial magnetic fields up to 2400 gauss.

Argon was used as the working gas; it is injected radially from a port located at the wall of the device at the source end of the device, and a mass flow controller (MFC) is used to maintain a constant influx of neutral argon gas at a rate of 25 SCCM. A 1000 l/sec turbo molecular pump at the far axial end of the machine a was used to maintain a low neutral pressure of 4.2 mTorr at the source end and 3.2 mTorr at the pump when the RF antenna is off. When the antenna is on the plasma acts as a sink for the neutrals and the pressure at the wall is approximately 1 mTorr along the length of the device. Typical electron temperatures and densities are 4 eV and 10^{13} cm^{-3} as measured by an RF-compensated Langmuir probe. Plasma parameters do not vary by more than 50% over the range of magnetic fields used in these experiments[45].

For the experiments in this paper a Mach probe was used to measure the plasma velocity parallel to the magnetic field. The location of the Mach probe is shown in Figure 15. The probe was constructed out of a pulled alumina shaft, approximately 0.5 cm in diameter with 14 bore holes. Tungsten rods housed in each of the bores act as electrodes. A small window was cut azimuthally around the circumference of the rod to expose the tungsten electrodes to the plasma. This gave each tip an ion acceptance angle of approximately $4\pi/7$ radians as shown in Figure 17 in Chapter 3. The tungsten rods were negatively biased at V_{bias} = -80V with respect to the chamber wall, which is about 50 V below the floating potential[45] in order to collect only the ion saturation current.

The Mach probe was inserted radially into the center of the plasma at a rate of ~3 cm/sec using a stepper motor under computer control. The ion saturation current was measured with a current following amplifier connected to a 0.5 MHz bandwidth DAQ system. The Mach number is determined from the measured upstream and downstream current densities of the probe using the method from Shikama[46]:

$$\frac{j_{\theta+\pi}}{j_\theta} = \exp(\mathrm{k}\frac{\sin\alpha}{\alpha}(M_{||}\cos\theta + M_{\perp}\sin\theta)) \qquad 10$$

Where α is the acceptance angle of the probe tip, θ is the angle of the tip normal with respect to the magnetic field line, j_θ and $j_{\theta+\pi}$ are the ion saturation current densities collected π radians apart, and k is a calibration constant. The probe was rotated through 2π radians in 14 equal increments to obtain independent measurements of the Mach number from each tip and eliminate effects due to differing probe tip areas. Since we used the rotation method of measurement we can use the collected ion current directly without needing to take a precise measurement of the probe tip area.

Different plasma parameters and different models for the ion current collection call for different values of the calibration constant, k[49,50]. Simulations approximating ion current to a sphere with a collisional presheath have been performed by Patacchini and Hutchinson previously [51]. In these studies, the flow was parallel to the magnetic field and the level of magnetization was represented by the parameter $\beta = R_p/R_L$, where R_p is the probe radius and R_L is the larmour radius. Over a range of β = 0 ->1, these simulations showed an increase in the value of the calibration factor, k, with increasing magnetic field for weakly magnetized plasmas. Our experiments run over a range of β from 0.2 to 0.7, but show an order of magnitude increase in Mach number. The change in calibration factor can only account for approximately 30% increase in the Mach number, However we see an increase of an order of magnitude in the Mach number over the range of magnetic fields used in our experiments.

In addition to the work described above, collisionless simulations over a wider range of magnetic fields has been carried out[52] with flows containing components both parallel and transvers to the magnetic field. However, these calibration factors represent even higher values for the Mach numbers with a given ratio of upstream-downstream ion currents. Thus, for our experiments we use the unmagnetized calibration factor of k = 1.34 from Hutchinson's previous work[50], a value that has been used in the past for weakly magnetized plasmas[46].

The ion saturation current signals are averaged over 100 mSec periods Which gives measurements averaged over a ~3 mm in radial extent, and which averages out short period fluctuations (> 10 Hz). Although data was taken for the full radial profiles, only the on-axis data is shown here for comparison with the LIF data measurements. Full radial profiles of the uncorrected inferred Mach number were published previously[45].

An LIF system was also used to measure the absolute parallel velocity for comparison with the Mach probe measurements. The three level scheme originally described by Severn[53] was used, which stimulates a transition from the Ar-II metastable $3d^4F_{7/2}$ state to the $4p^4D_{5/2}$ state causing a photon to be re-emitted through a transition back to the $4s^4P_{3/2}$ state as shown in the diagram in Figure 25. The magnetic field causes this transition to broaden into one group of linearly polarized pi transitions with $\Delta M = 0$

and two orthogonal, circularly polarized groups of sigma transitions with $\Delta M = \pm 1$ due to the Zeeman effect, where M is the magnetic quantum number (the z projection of the total angular momentum).

A diagram of the optical setup for the LIF system is shown in Figure 26. The laser used was a Toptica TA100 tunable diode laser with a line width of 1 MHz and a mode hop free range of up to 30 GHz. One 8% beam splitter was used to redirect a portion of the beam into a Bristol Instruments 621-VIS wavemeter, which measured the wavelength with an absolute accuracy of ±0.0001 nm; this corresponds to an uncertainty in ion velocity of approximately ±45 m/s. A second 8% beam splitter was used to redirect a portion of the beam through an iodine cell. The measurements of the iodine fluorescence spectrum confirm the measurements from the wavemeter and are consistent with two other independent measurements [53,54]. A more detailed description of the iodine spectrum is given in the appendix, which will be beneficial for future groups using this technique.

Laser light centered at 668.6139 nm was injected on axis, parallel to the magnetic field, from the pump end of the plasma device as shown in Figure 15. The laser frequency was scanned over 10-20 GHz to capture the full ion velocity distribution function (IVDF). A quarter wavelength plate was inserted in the beam path after the splitters to change the polarization of the laser light from linearly to circularly polarized. By rotating the quarter wave plate and monitoring the emitted light we are able to isolate the individual, circularly polarized sigma branches. The circularly polarized, $\Delta M = 1$ component of the transition was used for our LIF experiments. The spectrum is symmetric; so, the ΔM= -1 component would have worked equally well. The spectrum showing the pi and both sets of sigma transitions is shown in Figure 27 with the ΔM= 1, sigma excitation branch used in our experiments shown in blue. The emitted florescence is collected through a side port at the measurement location using a focusing optic and 1 nm width bandpass filter centered at 443 nm in front of a PMT. This isolates the $4p^4D_{5/2}$ to $4s^4P_{3/2}$ transition from any nearby transitions in the plasma as much as possible.

The collection optics were chosen so that the focal point is on the plasma axis. The overlap between the focusing optics and the laser beam forms a collection volume of approximately 3 mm^3. Optical layout and collection area is illustrated in Figure 32. Since this transition can also be collisionally excited by electron impact, phase synchronous detection was performed by modulating the beam intensity with a beam chopper at 1 kHz and using a lock-in amplifier in order to increase the signal to noise ratio. For the data points shown here the minimum signal to noise ratio (defined as $SNR = \frac{A}{\sigma_{noise}}$, where A is the amplitude of the fit and σ_{noise} is the rms of the residual) is 3.5 and the maximum is 80. A histogram of the SNR for the LIF data points presented in this paper is given in Figure 29.

The natural broadening of the line is on the order of 0.08 GHz[53] and the collisional broadening is on the order of 0.05 GHz[45]. The dominant contributions to the line width are the contribution due to Zeeman splitting, given in Table 1, and the

Doppler broadening which is given by $\Delta\nu = \nu_0\sqrt{\frac{8kT_i\ln(2)}{mc^2}}$[53], which is found to be on the order of 3.5 GHz for the ion temperatures in these experiments ($T_i = 0.4$ eV).

For interpretation of the LIF results a Maxwellian IVDF is assumed. Since the natural and collisional broadening is negligible compared to the Doppler and Zeeman broadening only the latter two are considered for the fitting model. The relative magnitudes and the Zeeman splitting of the lines can be calculated from quantum mechanical considerations. These calculations are given in detail in a WVU internal report [55], and are reproduced here in Table 1. The breadth due to the Doppler broadening is approximately 3.5 GHz and the spreading due to the Zeeman splitting is approximately 1 GHz per kgauss. Since the Zeeman splitting and Doppler broadening are of the same order each individual Zeeman split transition needs to be fit with a Doppler broadened Maxwellian function. The fitting function in its most general form is:

$$I(\nu) = \sum_n I_n \exp(\kappa_\nu \frac{(\nu - \delta\nu - \nu_n)^2}{T_i}) \qquad 11$$

For the sigma transitions this gives the fitting function as the sum of six Maxwellian functions of different weights. The ν_n terms represent the shift due to Zeeman splitting and can be calculated for a given magnetic field (calculated shift given in Table 1). The $\delta\nu$ term represents the Doppler shift of the IVDF due to the mean velocity parallel to the magnetic field and is a fitted parameter. The variable κ_ν is a constant with the value 0.092495 (eV/GHz^2)[55]. The relative amplitude of each transition is known and is given by I_n, with values given in Table 1. The parameters $\delta\nu$ and T_i are then adjusted to give a best fit of $I(\nu)$ to the measured spectrum.

5.2 Results:

Figure 30 shows an example of the raw LIF data with the fit from equation 11 that is used to determine the Ar-II parallel velocity. Similar results were obtained across a variety of magnetic fields and were compared to Mach probe measurements. The results of the Mach probe (MP) analysis indicate that the ion velocity parallel to the magnetic field at the plasma center increases monotonically as the magnetic field increases. The Mach number measured was converted to velocity using measurements of electron temperature published previously [45] and is shown in Figure 31. At 400 gauss the analysis shows a Mach number of 0.1 (350 m/s) and at the highest magnetic field the Mach number is approximately 0.8 (2800 m/s). The error bars used represent the standard deviation of multiple measurements as well as an uncertainty in the acceptance angle of ~13°.

The LIF measurements show that the plasma velocity at r=0 remains constant at about 300 m/s from 400 to 1600 gauss, which corresponds to a Mach number of ~0.1. This result stands in stark contrast to the measurements made with the Mach probe, as can be seen in Figure 31, and indicates that the Mach probe interpretation model is not correct.

5.3 Discussion:

The theory underlying LIF interpretation is simple; it relies only on knowledge of the electronic transitions of the ion (or atom) and the Doppler shift. However, the methods of Mach probe interpretation have been disputed and often rely heavily on the plasma parameters[49]. The LIF diagnostic is precise; however, operating the laser and accurately monitoring the wavelength provide some difficulty. In these experiments we are confident of our wavemeter accuracy (wavelength uncertainties represent ±45 m/s), and, as discussed in the appendix, measurement of a fiducial iodine spectrum provides further confirmation that we are returning accurate measurements of the Doppler shifted Ar-II ion velocity distribution function (IVDF). So, the most reasonable conclusion is that LIF has given an accurate measurement of the parallel ion velocity. It then follows that the velocity inferred from the Mach probe data becomes progressively more incorrect as the magnetic field is increased.

This leaves an open question: what is the cause of the discrepancy between the velocity interpreted from the Mach probe and the absolute velocity determined from LIF? We propose that the discrepancy between the LIF velocity measurements and the Mach probe measurements is due to the combination of two effects: the probe shaft leaving a low density geometric shadow on the downstream side, and ion-neutral collisions shortening the presheath length to the order of the ion-neutral mean free path. The remainder of this paper is devoted to deriving an estimate of the magnitude of the probe geometric shadow effect and comparing this theoretical calculation to the experimental data.

5.3.1 Presheath Edge Density Correction

Many Mach probe studies[9,49,56–61] have assumed the presheath length is the "natural" presheath length, $L_n = \frac{w^2 c_s}{D_\perp}$, where w is the probe diameter, c_s is the sound speed, and $D_\perp$ is the perpendicular diffusion coefficient. This is a valid assumption for the presheath length in a fully ionized plasma with Maxwellian electrons. However, when the ion-neutral mean free path is shorter than L_n, $\lambda_{i-n} < L_n$, then the presheath length is proportional to the ion-neutral collision mean free path[62]. As a result, when neutral atoms are present in the plasma the actual length of the presheath can be shorter than the "natural" length.

Another relevant scale length is the probe geometric shadow length, $L_g = \frac{(w^2 v_d)}{D_\perp}$, where v_d is the drift velocity of the background plasma ions. This is the length scale of a depleted density region due to the probe acting as a physical obstruction in the plasma. If the plasma presheath length is shorter than the probe geometric shadow length due to ion-neutral collisions, then as shown in the schematic in Figure 32 the ion saturation current collected would represent the lower, perturbed density of the geometric shadow due to the probe shaft at the position of the downstream presheath edge, instead of the density of the unperturbed plasma. The lower ion saturation current on the downstream side would then appear as an artificially high Mach number when naively applying the Shikama method described by equation 10.

This effect can be demonstrated using a simplified model for the downstream plasma density. The ions are modeled as a fluid, neglecting electrostatic effects. We consider a plasma in slab geometry with transport in the direction parallel to the magnetic field dominated by advection and perpendicular transport dominated by diffusion as described by equation 12, where v_d is the plasma drift velocity parallel to the magnetic field, $D_\perp$ is the cross field diffusion, z is the coordinate parallel to the magnetic field, and y is the coordinate perpendicular to the field.

$$v_d \partial_z n + D_\perp \partial_y^2 n = 0 \qquad 12$$

The probe geometric shadow creates a low plasma density region downstream of the probe as shown in the schematic in Figure 32. As the magnetic field increases, the perpendicular diffusive transport decreases, which increases the geometric shadow length. The effect of the density reduction can be included in the Shikama analysis method as a correction term, shown below.

In order to calculate the correction term, it is necessary to know the magnitude of the downstream density at the presheath edge relative to the unperturbed upstream density. Assuming v_d is constant equation 12 can be rearranged as:

$$\partial_z n + \frac{D_\perp}{v_d} \partial_y^2 n = 0 \qquad 13$$

Equation 13 is analogous to the 1-D diffusion equation, $\partial_t n + \frac{D_\perp}{v_d} \partial_y^2 n = 0$. For the system under consideration here, the probe is modeled as a boundary condition with $n(y, z = 0) = \begin{cases} n_0, & y \geq a \\ 0, -a < y < a, \\ n_0, & y \leq -a \end{cases}$ yielding an analytical solution for the density of the plasma downstream (equation 13):

$$n_d(y,z) = n_0\left(1 - \left(\frac{erf\left((y+a)\sqrt{\frac{v_d}{4D_\perp z}}\right) - erf\left((y-a)\sqrt{\frac{v_d}{4D_\perp z}}\right)}{2}\right)\right) \qquad 14$$

In both equations 13 and 14, $D_\perp$ represents the perpendicular diffusion direction, v_d is the drift velocity, a is the probe radius, w is the probe diameter, and n_0 represents the unperturbed plasma density. The resulting density distribution (n_d/n_0) in the probe wake calculated from equation 14 is plotted in Figure 33 for 400 and 1600 gauss magnetic fields, clearly showing the geometric shadow lengthening as the magnetic field is increased.

This representation of the probe geometric shadow downstream can be used to calculate a correction term for the parallel Mach number using the Shikama method. As shown in equation 15 (taken from reference 46), implicit in the Shikama method is the assumption that the density at the edge of the presheath (y=0, z= L_p) is the same on both the upstream and downstream sides of the probe.

Defining $F_{flow}(M_{||}, \theta)$ as the function $F_{flow}(M_{||}, \theta) = \exp(-\frac{k}{2}\frac{\sin\alpha}{\alpha}(M_{||}\cos\theta + M_\perp \sin\theta))$ with $M_{||}$ used to represent the true Mach number of the flow, while $M_{||,j}$ represents the uncorrected Mach number inferred from the ratio of the upstream and downstream ion saturation currents.

$$\frac{j_{up}}{j_{down}} = \frac{j(M_{||},\pi)}{j(M_{||},0)} = \frac{F_{flow}(M_{||},0+\pi)}{F_{flow}(M_{||},0)} = \frac{F_{flow(up)}}{F_{flow(down)}} \qquad 15$$

This can be easily solved for $M_{||,j}$ as, $M_{||,j} = \frac{\alpha}{\mathrm{k}\sin\alpha}\ln\left(\frac{j_{up}}{j_{down}}\right) = \frac{\alpha}{\mathrm{k}\sin\alpha}\ln\left(\frac{F_{flow(up)}}{F_{flow(down)}}\right)$. However, the probe will affect the downstream plasma density as shown in the model above (equation 14). Since the densities evaluated at the upstream and downstream presheath edges, n_{up} and n_{down}, are not equal, they should be included explicitly in the model. We can do this by converting the ratio $\frac{j_{up}}{j_{down}}$ to include a non-unity value of $\frac{n_{up}}{n_{down}}$.

$$\frac{j_{up}}{j_{down}} = \left(\frac{n_{up}}{n_{down}}\right)\left(\frac{F_{flow(up)}}{F_{flow(down)}}\right) \qquad 16$$

Taking the natural logarithm of equation 16 allows us to relate this back to the model shown in equation 15:

$$\begin{gathered}\ln\left(\frac{j_{up}}{j_{down}}\right) = \ln\left(\frac{n_{up}}{n_{down}}\right) + \ln\left(\frac{F_{flow(up)}}{F_{flow(down)}}\right) \\ \Rightarrow M_{||,\mathrm{j}} = M_{||} + \frac{\alpha}{\mathrm{k}\sin\alpha}\ln\left(\frac{n_{up}}{n_{down}}\right) \\ \Rightarrow M_{||} = M_{||,\mathrm{j}} - \frac{\alpha}{\mathrm{k}\sin\alpha}\ln\left(\frac{n_{up}}{n_{down}}\right) = M_{||,\mathrm{j}} + M_{\mathrm{corr}}\end{gathered} \qquad 17$$

Upstream of the probe there is no shadowing, so the upstream density can be assumed to be the unperturbed density n_0. The density at the edge of the downstream presheath edge, n_{down}, is calculated with the simplified advection-diffusion model described by equation 14. Assuming the probe collects the ion saturation current from the downstream presheath region of length L_{ps} downstream from the probe, the analytic solution for the density collected downstream at the midplane of the probe at position (y = 0, z = L_{ps}) is given by:

$$n_d = n_0(1 - erf(\sqrt{(\frac{a^2 v_d}{4D_\perp L_{ps}})})) \qquad 18$$

The results for the density on axis are shown in Figure 34. This plot shows that as the magnetic field increases the downstream density is reduced for a considerable distance downstream from the probe. The correction for the Mach number accounting for this effect is given in equation 19 and arises from using the expression for the downstream density, equation 18, in equation 17:

$$M_{corr} = \frac{\alpha}{\mathrm{k}\sin\alpha}\ln(1 - erf(\sqrt{\frac{a^2 v_d}{4D_\perp L_{ps}}})) \qquad 19$$

All Mach probe measurements were made at the center of the plasma column, r = 0, where the density fluctuations and turbulent particle flux due to drift waves are at a minimum[63]. Hence the perpendicular diffusion can be treated as classical on axis. The classical diffusion constant is given by, $D_\perp = \frac{D_{\perp,A}}{1+\left(\frac{\omega_{ci}}{\nu_i}\right)^2+\frac{\mu_i}{\mu_e}\left(1+\left(\frac{\omega_{ce}}{\nu_e}\right)^2\right)}$. Here $\omega_{c\beta}$ is the cyclotron frequency of the βth species, ν_β is the total collision frequency of the βth species, and μ_β is the mobility of the βth species. The perpendicular diffusion coefficient is given by: $D_{\perp,A} = \frac{V_{Ti}^2}{\nu_i}(1+\frac{T_e}{T_i})$, where $\nu_i = \nu_{i-e} + \nu_{i-n}$. The electron collision frequency, ν_e, is dominated by the electron-ion momentum exchange frequency.

The collision frequencies for the ions were calculated using the formulas from Choi[64]. The neutral densities were calculated based on the measured neutral pressure at the wall of the device, which was consistently about 1.1 mTorr. Assuming that the neutral temperature is the same as the plasma ion temperature at r = 0 and the neutral pressure is constant across the radius of the chamber, the neutral density is easily modeled as $n_{r=0} = \frac{P_{wall}}{T_{r=0}}$. A calculation of the resulting ion-neutral collision frequency is given in Table 2. The dominant contribution to the perpendicular diffusion coefficient was found to be from the electron-ion momentum exchange frequency.

It is important to note that the parallel plasma diffusion is neglected in this model. This is appropriate when the parallel probe shadow Péclet number, $Pe = \frac{L_g v_d}{D_{||}}$ > 1. Here the parallel diffusion coefficient is calculated using the Einstein relation, $D_{||} = \frac{V_{Ti}^2}{\nu_s}$, where ν_s is the ion-ion momentum exchange frequency. A calculation of the parallel probe shadow Péclet number is shown in Table 3. These calculations indicate that the agreement is expected to be poorest under the 400 gauss conditions, as the Péclet number drops below 1, and we expect the model to break down at magnetic fields at or below 400 gauss in our device.

Corrected Mach probe data are shown in Figure 35. The presheath length used is approximately the ion-neutral mean free path calculated using $\frac{c}{\nu_{i-n}}$ as described in [62].

The drift velocity used is the velocity measured with LIF, the perpendicular diffusion is calculated as the classical perpendicular diffusion coefficient using the ion temperature measurements from the LIF experiments.

The corrected Mach probe data shows excellent agreement with the measurements from the LIF experiment, with the exception of the data point at 400 gauss. The analytic model for the probe shadow is expected to break down at this field because the parallel diffusion can no longer be neglected. We consider this to be a strong indication that this enhancement of the Mach number is due to the geometric shadow described in this section.

5.4 Summary and Conclusions:

In this paper we compared measurements of the velocity parallel to the magnetic field taken with Mach probe and LIF techniques. As can be seen in Figure 31, the LIF technique shows a parallel velocity approximately constant at 300 m/s over the range of magnetic fields used in these experiments, while the Mach probe reports a velocity ranging from 350 to 2800 m/s over the same range of magnetic fields. The velocity reported by the Mach probe increases monotonically with increasing magnetic field, suggesting that the cause of the discrepancy is proportional to the magnetic field.

We have shown that the presence of the probe creates a shadow downstream by absorbing the plasma as it passes, a simple 2-D model of the shadow is presented in Figure 33. In a collisionless plasma this shadow would be shorter than the presheath length for subsonic flows, and thus this effect would not apply in that case. However, previous studies have shown that the presheath length in collisional plasmas is proportional to the ion-neutral mean free path. If the ion-neutral mean free path is shorter than the length of the probe geometric shadow the downstream ion saturation current will be reduced due to the shadow as shown in the schematic in Figure 32.

We present a simple correction term taking into account the probe shadow in equation 19 and demonstrate that it can correct for the reduced downstream density due to shadowing as shown in Figure 35. It is well known that the ion-neutral collisions can affect the presheath length, and we have shown the perturbation due to the probe shadow can dominate the ion saturation current signal. If the plasma parameters are well known (C_s, T_e, $D_\perp$) the magnitude of this shadow effect can be calculated and accounted for.

For practical purposes, the model for the downstream density should be used by groups using Mach probes to ensure that the effects due to the geometric shadowing of the probe are included whenever the geometric shadow length, $L_g = \frac{a^2 V_d}{D_\perp}$, is on the order of the ion-neutral mean free path. This could be especially important in regions of a tokamak where the neutral gas pressure is relatively high, such as the divertor. When exact measurements of the ion-neutral mean free path and perpendicular diffusion are not available the probe shaft should be designed so that the radius is less than a critical radius derived from equation 19, $a_{crit} = \sqrt{(\frac{4.*D_\perp*\lambda_{i-n}}{c_s})}$, to avoid these probe shadowing effects.

Portions of Chapter 5 have been submitted for publication of the material as it may appear in Physics of Plasmas, 2016, J. J. Gosselin, S. C. Thakur, S. H. Sears, J. S.

McKee, E. E. Scime, and G. R. Tynan, American Institute of Physics, 2016. The dissertation author was the primary investigator and author of this paper.

Table 1 In the left column are line shifts due to Zeeman splitting of the sigma, m = 1 transition from the central line location. Right column contains the relative amplitude of the line components. Total amplitude is normalized to 1.

Line Shift (GHz/kGauss)	**Weight**
$\nu_0 = 1.26$	$I_0 = 0.375$
$\nu_1 = 1.44$	$I_1 = 0.268$
$\nu_2 = 1.63$	$I_2 = 0.179$
$\nu_3 = 1.82$	$I_3 = 0.107$
$\nu_4 = 2.01$	$I_4 = 0.0536$
$\nu_5 = 2.19$	$I_5 = 0.0178$

Table 2 Values of the various collision frequencies used to calculate the perpendicular diffusion coefficient.

Collision Frequencies Used for Perpendicular Diffusion	
Collision Type	Collision Frequency (kHz)
Ion-neutral Charge Exchange	11
Ion-electron Momentum Exchange	0.5
Electron Impact Ionization	1.7
Electron-ion Momentum Exchange	64,000

Table 3 Scaling parameters of the probe shadow. Parallel and perpendicular diffusion coefficients calculate from classical considerations as discussed in the text.

Magnetic Field (gauss)	Parallel Diffusion, $D_{\|\|}$ (cm^2/s)	Perpendicular Diffusion, $D_\perp$ (cm^2/s)	Probe Shadow Scale Length (cm) $Lg = w^2 Vd/D_\perp$	Probe Shadow Parallel Peclet Number $Pe = L_g V_d / D_{\|\|}$
400	34000	9400	0.64	0.56
800	51000	2500	2.4	1.4
1200	64000	1100	5.4	2.5
1600	43000	800	7.5	5.2

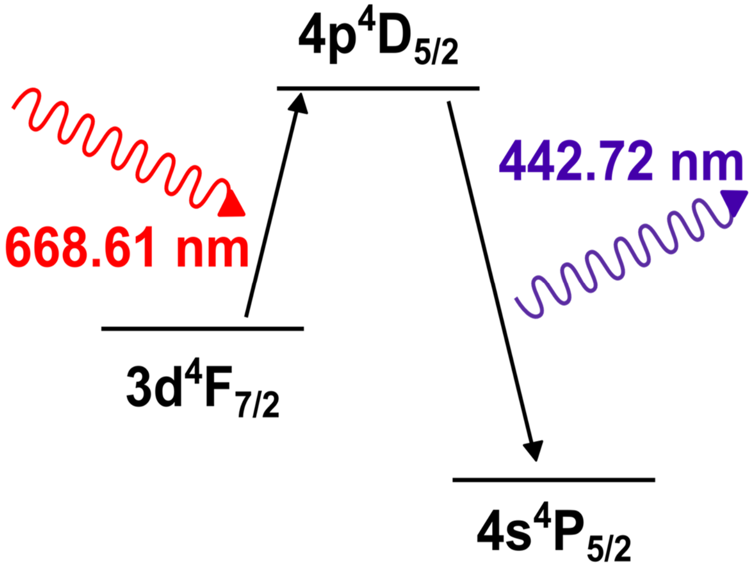

Figure 25 Diagram showing the three-level scheme for LIF. Red laser light excites the metastable transition at approximately 668.61 nm, and the ion re-emits at 442.72 nm.

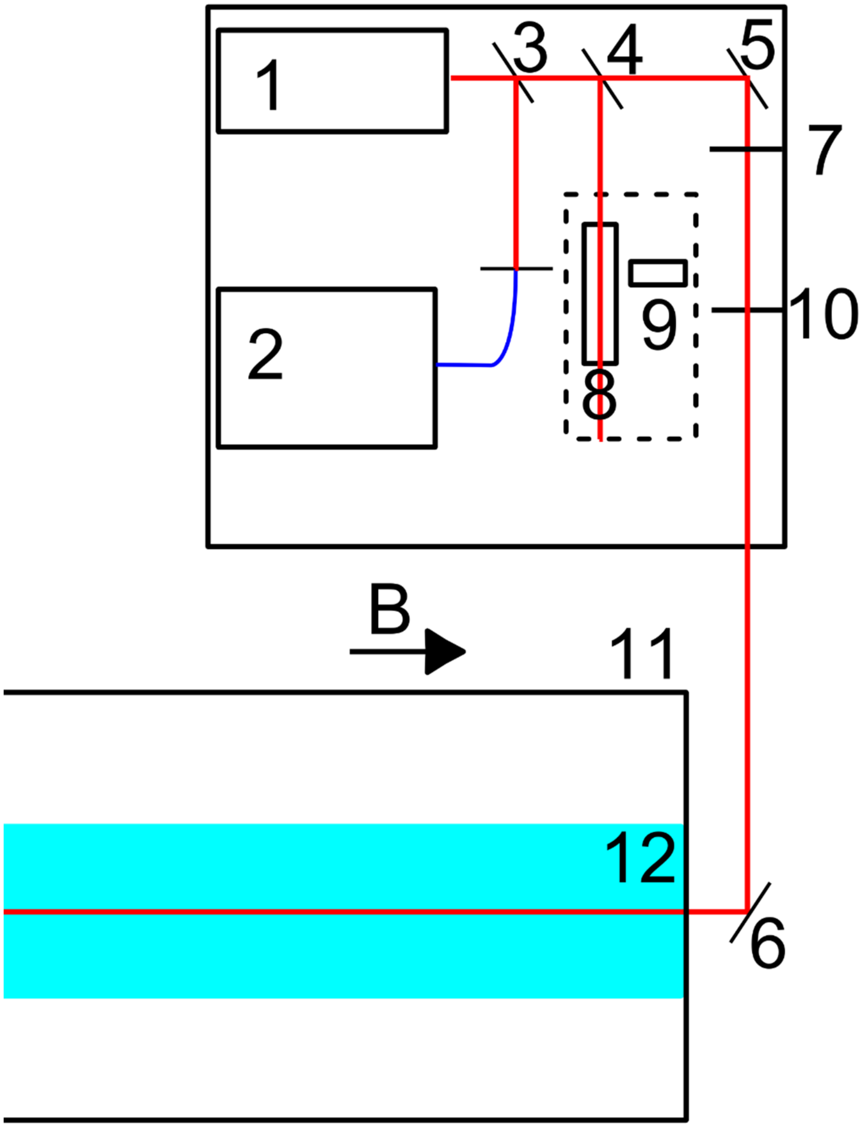

Figure 26 Schematic of LIF setup. Shown in red is the laser beam path; The laser travels through a window at the end of the plasma device and along the axis of the machine. Shown in the dotted line is the iodine cell enclosure. Shown in blue is a fiber optic cable. Also shown is: 1) Toptica T100 laser, 2) Bristol Instruments 621-VIS wavemeter, 3) 8% beam splitter, redirecting 8% of the beam energy to the wavemeter, 4) 8% beamsplitter redirecting 8% of the beam energy through the iodine cell, 5-6) turning mirror, 7) quarter wave plate 8) iodine cell, 9) PMT for monitoring iodine florescence, 10) chopper wheel, which modulates the beam at ~1 kHz, 11) CSDX vacuum chamber, 12) plasma column

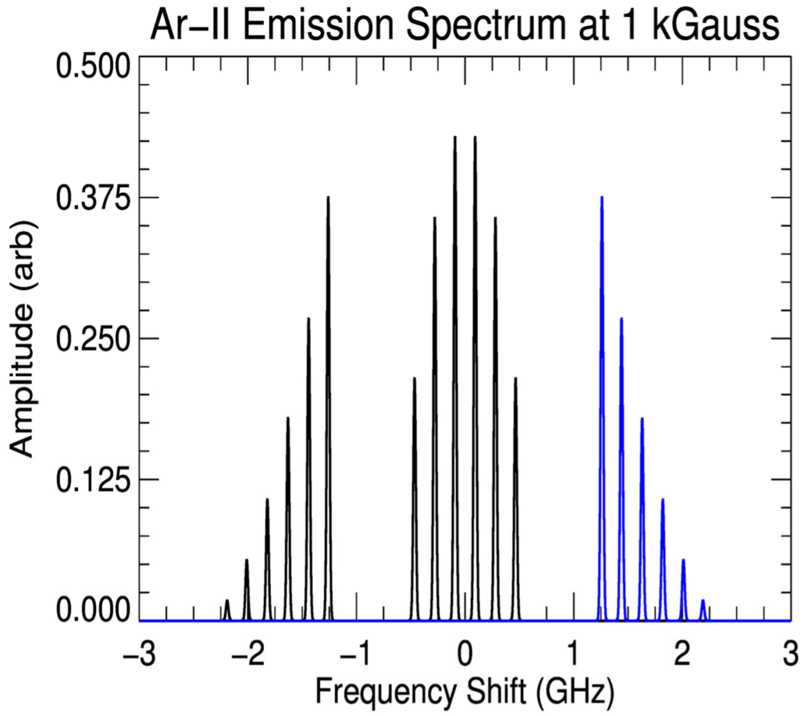

Figure 27 Diagram showing the emission spectrum used by the three level LIF scheme. Zeeman splitting is illustrated for the 1 kGauss case. Line widths are arbitrary. The sigma transition branch used for the LIF measurements is shown in blue.

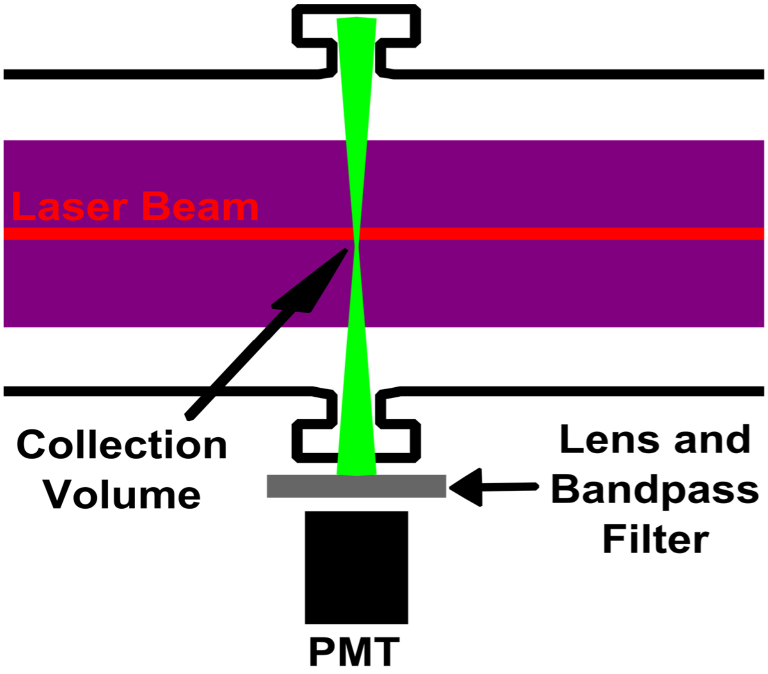

Figure 28 Diagram of CSDX showing the LIF laser beam (red online) and the PMT viewing area (green online). The overlap of the beam and PMT view gives the effective collection volume, which determines the spatial resolution of the experiment.

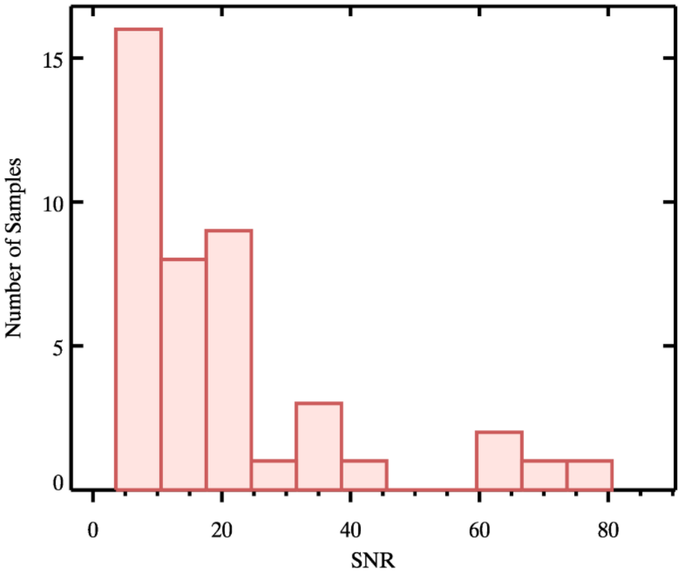

Figure 29 Histogram of the signal to noise ratio for the LIF data shown in this paper. As can be seen, most of the data points have a signal to noise ratio between 3.5 and 25.

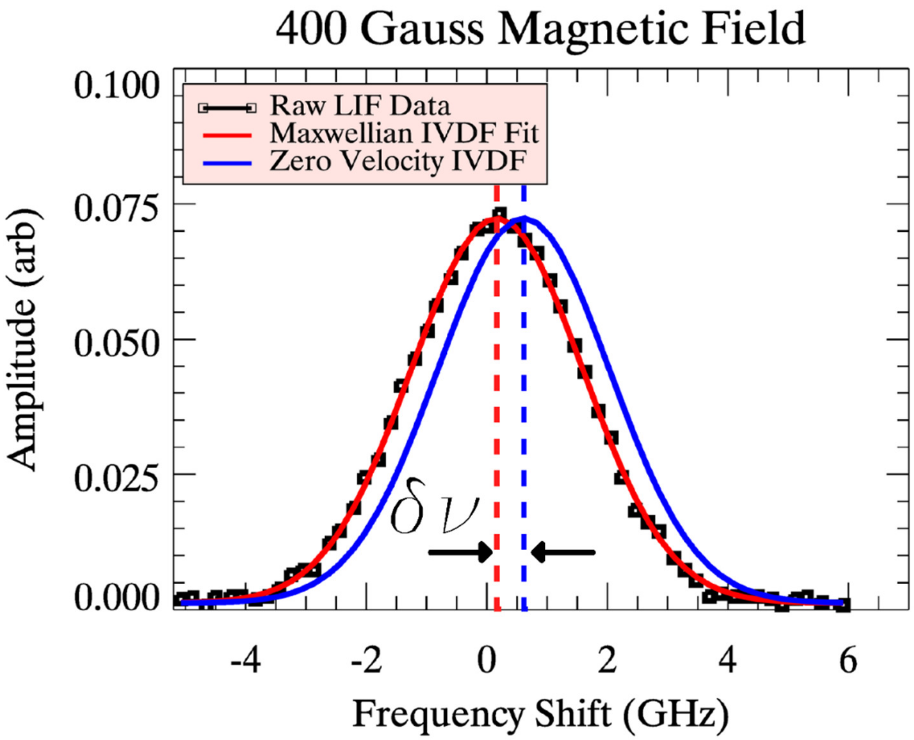

Figure 30 Plot showing the LIF raw data with the fit used to extract the velocity. Temperature is determined from the width, and the mean velocity is determined by the shift of the function relative to the expected Zeeman shift. Here the shift is 0.44 GHz, which corresponds to 300 m/s of ion flow. The unshifted distribution is determined by the wavemeter measurements (confirmed with the fiducial iodine spectrum) and the calculated Zeeman shifts from Table 1

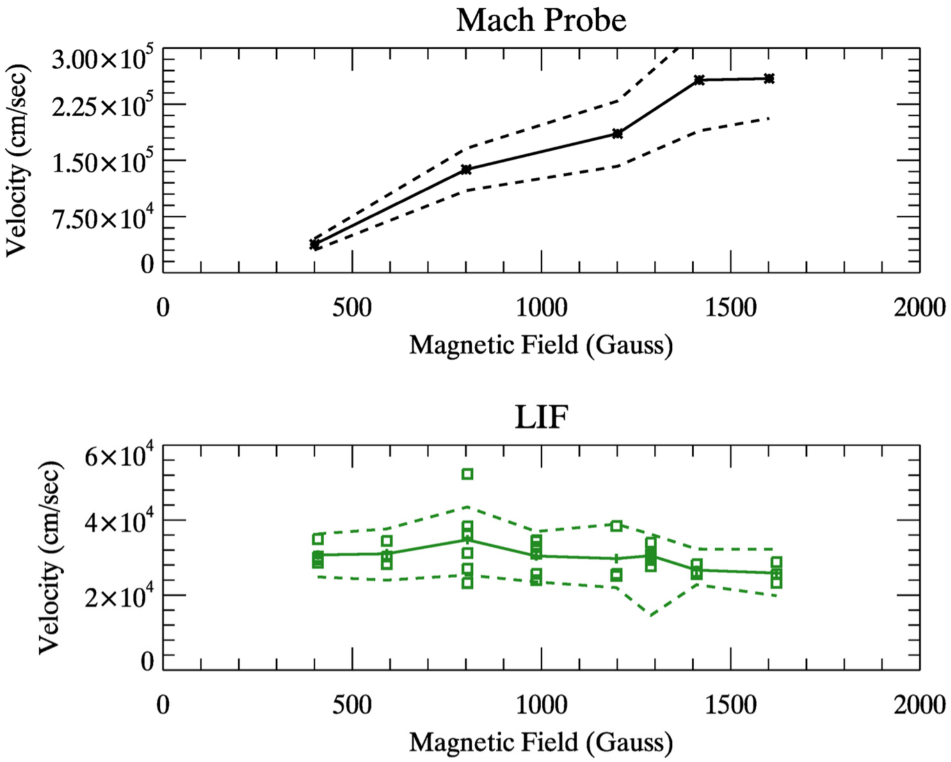

Mach Probe

LIF

Figure 31 Plot showing the plasma ion velocity as determined by the Mach probe (top) on the plasma axis (r=0) for comparison with the velocity on axis determined by LIF (bottom) on the plasma axis. It can be clearly seen that there is a disagreement between the two values at fields higher than 400 gauss, and that the disagreement increases with increasing magnetic fields.

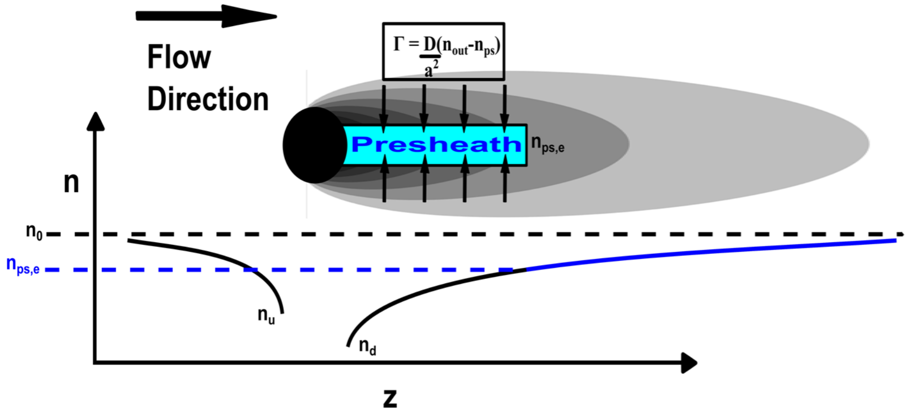

Figure 32 Schematic of the probe shadow and the boundary conditions for the presheath model. The black circle represents the Mach probe, the grey region downstream of the probe represent the low density geometric shadow with darker grey representing lower density. Cartoon plot below illustrates the presheath density drop in black. In blue is the density drop due to the probe shadow, which demonstrates the reduced density at the presheath edge, $n_{ps,e}$.

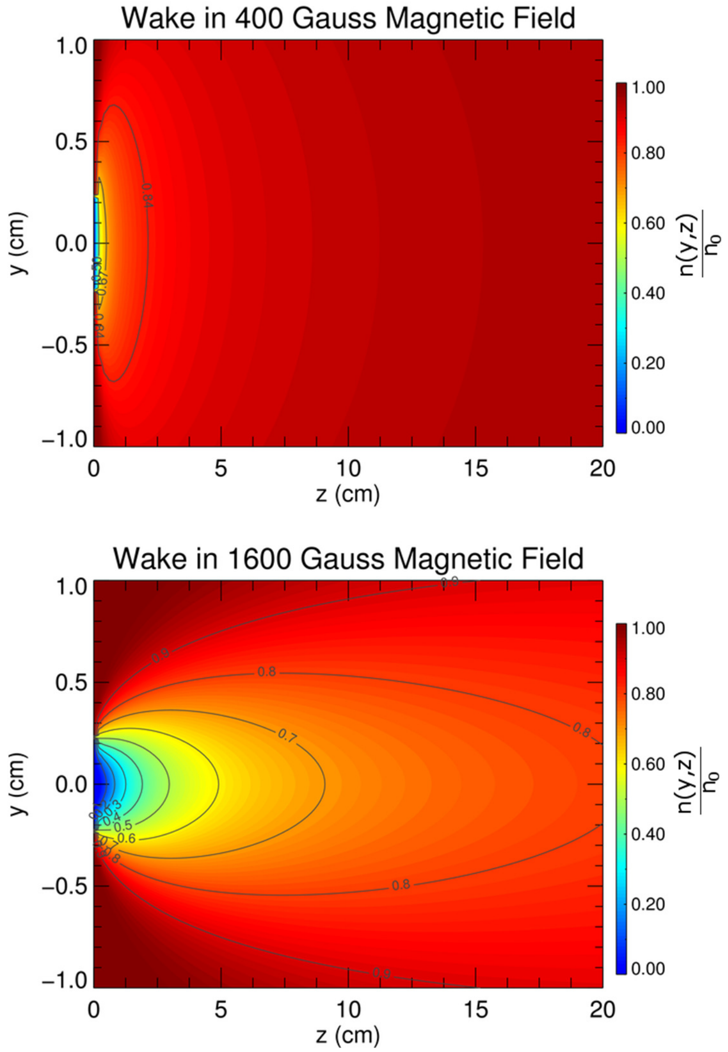

Figure 33 Low density wake calculated from simplified model at 400 and 1600 gauss magnetic fields. Contours represent $\frac{n(y,z)}{n_{up}}$. Wake elongation due to decreased perpendicular transport can be seen clearly by comparing the two plots.

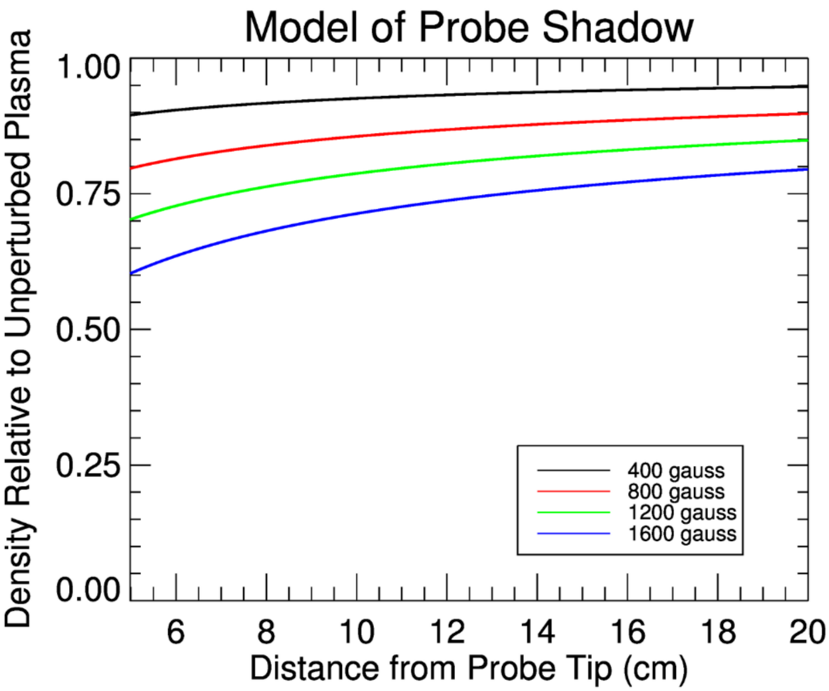

Figure 34 Background plasma density due to the geometric shadowing with different magnetic fields. The edge of the plot (at 23 cm) represents the presheath edge. The density at distances less than 23 cm from the probe tip is determined by the presheath physics.

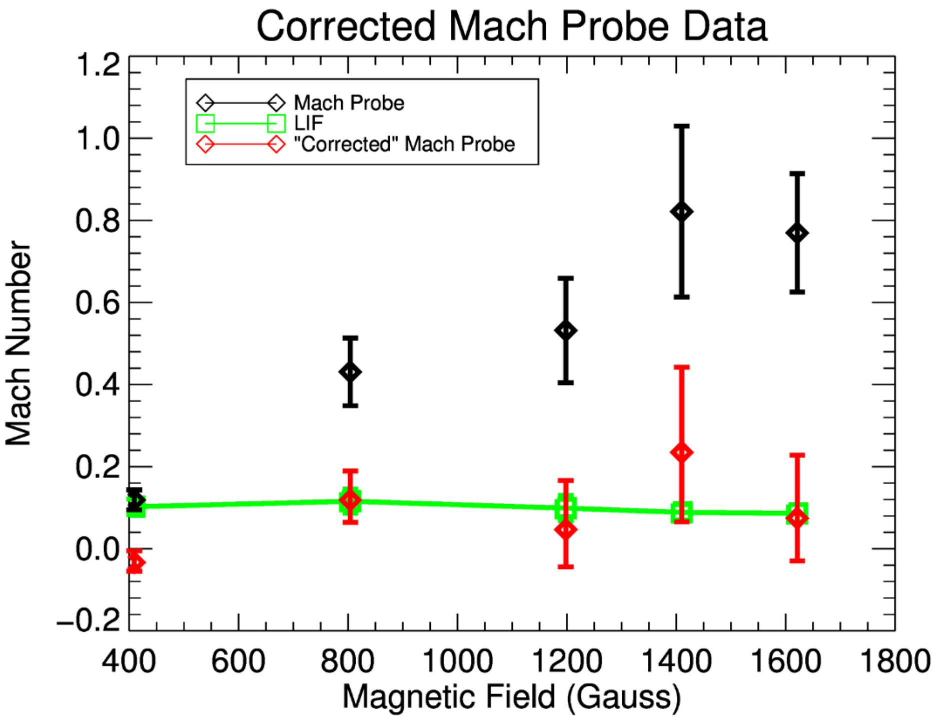

Figure 35 Plot showing the application of the collisional presheath correction for 0-D model (red online). These are compared to the actual velocity (determined from LIF, green online), and the Mach number from the Mach probe interpretation (shown in black). With the exception of the MP measurement at 400 gauss (where the simplified probe shadow model is expected to break down) the correction term works very well, suggesting that the geometric shadow is playing a roll.

Chapter 6: Multi-Species Ambipolar Diffusion Along a Magnetic Field

6.1 Introduction:

Understanding the migration of wall material in a fusion device is essential to understanding the lifetime of the plasma-facing components (PFCs)[65]. Material migration will occur in long pulse and steady state confinement devices due to the combined action of material erosion due to physical sputtering and chemical erosion, ionization of some or all of the eroded material, entrainment on the material in the background plasma, and, finally, redeposition of that material elsewhere in the system.

In this paper we investigate the parallel diffusion of a heavy impurity that is injected into a background of lighter ion, flowing plasma. This seemingly simple parallel transport mechanism can be complex. For example, work in ionospheric plasmas has shown that the ambipolar diffusion of impurities in a plasma is non-linear in terms of the ratio of impurity to plasma ion density[66,67] . In this paper we present measurements of the parallel diffusion of a low density, non-perturbative burst of impurities that are injected into an argon plasma flowing parallel to the magnetic field.

The paper is organized as follows. In the first section we discuss the experimental apparatus used for the measurements of the parallel transport. In the results section we describe the measurements, and show that it can be described by a simple advection-diffusion model by examining the impurity plume. Finally, we discuss the theory of multispecies ambipolar diffusion and show that our measurements are consistent with non-neutral, current-free ambipolar distribution of the heavier impurities in the background lighter ion plasma.

6.2 Experimental Methods:

These experiments were performed in the CSDX linear plasma device (Figure 15), a 2.8m long, 0.1 m radius helicon plasma device. Argon is used as the working gas and is injected at the first available port downstream of the source. The gas is ionized using an M = 1, helical antenna with a radius of 7.5 cm operating at 13.56 MHz and 1.8 kWatts of RF power. The plasma is confined radially by a series of 28 coils which provide a solenoidal magnetic field in the range of 0-2400 gauss, and the plasma is free to flow axially along the length of the machine until it recombines at the ends.

Diagnostic access is provided by way of a series of ports located 70cm apart along the length of the machine as well as a large window at the downstream (pump) end of the device. For the purposes of these experiments these ports were equipped with windows for optical access to the plasma.

A laser blow off (LBO) impurity injection scheme was used to introduce a plume of impurities and to study the transport properties of the impurities in the plasma. In order to utilize this technique a microscope slide is coated with a thin (~2-3 micron) layer of the desired solid impurity. The coated slide is placed inside the vacuum chamber attached to a linear positioner. A focused laser pulse propagates through the slide and deposits energy into the thin film.

The energy absorbed from the laser ablates the thin film in a region under the laser spot. The film is blown off as a combination of impurities, ions, and dust grains. The ions are deflected by the magnetic field. The neutral particles travel into the plasma where they are ionized by electron collisions. The resulting ions are confined radially by the magnetic fields and transported axially by frictional drag with the background plasma. A diagram of the cross section of the slide mount and vacuum hardware for the LBO system is shown in Figure 21 in Chapter 3.

A non-perturbative source of impurities was ensured by a series of probe measurements of the ion saturation current in the plasma as the impurity cloud passed the ion saturation current collecting probe tip. The laser power and spot size was adjusted to control the amount of impurities ablated off of the slide. In the experiments presented here the perturbation to the ion saturation current was within the ion saturation current fluctuations that are inherent to the background plasma operating conditions[45]. The perturbation in the ion current due to the impurity injection was found to be less than 5% at 400 gauss.

Typical spot sizes of ablated film were about 0.5-1 mm. Typical energy of the laser pulse was between 25 and 50 mJoules for each shot. A back of the envelope calculation can be carried out using the heat of vaporization (151 kJoules/mol), the heat of fusion (11 kJoules/mol), the specific heat (25.5 Joules/(mol K)), and the volume of the ablated spot[1]. The range of energies required for ablation range from 6 mJoules at the smallest spot size and thickness to 22 mJoules at the largest spot size and thickness.

A photomultiplier tube equipped with a 10 nm bandpass filter centered over the 6p7s(1/2,1/2) -> 6p7p(1/2,3/2) transition at 521 nm in Bi-II (ionized bismuth) was placed at the injection location and the next two ports downstream of the injection site. The 6p7s(1/2,1/2) -> 6p7p(1/2,3/2) transition was chosen because it is sufficiently bright and spectrally isolated from both the Ar-I and Ar-II lines in the plasma. This ensures that the light pollution from the background plasma is kept to a minimum.

A 2-dimensional, cross-sectional view of the impurity cloud immediately after injection was obtained using a fast camera equipped with a 520 nm centered, 10 nm width bandpass filter. This view is shown in Figure 22 in Chapter 4. The light emission profile is proportional to the product of the bismuth impurity ion density and the electron density. The light emission occurs primarily from the region located inside a radius of $r \leq 2$ cm. Thus, even though the photo multiplier tubes integrate across the entire diameter of the plasma, only the first centimeter or two of plasma radius needs to be considered. This is beneficial for our parallel transport measurements because we may neglect parallel velocity shear and to use a 1-D advection diffusion model, satisfying $v\frac{\partial n}{\partial z} + D_{||}\frac{\partial^2 n}{\partial z^2} = 0$, for the impurity transport.

Figure 36 shows a profile of the parallel velocity at 400 gauss. It has been shown previously[68] that the ion-neutral collisions need to be taken into account under certain parameter regimes. The data shown in Figure 36 agrees with LIF data on the plasma axis (r=0). This indicates that the correction term used in chapter 5 is not necessary in this plasma parameter regime. So the full profile of parallel velocity is used to estimate the effect of the plasma shear.

Since the electron temperature profile is relatively flat across the bulk of the plasma column[45], the ion saturation current, shown in Figure 37, can be taken to be proportional to the plasma density and is fit well by a Gaussian with a standard width, σ, of 3 cm.

The full 2-dimensional advection-diffusion equation is not analytically tractable. However, the effect of radial shear of the parallel velocity $\left(\frac{\partial V_z}{\partial r}\right)$ alone can be estimated by applying an analysis similar to that used by G. I. Taylor[69].

In this analysis we calculate the effect of the radial shear of the parallel velocity while neglecting diffusion. A bismuth density profile is assumed that is constant in radius and Gaussian in the axial direction. The electron density is measured as Gaussian in the radial direction and assumed constant in the axial direction. The velocity profile is approximated by a quadratic, $V(r) = V_0\left(1 - \left(\frac{r}{a}\right)^2\right)$, where a = 7cm and V_0 = 3600 cm/s. This disagrees with the measured velocity at r>7cm, but the electron density in this region is very low. So, it is expected to contribute negligibly to the light emission of the impurity cloud.

The total intensity of light emitted by the impurity cloud should be proportional to the product of the electron density and the impurity density.

$$I_{Bi}(r,z,t) \propto n_e(r) n_{Bi}(r,z,t) \qquad 20$$

$$\propto \exp\left(-\frac{(z-vt)^2}{2\sigma_{Bi}^2}\right)\exp\left(-\frac{r^2}{2\sigma_e^2}\right)$$

Here, n_e is the electron density, n_{Bi}, is the bismuth density, and σ_{Bi} is the standard width of the bismuth distribution in the axial direction, and σ_e is the standard width of the electron distribution in the radial direction.

The signal captured by the PMTs will be proportional to the total light emission throughout the plasma column. Integrating the light emission across the radius at a constant axial position yields:

$$I_{tot,Bi} = \alpha\ (\exp\left(\left(\frac{z-V_0 t}{2\sqrt{2}\,\sigma_{Bi}} + \frac{\sigma_{Bi}a^2}{\sqrt{2}\,V_0 t\,\sigma_e^2}\right)^2 \right. \qquad 21$$

$$\left. -\frac{(z-V_0 t)^2}{2\,\sigma_e^2}\right)(\operatorname{erf}\left(\frac{z-V_0 t}{2\sqrt{2}\,\sigma_{Bi}} + \frac{\sigma_{Bi}a^2}{\sqrt{2}\,V_0 t\,\sigma_e^2}\right.$$

$$\left. + \frac{R^2 V_0 t}{\sqrt{2}\sigma_{Bi}a^2}\right) - \operatorname{erf}\left(\frac{z-V_0 t}{2\sqrt{2}\,\sigma_{Bi}} + \frac{\sigma_{Bi}a^2}{\sqrt{2}\,V_0 t\,\sigma_e^2}\right))\ )$$

Here, α is a normalization constant and R is the radius over which the integration is taken (in this case to the wall of the plasma chamber, R = 10cm).

Although the form of equation 21 is complicated, it can be seen graphically in Figure 38 that the expected effect due to the velocity shear in these experiments is small. It results in the appearance of a plume traveling 3% slower than the actual velocity and a 6% increase in the apparent plume width. For the purposes of these experiments that is considered to be negligible.

The solution to the 1-dimensional advection-diffusion equation is well known when a delta function initial condition for the injected impurity is assumed and is given by $C(x,t) = \frac{C_0}{\sqrt{(4\pi Dt)}}\exp(-\frac{(z-vt)^2}{(4Dt)})$. Clearly a delta function initial condition is not a physical initial condition for this system. While this assumption will not affect the parallel velocity measurement because of the symmetric injection at the center of the port, it will lead to an artificially enhanced measurement of the diffusion coefficient. In order to more accurately predict the diffusion coefficient a better estimate of the initial condition for the impurity plume is therefore necessary.

This can be done by assuming that the diffusion coefficient is constant along the length of the device. In this situation the plume can be approximated by an imaginary injection of a delta function-like plume at an earlier time upstream of the actual injection location, $C(z,t) = \frac{C_0}{\sqrt{(4\pi D_0(t-t_0))}}\exp(-\frac{(z-z_0-v(t-t_0))^2}{(4D_0(t-t_0))})$. Here z_0 and t_0 represent an earlier axial location and an earlier time ($z_0 < 0$, $t_0 < 0$) relative to the time and place of the actual injection (at $z = 0$, $t = 0$). The constant diffusion coefficient is represented by D_0.

This then creates a Gaussian shaped plume that has a finite width when it reaches the actual injection location at time $t = 0$, $C(z,t) = \frac{C_0}{\sqrt{(4\pi D_0(-t_0))}}\exp(-\frac{(-z_0-v(-t_0))^2}{(4D_0(-t_0))})$. Since the solutions are in the form of a shifted gaussian the unknown coefficients (D_0, t_0) can be determined uniquely by equating the width of the Gaussian plumes at the two measurement ports downstream of the initial conditions. If $\sigma_{2,3}$ and $t_{2,3}$ represent the inferred diffusion coefficient and arrival time (V/$L_{2,3}$ where V is the inferred velocity and $L_{2,3}$ is the distance from the injection port to port 2 or 3 downstream) from ports 2 and 3 downstream of the injection site (see Figure 15 in Chapter 3), then the equations that determine the unknown quantities are $D_0(t_2 - t_0) = \sigma_2^2$ and $D_0(t_3 - t_0) = \sigma_3^2$. Solving these for the unknown quantities yields $t_0 = -\frac{\sigma_2^2 t_3 - \sigma_3^2 t_2}{\sigma_3^2 - \sigma_2^2}$ and $D_0 = \frac{\sigma_2^2 - \sigma_3^2}{2(t_2 - t_3)}$. A typical example of the photo multiplier tube measurements along with the fitted solution to the 1-D advection diffusion equation are shown in Figure 23 in Chapter 4. It can be seen that the 1-D advection diffusion model agrees well with the data.

Laser induced fluorescence (LIF) was used to measure the temperature of the ions in the plasma. LIF is a technique that utilizes a tunable laser to excite a metastable transition in the targeted ion species. For our experiment we use a three level scheme first described by Severn[53] to excite transitions in the argon ions. The light is reemitted at a wavelength distinct from the excitation wavelength for detection with a photo multiplier tube. By scanning the wavelength of the laser over a small range the entire IVDF can be measured. The laser set up and details of the LIF apparatus are described in detail elsewhere[68] and in chapter 5.

6.3 Results:

Figure 39 shows the Doppler broadened emission from the argon ions in the plasma. The measured ion temperatures for different magnetic fields are given in Table 4. It can be seen that there is a gradual increase in the ion temperature as the magnetic field is increased.

The standard width of the initial plume, $\sigma_0 = \sqrt{(D_0(-t_0))} \;= \frac{(D_3 - D_2)t_2 t_3}{t_2 - t_3}$, is found to be consistent across all the magnetic field measurements with a value of σ = 7.5 cm ± 2 cm. Figure 40 shows the diffusion coefficients as measured assuming a constant value along the length of the device as described above. The classical, collisional, Einstein diffusion coefficient is calculated as $D = \frac{V_{ti}^2}{\nu_{Bi-Ar}}$ where ν_{Bi-Ar} is the bismuth-argon momentum exchange rate and V_{Ti} is the thermal velocity of the bismuth ions. The bismuth ion temperature is assumed to be the same as the argon ion temperature.

It is interesting to note that the diffusion coefficient appears to be purely collisional with no contribution from the ambipolar electric field. The open question for discussion is: how does this compare with theories for multispecies ambipolar diffusion?

6.4 Discussion:

It was seen experimentally that increasing the laser power would increase the amplitude of the impurity cloud emission at the injection site. This is presumably due to an increase in the number of injected bismuth atoms indicating that the laser pulse is marginally energetic enough to ablate the coating. Thus it is presumed that the ablated atoms have a temperature near the vaporization temperature, approximately 0.2 eV[1], and rapidly equilibrate to the background plasma temperature (approximately 5 μsec). However, even at an extreme upper limit for the initial temperature, the energy exchange time is remarkably short compared to the transit time of the impurities from the injection port to the first port downstream.

An extreme upper limit on the initial temperature of the ablated impurities can be calculated by assuming complete absorption of the maximum energy laser pulse used into the smallest diameter spot size in a region of the film with the minimum thickness. This gives an excess laser energy of approximately 45 mJoules deposited in 1.4 x 10^{16} atoms resulting in a temperature for the impurity cloud of 15 eV. Even at this extreme upper limit, the thermal equilibration timescale is only 20 μsec, two orders of magnitude lower than the transit time between the injection port and the port downstream. So, the temperature of the impurities is presumed equal to that of the background plasma ions.

The problem of multispecies ambipolar diffusion was considered theoretically in terms of the ionosphere by Hill[66] in 1978 and again by Bellan[67]. Hill and Bellan were concerned about negative ions and negatively charged aerosols in the ionosphere. However, the equations for the ion fluxes are general. Assuming the ion mobility is negligible compared to the electron mobility, quasineutrality, and zero net current, the equations for parallel flux of the ion species are[66]:

$$\Gamma_\alpha = -D_\alpha \nabla n_\alpha - n_\alpha \frac{Z_\alpha T_e}{T_\alpha} D_\alpha \frac{\sum_{\{\beta \neq e\}} Z_\beta \nabla n_\beta}{\sum_{\{\beta \neq e\}} Z_\beta n_\beta} \qquad 22$$

Here the subscript α refers to the ion species diffusing through a background species β. D_α is the diffusion coefficient determined from the Einstein relation, and Z_β

is the charge state of the β species. The first term is the collisional diffusion, and the second term is the enhanced transport due to the ambipolar electric field.

The second term introduces non-linearity in the ion densities through the summation in the denominator. In our plasmas the impurity injection has been specifically tailored to be nonperturbative. The lack of an impurity induced perturbation in the ion saturation current implies $\frac{n_\beta}{n_\alpha} \ll 1$. The non-linear term can then be approximated by a Taylor expansion to lowest order in $\frac{n_\beta}{n_\alpha}$ for both the background argon plasma and the bismuth impurities.

$$\boldsymbol{\Gamma_{Bi}} = -D_{Bi}\left(1 + \frac{n_{Bi}T_e}{n_{Ar}T_{Bi}}\right)\boldsymbol{\nabla} n_{Bi} - D_{Bi}\frac{n_{Bi}T_e}{n_{Ar}T_{Bi}}\boldsymbol{\nabla} n_{Ar} \tag{23}$$

$$\boldsymbol{\Gamma_{Ar}} = -D_{Ar}\left(1 + \frac{T_e}{T_{Ar}}\right)\boldsymbol{\nabla} n_{Ar} - D_{Ar}\frac{T_e}{T_{Ar}}\boldsymbol{\nabla} n_{Bi} \tag{24}$$

As discussed above, the temperature of the bismuth ions is assumed to be the same as the temperature of the background plasma ions because the energy exchange time of the impurity ions with the background plasma ions is orders of magnitude less than the transit time between the injection site and the first photomultiplier tube downstream. Thus the ion species will have time to thermally equilibrate.

As can be clearly seen from equation 24, the ambipolar terms are zeroth order in the density ratio, $\frac{\mathrm{n}_\beta}{\mathrm{n}_\alpha}$, for the background argon ions. This gives a form for the ambipolar diffusive flux that is precisely what would be expected by comparison with a single ion species plasma. However, the ambipolar contribution to the flux for the bismuth impurities is first order in the smallness parameter, $\frac{n_\beta}{n_\alpha}$. Assuming impurity injection into a uniform background plasma (no axial gradient in the argon plasma) and dropping the terms that are first order in the smallness parameter gives:

$$\boldsymbol{\Gamma_{Bi}} = -D_{Bi}\ \boldsymbol{\nabla} n_{Bi} \tag{25}$$

$$\boldsymbol{\Gamma_{Ar}} = -D_{Ar}\frac{T_e}{T_{Ar}}\boldsymbol{\nabla} n_{Bi} \tag{26}$$

The argon background plasma shifts in response to the ambipolar field induced by the rapidly diffusing electrons from the impurity pulse. Meanwhile the impurity ions will diffuse collisionally according to the diffusion coefficient determined from the Einstein relation $D_{Bi} = V_{TBi}^2/\nu_m$, where V_{TBi} is the thermal velocity of the bismuth ions and ν_m is the momentum exchange rate between the bismuth and background argon ions. The parallel diffusion coefficient for the impurities can then be calculated directly, and this is shown in Figure 40.

6.5 Conclusion:

In this paper we have presented measurements and calculations of multi-species ambipolar diffusion parallel to the magnetic field in the CSDX linear device. We introduced trace amounts of impurities into an argon plasma in a linear plasma device through a laser blow off system, which is shown in Figure 15 in Chapter 3. The impurity transport is modeled using a 1-dimensional advection-diffusion equation. This is appropriate because the impurity ion light emission is primarily coming from the center of the plasma as shown in Figure 22. The data is fit assuming a Gaussian function initial condition for the impurity plume. The fits of the equation and the PMT output from the impurity light emission are shown in Figure 23, and it is easily seen that there is good agreement downstream of the injection site.

In order to accurately measure the parallel diffusion coefficient, it is necessary to constrain the initial condition to a physically realistic scenario. By assuming that the parallel diffusion coefficient is constant along the length of the device we can uniquely determine the width of the initial plume. The calculated parallel diffusion coefficient is shown in Figure 40, and it agrees with the theoretical calculation of the parallel diffusion coefficient within the error bars.

In this paper we measurements of multispecies diffusion in a laboratory plasma. We have observed the surprising result that trace impurities will diffuse collisionally and will not suffer enhanced diffusion due to the ambipolar field. This work focuses on the non-perturbative impurity injection, which allows us to linearize the equations in terms of the ratio of impurity to background ion density. For future work it would be interesting to vary the injected impurity to background ion density ratio and determine experimentally where the linear approximation breaks down. The full equations for the multispecies diffusion should be considered carefully when modeling transport of impurities in linear devices, tokamaks, and stellerators.

Chapter 6, in part, is currently being prepared for submission for publication of the material. J. J. Gosselin, S. C. Thakur, and G. R. Tynan. The dissertation author was the primary investigator and author of this material.

Table 4 Ion temperatures measured with laser induced fluorescence (LIF). Approximately a 50% increase in temperature is observed over the range of magnetic fields used in these measurements.

Magnetic Field (Gauss)	**Ion Temperature (eV)**
400	0.38 ± 0.02
600	0.41 ± 0.06
800	0.49 ± 0.1
1000	0.50 ± 0.08
1200	0.56 ± 0.07

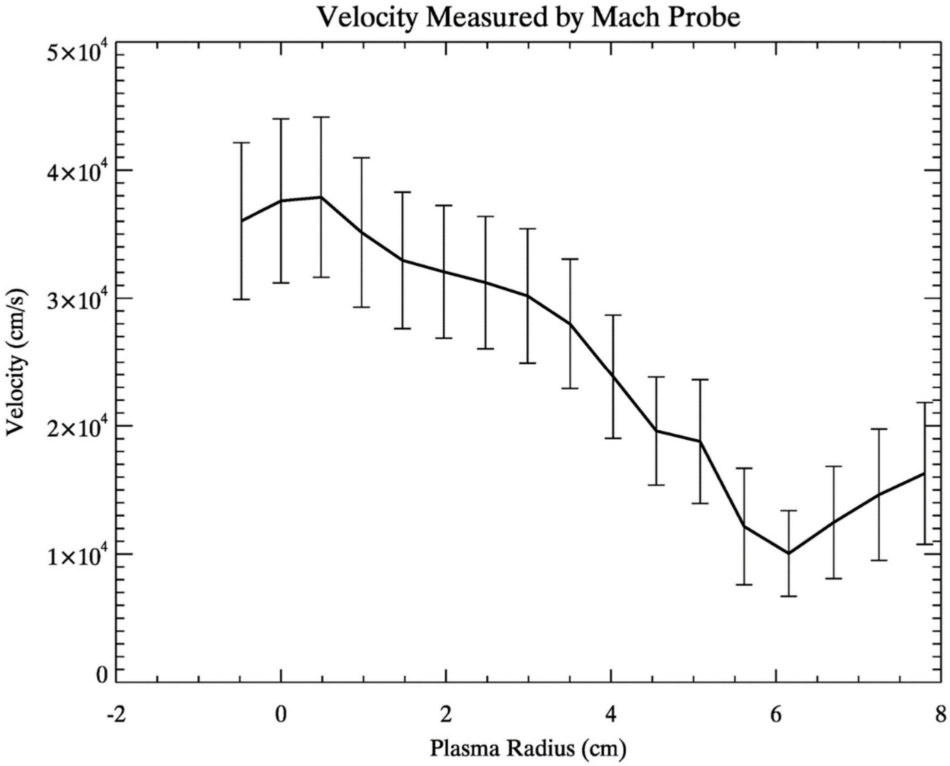

Figure 36 Parallel velocity measured by a Mach probe for the 400 gauss magnetic field. For calculations of the effect of shear the velocity profile is approximated as a quadratic, $V = V_0 (1 - (r/a)^2)$, where $V_0 = 3.6\text{x}10^4$ cm/s and a = 7 cm. Under the plasma conditions at 400 gauss the Mach probe and LIF velocity measurements agree with each other. So, it is assumed that no correction is necessary.

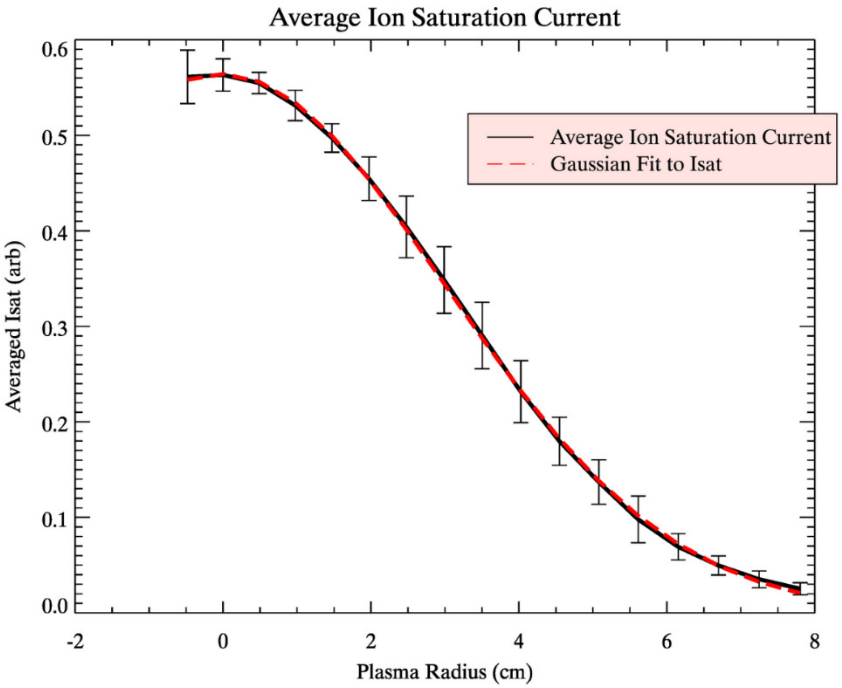

Figure 37 Plot of the ion saturation current in arbitrary units with a Gaussian fit to the profile visible in red. The best fit gives σ = 3 cm.

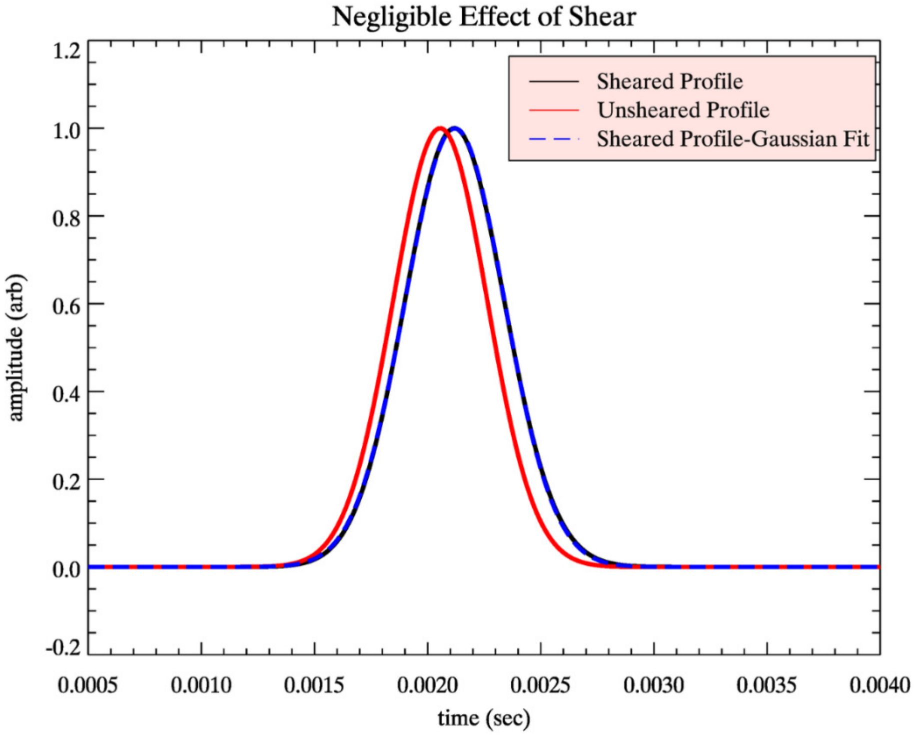

Figure 38 Simulated PMT signal illustrating effect of shear. Diffusion is neglected in the simulation. Shown in black is a sheared impurity emission signal assuming a Gaussian initial condition for the impurity plume. Shown in red is the expected signal for the same plume assuming no shear. In blue is a Gaussian fit to the sheared profile. The shear produces a 3% decrease in plasma velocity, and a 6% increase in the impurity plume width. These changes are considered to be negligible for our experiments.

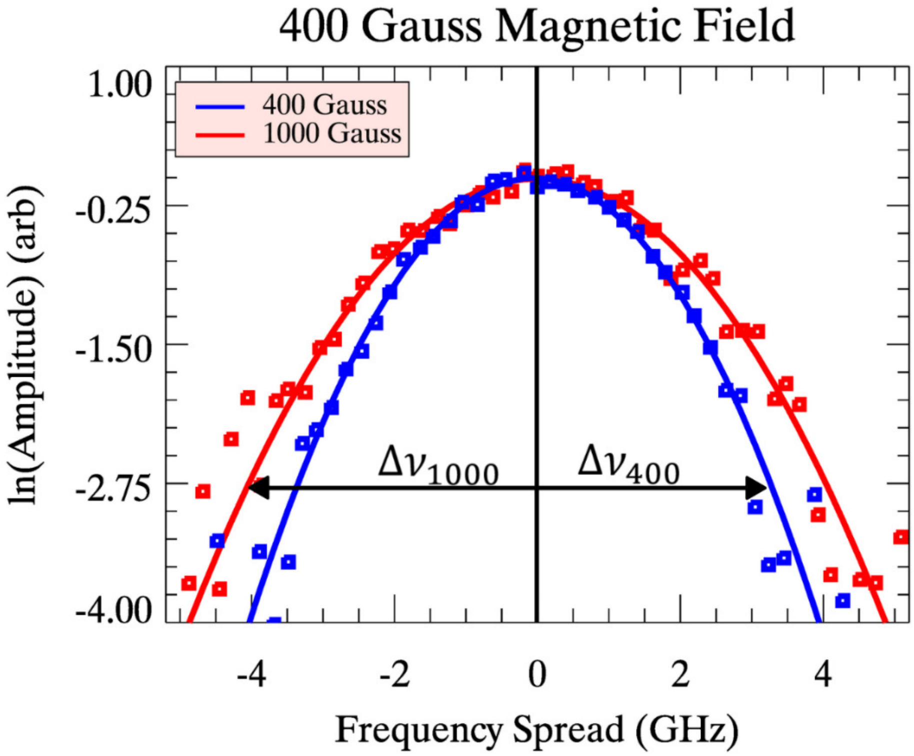

Figure 39 Plot of the LIF signals at 400 and 1000 gauss showing the increasing width of the ion IVDF with increasing temperature.

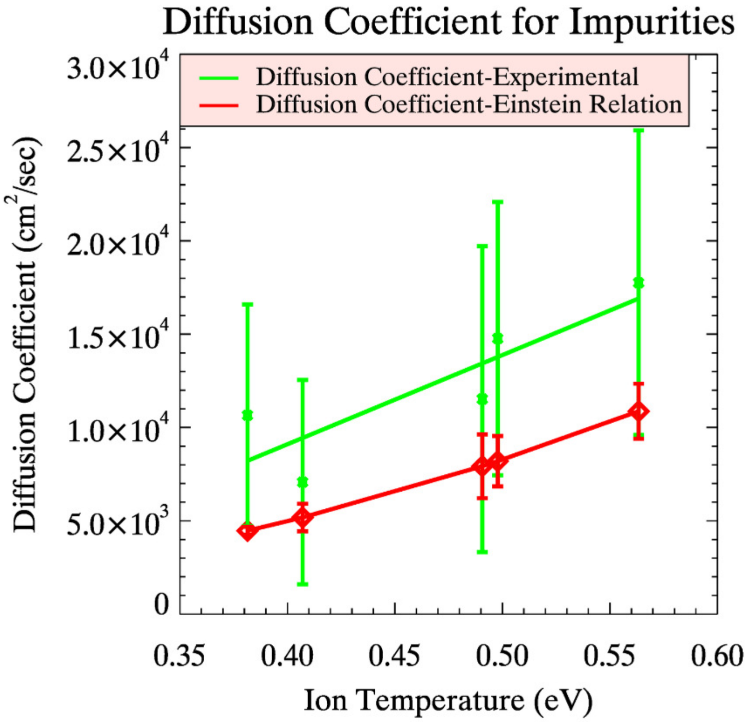

Figure 40 Plot showing the diffusion coefficient as determined by the 1-D advection diffusion modeling. In green is the diffusion coefficient measured assuming the diffusion coefficient is constant along the length of the device. In red is the diffusion coefficient as calculated by the expected bismuth ion temperature. The calculated diffusion coefficient agrees with the measured diffusion coefficient within the error bars. Errors in calculated diffusion coefficient are the result from uncertainty in ion temperature.

Chapter 7: Future Work

The fundamental problem discovered through this thesis work was the systematic error in the Mach probe interpretation. This may be of great importance to the plasma community since these probes are often used to determine the plasma flow velocity[9,46,49,61,70–76]. The theory presented in this thesis is simple, but does a good job of explaining the physical processes behind the discrepancy between the Mach probe interpretation of the velocity and the LIF measured velocity. Future work should focus on testing this model thoroughly and, if necessary, expanding on it by introducing a full 2 or 3 dimensional model.

Fortunately, the parallel LIF experiments described in this thesis provide an excellent fiduciary measurement of the parallel ion velocity. Perhaps the simplest, and easiest to implement, test would be to develop a series of Mach probes of progressively smaller radius in order to test the dependence of the correction term of the probe radius given in equation 27.

$$M_{corr} = \frac{\alpha}{\mathrm{k}\,\sin\alpha}\ln(1 - erf(\sqrt{\frac{a^2 v_d}{4D_\perp L_{ps}}})) \tag{27}$$

One could also build a probe with a progressively decreasing radius such as that presented schematically in Figure 41. By comparing the velocity measured by each set of Mach probe tips to the velocity measured by the LIF system the dependence on the probe radius could easily be determined.

Another test that could be attempted would be to directly measure the wake in the plasma. One could use a sweeping probe to measure the plasma density downstream of an obstruction (such as a large Mach probe). An experiment like this was performed for a connected presheath in the DITE tokamak[58], and the connected presheath was successfully modeled with a diffusive model. When the presheath is unconnected the situation is slightly more complicated; it would be very interesting to see how large of a role parallel diffusion plays, since it is neglected in this study.

It may also be possible to measure the wake by measuring the drop in intensity of ion emission downstream of the probe. If the model for the density drop is correct the light intensity downstream of the probe should be proportional to the plasma density, which is described by:

$$n_d(y,z) = n_0\left(1 - \left(\frac{erf\left((y+a)\sqrt{\frac{v_d}{4D_\perp z}}\right) - erf\left((y-a)\sqrt{\frac{v_d}{4D_\perp z}}\right)}{2}\right)\right) \qquad 28$$

Here, y is the coordinate perpendicular to the magnetic field, and z is the coordinate along the field in slab geometry.

Some preliminary attempts to measure the width of the wake optically were made during this project; however, they were unsuccessful. An image from one of these attempts is shown in Figure 42. While a dark region downstream of the probe shaft can be clearly seen, the region that is visible through the viewport does not extend far enough axially for the shape of the wake to be discernable above the noise level in the image. It may be possible to statistically improve the measurement by taking more images, or it may be necessary to install a larger viewport/use optical techniques to achieve a longer field of view downstream of the probe.

Once a model for the probe wake has been verified, the structure of the probe wake can be used to determine the perpendicular diffusion coefficient. As can be seen from equation 28 the wake structure depends on the ratio of the plasma velocity to the perpendicular diffusion coefficient. By taking multiple measurements with Mach probes with different radii, the plasma velocity can be uniquely determined, and then the structure of the wake should reveal information about the perpendicular diffusion coefficient.

Additionally, the next logical step is to expand the model to be fully two-dimensional. While this model seems to work well, it was developed to explain the discrepancy between the Mach probe and LIF measurements of the plasma velocity under the simplest possible conditions. It is only applied on the axis of the plasma column (r=0). On axis there is no azimuthal velocity to consider. When off axis the probe wake will tilt relative to the magnetic field due to the azimuthal contribution to the velocity, and both perpendicular and parallel diffusion will be important. Developing a full two-dimensional model would be useful for the plasma physics community as a whole.

Finally, with a trust worthy Mach probe these impurity entrainment experiments could be re-attempted. There is some evidence that the plasma flow velocity is proportional to the RF power from the impurity measurements as shown in Figure 43.

It may be possible to use the source RF power as the experimental knob to control the plasma velocity over a limited range. However, it will be necessary to take careful measurements of the electron temperature, there are limits to the amount of power that can be applied through the source, and it may be difficult to determine the ion temperature, which affects the momentum exchange time.

The experiment could be further improved by decreasing the distance between the impurity injection location and the downstream measurement locations. Decreasing the distance will decrease the impurity cloud transit time between the injection location and the downstream measurement locations; this will also result in an increase in the entrainment time/transit time ratio, which will improve the sensitivity of the measurement.

Finally, with the exception of a small amount of work[66,67,77] the topic of multi-species ambipolar diffusion in plasmas remains largely unaddressed. The laser blow off technique could be successfully used to explore this topic further. It would be relatively simple to create thicker coatings or larger spot sizes in order to systematically vary the amount of impurity injected into the plasma. According to the theory laid out by Hill[66], systematically increasing the ratio of impurity density to background plasma density should systematically increase the contribution of the ambipolar enhancement to the diffusion coefficient.

The operation and interpretation of Mach probes has been debated and is known to be different under different plasma parameters[49,78,79]. This project has shown collisions with neutral particles play an important role in the interpretation of Mach probe data. Exploring this model further would be useful for the plasma physics community and would facilitate further studies on parallel impurity transport.

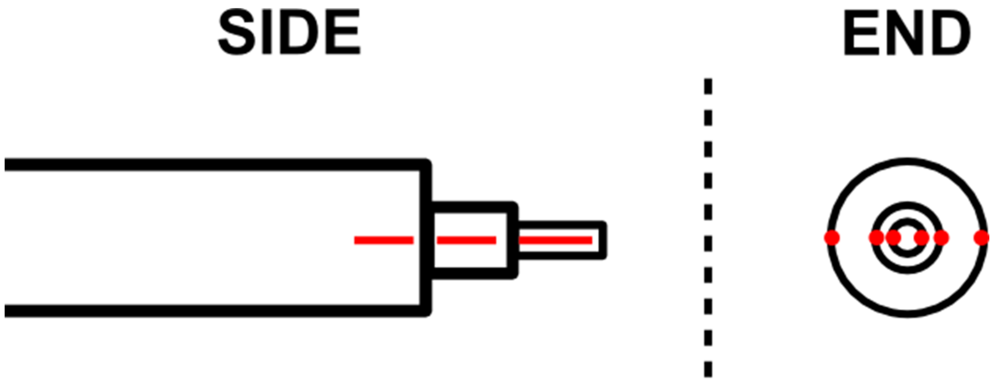

Figure 41 A schematic of a conceptual Mach probe side and end view. The progressively smaller radii should allow for simultaneous measurements of the Mach number with different correction factors. Since the parallel plasma flow velocities in CSDX have been measured accurately with LIF, the dependence of the correction term on the probe radius can be verified.

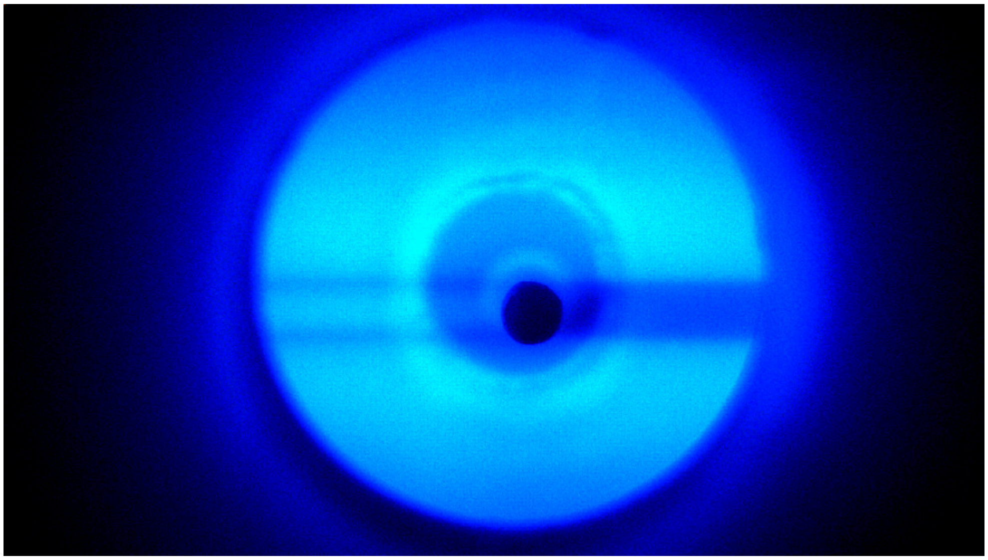

Figure 42 Head on image of the Mach probe fully inserted into the plasma column. Downstream of the probe a region of low light intensity can be seen. This is presumably due to a low density wake from the probe blocking the flowing plasma. Brightness and contrast on the image have been adjusted to emphasize the wake.

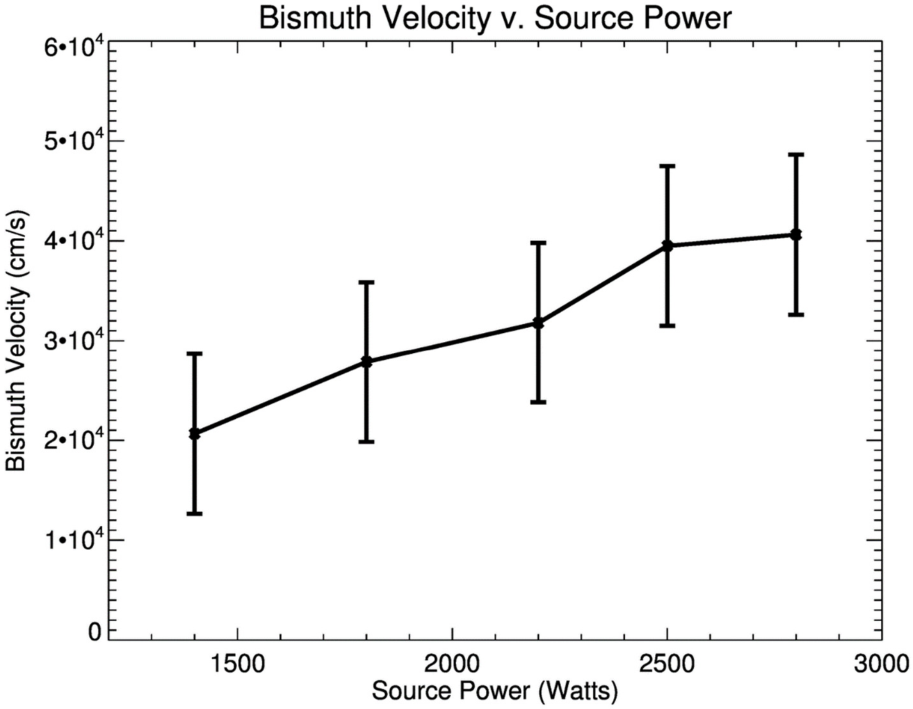

Figure 43 Velocity of the impurity cloud measured as a function of the RF power of the plasma source at 400 gauss. The impurity cloud velocity appears to be linearly proportional to the RF source power over the range of powers used.

Appendix:

There has been some disagreement in the literature as to the location of the Ar-II excitation line with respect to the iodine cell spectrum[80]. In our experiments we find that the unshifted wavelength for the $3d^4F_{7/2}$ to the $4p^4D_{5/2}$ transition agrees well qualitatively with the wavelengths reported in the private communication from Severn reported in Keesee's thesis [80]. Additionally, we have good quantitative agreement with the peak locations reported by Woo[54] for this same Ar-II LIF scheme as shown in Figure 44.

The result in Figure 44 is the I_2 spectrum obtained by of averaging over 350 LIF runs. The iodine spectrum was measured by diverting 8% of the beam intensity with a beam splitter into an iodine cell. The fluorescence from the iodine cell was detected by a photomultiplier tube (PMT). Both iodine cell and PMT were housed in a dark box and the high background (~80% of max signal) is presumed to be scattered laser light. All of the peak measurements agree with those of Woo[54] within one standard deviation with the exception of the smallest, least well-defined peak. The locations of the peaks, labeled 1-4 in Figure 44 were found by fitting a series of Gaussians to each of the 350 iodine spectrum measurements independently. The line positions and uncertainties represent the mean and standard deviations of the fitted parameter for the peak of the Gaussian. Lines 1-4 locations (and uncertainties) are: (1) 668.6174 (± 0.0003) nm, (2) 668.6127 (± 0.0001) nm, (3) 668.6093 (± 0.0003) nm, and (4) 668.6062 (± 0.0005) nm.

This measurement is important because as of the date of publication there are only three comparisons of the Ar-II $3d^4F_{7/2}$ to the $4p^4D_{5/2}$ transition compared to the iodine spectrum (I_2). Woo's counter-propagating laser beam measurements provide an excellent physical measurement of the unshifted line. Based on both the extraordinary number of data points for the iodine spectrum that we collected over our experimental campaign, the qualitative agreement with the report from Severn, and the report from Woo; we can say with a very high level of confidence that we are reporting the correct zero velocity location on the iodine line.

Groups wishing to use LIF for Ar-II velocity measurements can use an iodine cell to verify the wavelength reported by a calibrated wavemeter. The unshifted wavelength of the Ar-II $3d^4F_{7/2}$ to the $4p^4D_{5/2}$ transition is precisely located by the low-frequency "shoulder" of the iodine spectrum, shown as the dotted line in Figure 44. This qualitative feature is visible in the iodine spectrum used by Severn and the fourth figure of Woo's results [54]. Our results represent a quantitative verification of the structure of the iodine spectrum in this wavelength range.

Portions of this appendix have been submitted for publication of the material as it may appear in Physics of Plasmas, 2016, J. J. Gosselin, S. C. Thakur, S. H. Sears, J. S. McKee, E. E. Scime, and G. R. Tynan, American Institute of Physics, 2016. The dissertation author was the primary investigator and author of this paper.

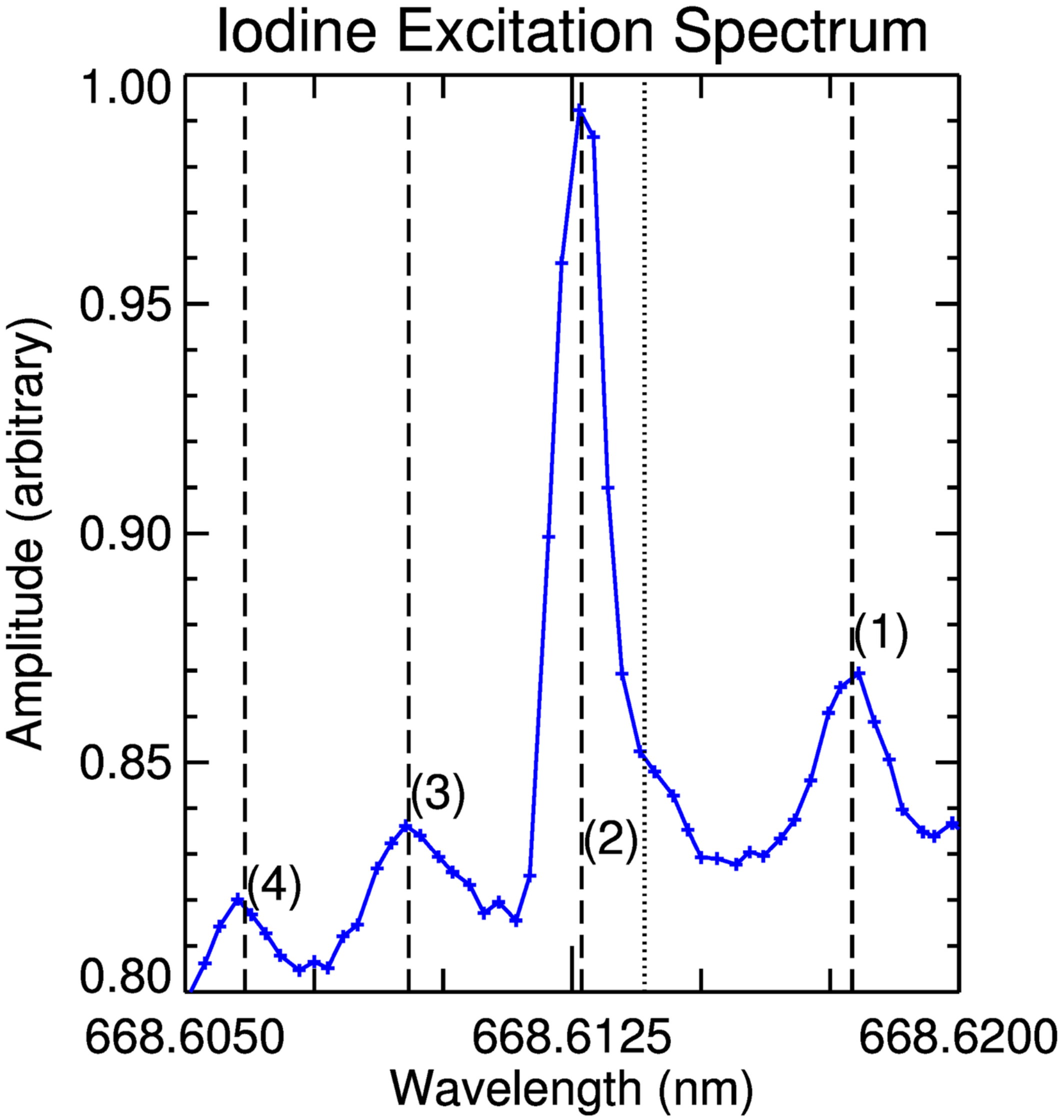

Figure 44 Averaged iodine cell spectrum. Light intensity data is binned and averaged over ~350 individual LIF measurements. Apparent skew represents 5% of absolute intensity. Iodine cell was placed inside a dark box that was not completely light tight. 80% of signal is background; skew represents only 5% of total signal. Labeled peak location was determined by fitting a Gaussian to each run individually; errors represent statistical deviations of peak location. Peaks are: (1) 668.6174 (± 0.0003) nm, (2) 668.6127 (± 0.0001) nm, (3) 668.6093 (± 0.0003) nm, and (4) 668.6062 (± 0.0005) nm. The dotted line represents the unshifted Ar-II $3d^4F_{7/2}$ to the $4p^4D_{5/2}$ transition.

References:

[1] D.R. Lide, 3485 (2005).

[2] C.S. Pitcher and P.C. Stangeby, Plasma Phys. Control. Fusion **39**, 779 (1997).

[3] F.B. Argomedo, E. Witrant, C. Prieur, S. Brémond, R. Nouailletas, and J.-F. Artaud, Nucl. Fusion **53**, 33005 (2013).

[4] V. Philipps, Phys. Scr. **T123**, 24 (2006).

[5] J.P. Coad, P. Andrew, D.E. Hole, S. Lehto, J. Likonen, G.F. Matthews, M. Rubel, and C. Efda-jet, **316**, 419 (2003).

[6] R.A. Pitts, J.P. Coad, D.P. Coster, G. Federici, W. Fundamenski, J. Horacek, K. Krieger, A. Kukushkin, J. Likonen, G.F. Matthews, M. Rubel, J.D. Strachan, and J.-E. Contributors, Plasma Phys. Control. Fusion **47**, B303 (2005).

[7] J. Bohdansky, J. Roth, and H.L. Bay, J. Appl. Phys. **51**, 2861 (1980).

[8] A. Loarte, R. Monk, J. Martin-Solis, D. Campbell, A. Chankin, S. Clement, S. Davies, J. Ehrenberg, S. Erents, H. Guo, P.J. Harbour, L.D. Horton, L.C. Ingesson, H. Jackel, J. Lingertat, C.G. Lowry, C.F. Maggi, G.F. Matthews, K. McCormick, D.. O'Brien, R. Reichle, G. Saibene, R.J. Smith, M.F. Stamp, D. Stork, and G.C. Vlases, Nucl. Fusion **38**, 331 (1998).

[9] G.F. Matthews, Plasma Phys. Control. Fusion **36**, 1595 (1999).

[10] R.A. Pitts, P. Andrew, Y. Andrew, M. Becoulet, I. Coffey, D. Coster, D.C. McDonald, T. Eich, S.K. Erents, M.E. Fenstermacher, W. Fundamenski, G. Haas, A. Hermann, C. Hidalgo, D. Hillis, A. Huber, L.C. Ingesson, S. Jachmich, A. Kallenbach, A. Korotkov, K. Lawson, P. Lomas, T. Loarer, A. Loarte, G.F. Matthews, G. McCracken, A. Meigs, P. Mertens, M. O'Mullane, V. Philipps, G. Porter, A. Pospieszczyk, J. Rapp, D. Reiter, V. Riccardo, G. Saibene, R. Sartori, M.F. Stamp, E. Tsitrone, M. Wischmeier, and J. Gafert, J. Nucl. Mater. **313-316**, 777 (2003).

[11] G.F. Matthews, J. Nucl. Mater. **337-339**, 1 (2005).

[12] J. Roth, J. Nucl. Mater. **266-269**, 51 (1999).

[13] G. Federici, C. Skinner, J. Brooks, J.P. Coad, C. Grisolia, A.A. Haasz, A. Hassanein, V. Phillips, C.S. Pitcher, J. Roth, W.R. Wampler, and D.G. Whyte, Nucl. Fusion **41**, (2001).

[14] S. Yamoto, Y. Homma, K. Hoshino, Y. Sawada, X. Bonnin, D. Coster, R. Schneider, and A. Hatayama, J. Nucl. Mater. **463**, 615 (2015).

[15] D. Naujoks, R. Behrisch, J. Coad, and L. De Kock, Nucl. Fusion **581**, (2002).

[16] T. Parisot, R. Guirlet, C. Bourdelle, X. Garbet, N. Dubuit, F. Imbeaux, and P.R. Thomas, Plasma Phys. Control. Fusion **50**, 055010 (2008).

[17] K. Shimizu, T. Takizuka, and A. Sakasai, J. Nucl. Mater. **241-243**, 167 (1997).

[18] M. Groth, S.L. Allen, J.A. Boedo, N.H. Brooks, J.D. Elder, M.E. Fenstermacher, R.J. Groebner, C.J. Lasnier, a. G. McLean, a. W. Leonard, S. Lisgo, G.D. Porter, M.E. Rensink, T.D. Rognlien, D.L. Rudakov, P.C. Stangeby, W.R. Wampler, J.G. Watkins, W.P. West, and D.G. Whyte, Phys. Plasmas **14**, 056120 (2007).

[19] N. Asakura, J. Nucl. Mater. **363-365**, 41 (2007).

[20] Y. Homma and A. Hatayama, J. Comput. Phys. **231**, 3211 (2012).

[21] J.D. Huba, Plasma Phys. 1 (2011).

[22] P. Wienhold, H.G. Esser, D. Hildebrandt, A. Kirschner, M. Mayer, V. Philipps, and M. Rubel, J. Nucl. Mater. **290–293**, 362 (2001).

[23] J.. Coad, J. Likonen, M. Rubel, E. Vainonen-Ahlgren, D.. Hole, T. Sajavaara, T. Renvall, G.. Matthews, and J.E. Contributors, Nucl. Fusion **46**, 350 (2006).

[24] M. Mayer, V. Rohde, J. Likonen, E. Vainonen-Ahlgren, K. Krieger, X. Gong, and J. Chen, J. Nucl. Mater. **337-339**, 119 (2005).

[25] E. Vainonen-Ahlgren, J. Likonen, T. Renvall, V. Rohde, R. Neu, M. Mayer, R. Pugno, and K. Krieger, J. Nucl. Mater. **337-339**, 55 (2005).

[26] M. Groth, J. a. Boedo, N.H. Brooks, R.C. Isler, a. W. Leonard, G.D. Porter, J.G. Watkins, W.P. West, B.D. Bray, M.E. Fenstermacher, R.J. Groebner, R. a. Moyer, D.L. Rudakov, J.H. Yu, and L. Zeng, Nucl. Fusion **49**, 115002 (2009).

[27] M. Groth, G.D. Porter, J. \A. Boedo, N.H. Brooks, R.C. Isler, W.P. West, B.D. Bray, M.E. Fenstermacher, R.J. Groebner, A.W. Leonard, R.A. Moyer, T.D. Rognlien, J.G. Watkins, and J.H. Yu, J. Nucl. Mater. **390-391**, 343 (2009).

[28] S. Gangadhara and B. LaBombard, Plasma Phys. Control. Fusion **46**, 1617 (2004).

[29] B. LaBombard, J.. Rice, a. . Hubbard, J.. Hughes, M. Greenwald, J. Irby, Y. Lin, B.

Lipschultz, E.. Marmar, C.. Pitcher, N. Smick, S.. Wolfe, S.. Wukitch, and the A. Group, Nucl. Fusion **44**, 1047 (2004).

[30] E.M. Hollmann, K.R. Umstadter, R.P. Doerner, J. Munoz, D. Nishijima, and A.Y. Pigarov, J. Nucl. Mater. **415**, S425 (2011).

[31] N.T. Howard, M. Greenwald, and J.E. Rice, Rev. Sci. Instrum. **82**, 1 (2011).

[32] J.A. Goetz, B. LaBombard, B. Lipschultz, C.S. Pitcher, J.L. Terry, C. Boswell, S. Gangadhara, D. Pappas, J. Weaver, B. Welch, R.L. Boivin, P. Bonoli, C. Fiore, R. Granetz, M. Greenwald, A. Hubbard, I. Hutchinson, J. Irby, E. Marmar, D. Mossessian, M. Porkolab, J. Rice, W.L. Rowan, G. Schilling, J. Snipes, Y. Takase, S. Wolfe, and S. Wukitch, Phys. Plasmas **6**, 1899 (1999).

[33] G.M. McCracken, B. Lipschultz, B. LaBombard, J. a. Goetz, R.S. Granetz, D. Jablonski, S. Lisgo, H. Ohkawa, P.C. Stangeby, and and the A.G.J.L. Terry, Phys. Plasmas **4**, 1681 (1997).

[34] B. Zurro, E. Hollmann, A. Baciero, M.A. Ochando, F. Medina, K.J. McCarthy, E. Blanco, E. de la Cal, D. Carralero, and M.A. Pedrosa, Nucl. Fusion **51**, 063015 (2011).

[35] S. Gangadhara, B. Labombard, and C. MacLatchy, J. Nucl. Mater. **290-293**, 598 (2001).

[36] S. George, A. Kumar, R.K. Singh, and V.P.N. Nampoori, Appl. Phys. Lett. **94**, 2007 (2009).

[37] A. Kumar, H.C. Joshi, V. Prahlad, and R.K. Singh, Phys. Lett. A **374**, 2555 (2010).

[38] R.A. Pitts, S. Carpentier, F. Escourbiac, T. Hirai, V. Komarov, A.S. Kukushkin, S. Lisgo, A. Loarte, M. Merola, R. Mitteau, A.R. Raffray, M. Shimada, and P.C. Stangeby, J. Nucl. Mater. **415**, S957 (2011).

[39] M.A. Lieberman and A.J. Lichtenberg, (1994).

[40] V.A. Abramov, Nucl. Fusion **225**, 225 (1980).

[41] K.-U. Riemann, J. Phys. D. Appl. Phys. **24**, 493 (1991).

[42] N. Hershkowitz, Phys. Plasmas **12**, 1 (2005).

[43] K.U. Riemann, IEEE Trans. Plasma Sci. **23**, 709 (1995).

[44] P. Wienhold, H.G. Esser, D. Hildebrandt, A. Kirschner, M. Mayer, V. Philipps, and

M. Rubel, J. Nucl. Mater. **290–293**, 362 (2001).

[45] S.C. Thakur, C. Brandt, L. Cui, J.J. Gosselin, A.D. Light, and G.R. Tynan, Plasma Sources Sci. Technol. **23**, 044006 (2014).

[46] T. Shikama, S. Kado, A. Okamoto, S. Kajita, and S. Tanaka, Phys. Plasmas **12**, 044504 (2005).

[47] S.C. Thakur, M. Xu, P. Manz, N. Fedorczak, C. Holland, and G.R. Tynan, Phys. Plasmas **20**, (2013).

[48] D.A. D'Ippolito, D.A. Russell, J.R. Myra, S.C. Thakur, G.R. Tynan, and C. Holland, Phys. Plasmas **19**, (2012).

[49] K.-S. Chung, Plasma Sources Sci. Technol. **21**, 063001 (2012).

[50] I. Hutchinson, Plasma Phys. Control. Fusion **1953**, (2002).

[51] L. Patacchini and I.H. Hutchinson, Plasma Phys. Control. Fusion **49**, 1193 (2007).

[52] L. Patacchini and I. Hutchinson, Phys. Rev. E **80**, 036403 (2009).

[53] G.D. Severn, D.A. Edrich, and R. McWilliams, Rev. Sci. Instrum. **69**, 10 (1998).

[54] H. Woo, K. Chung, T. Lho, and R. McWilliams, J. Korean … **48**, 260 (2006).

[55] R.F. Boivin, *WEST VIRGINIA UNIVERSITY PLASMA PHYSICS GROUP INTERNAL REPORT PL-050 Zeeman Splitting for LIF Transitions and De-Convolution Technique to Extract Ion Temperature* (2001).

[56] P. Stangeby, J. Phys. D. Appl. Phys. **1472**, (1987).

[57] C.S. MacLatchy, C. Boucher, D.A. Poirier, and J. Gunn, Rev. Sci. Instrum. **63**, 3923 (1992).

[58] G.F. Matthews, P.C. Stangeby, and P. Sewell, J. Nucl. Mater. (1987).

[59] J. a. Boedo, R. Lehmer, R. a. Moyer, J.G. Watkins, G.D. Porter, T.E. Evans, a. W. Leonard, and M.J. Schaffer, J. Nucl. Mater. **266**, 783 (1999).

[60] K. Chung, J. Korean Phys. Soc. **33**, 54 (1998).

[61] R. a. Pitts, J. Horacek, W. Fundamenski, O.E. Garcia, A.H. Nielsen, M. Wischmeier, V. Naulin, and J. Juul Rasmussen, J. Nucl. Mater. **363-365**, 505 (2007).

[62] L. Oksuz and N. Hershkowitz, Plasma Sources Sci. Technol. **14**, 201 (2005).

[63] M.J. Burin, G.R. Tynan, G.Y. Antar, N.A. Crocker, and C. Holland, Phys. Plasmas **12**, 052320 (2005).

[64] Y.-S. Choi, K.-S. Chung, H.-J. Woo, M.-J. Lee, and T. Lho, J. Phys. D. Appl. Phys. **42**, 225205 (2009).

[65] P.C. Stangeby, J. Nucl. Mater. **415**, S278 (2011).

[66] R.J. Hill, J. Geophys. Res. **83**, (1978).

[67] P.M. Bellan, J. Atmos. Solar-Terrestrial Phys. **73**, 2166 (2011).

[68] J.J. Gosselin, S.C. Thakur, S.H. Sears, J.S. Mckee, E.E. Scime, and G.R. Tynan, Phys. Plasmas (Submitted 2/2016) (2016).

[69] G. Taylor, Proc. R. Soc. A Math. Phys. Eng. Sci. **219**, 186 (1953).

[70] S. Kado, T. Shikama, S. Kajita, T. Oishi, and S. Tanaka, Contrib. to Plasma Phys. **44**, 656 (2004).

[71] S.C. Thakur, D. McCarren, T. Lee, N. Fedorczak, P. Manz, E.E. Scime, G.R. Tynan, M. Xu, and J. Yu, Rev. Sci. Instrum. **83**, 10D708 (2012).

[72] J. a. Boedo, R. Lehmer, R. a. Moyer, J.G. Watkins, G.D. Porter, T.E. Evans, a. W. Leonard, and M.J. Schaffer, J. Nucl. Mater. **266**, 783 (1999).

[73] Y.-S. Choi, H.-J. Woo, K.-S. Chung, M.-J. Lee, D. Zimmerman, and R. McWilliams, Jpn. J. Appl. Phys. **45**, 5945 (2006).

[74] K.-S. Chung and R.D. Bengtson, Phys. Plasmas **4**, 2928 (1997).

[75] T. Shikama, S. Kado, a. Okamoto, and S. Tanaka, Contrib. to Plasma Phys. **46**, 427 (2006).

[76] K. Nagaoka, A. Okamoto, S. Yoshimura, and M.Y. Tanaka, J. Phys. Soc. Japan **70**, 131 (2001).

[77] P. Rosenau and E. Turkel, Phys. Scr. **31**, 207 (2006).

[78] L. Oksuz, M.A. Khedr, and N. Hershkowitz, Phys. Plasmas **8**, 1729 (2001).

[79] I.H. Hutchinson, Phys. Plasmas **9**, 1832 (2002).

[80] A.M. Keesee, Neutral Density Profiles in Argon Helicon Plasmas, 2006.